

University of Calgary

PRISM: University of Calgary's Digital Repository

Graduate Studies

The Vault: Electronic Theses and Dissertations

2020-08

Practical schemes for quantum memories

Moiseev, Evgeny

Moiseev, E. (2020). Practical schemes for quantum memories (Unpublished doctoral thesis).
University of Calgary, Calgary, AB.
<http://hdl.handle.net/1880/112414>
doctoral thesis

University of Calgary graduate students retain copyright ownership and moral rights for their thesis. You may use this material in any way that is permitted by the Copyright Act or through licensing that has been assigned to the document. For uses that are not allowable under copyright legislation or licensing, you are required to seek permission.

Downloaded from PRISM: <https://prism.ucalgary.ca>

UNIVERSITY OF CALGARY

Practical schemes for quantum memories

by

Evgeny Moiseev

A THESIS

SUBMITTED TO THE FACULTY OF GRADUATE STUDIES
IN PARTIAL FULFILLMENT OF THE REQUIREMENTS FOR THE
DEGREE OF DOCTOR OF PHILOSOPHY

GRADUATE PROGRAM IN PHYSICS AND ASTRONOMY

CALGARY, ALBERTA

AUGUST, 2020

© Evgeny Moiseev 2020

Abstract

This dissertation is devoted to the development of quantum memories for light. Quantum memory is an important part of future long-distance quantum fiber networks and quantum processing. Quantum memory is required to be efficient, multimode, noise free, scalable, and should be able to provide long storage times for practical applications in quantum communications and beyond. Here I concentrate on solving particular problems of different quantum protocols and find ways for extending the performance of memories and adding new capabilities.

I theoretically show that an array of whispering-gallery resonators is capable of being an efficient and noise-free optical memory with an adjustable storage time. The potential for on-chip realization at room temperature makes the scheme attractive for easy implementation.

The effect of Raman scattering in echo memory was evaluated experimentally and theoretically. The noise performance of gradient echo memory in Λ configuration proves, that the developed theory is in a good agreement with an experiment.

I proposed a mechanism for extending the bandwidth of impedance-matched memories via a white-light cavity effect. The introduced additional dispersion compensates a bandwidth decrease induced by the cavity and hence increases the spectral zone of impedance matching. Theoretically the scheme allows to increase the bandwidth of high efficient storage ($> 90\%$) several times without adding extra noise.

Finally, I have proposed an architecture of quantum random-access memory for time-bin photons. The architecture consists from a memory unit and a strongly coupled three-level atom. Both of them are placed in their own cavities, which are coupled to each other. The protocol allows to achieve quantum addressing of quantum information stored in the memory with only a single control unit. This is useful for numerous tasks in quantum machine learning.

Preface

In this preface I discuss the role I played in each of the chapter through out the thesis. Specifically, I briefly describe each chapter, my collaborators and my and their contribution to these chapters.

In the first chapter, I present a historic overview of the prior methods and techniques used for implementation of optical quantum memories. I identified the relevant literature and wrote the chapter by myself. I received feedback from B.C. Sanders and A. Tashchilina.

In the second chapter, I present relevant prior theory for describing optical quantum memories, which is used for subsequent analysis in the next chapters. I wrote the chapter on my own with feedback from B.C. Sanders.

In the third chapter, I present a scheme for an on-chip optical quantum memory based on an array of whispering gallery mode resonators. The concept of Chapter 3 was proposed by S.A. Moiseev with the novelties being that resonators have a chirped frequencies and are coupled to a common waveguide. I derived and wrote the mathematical expressions for modeling the proposed concept, and I solved the mathematical expressions analytically for optical quantum memory operation. I developed optimization methods to determine control parameters for the highest storage efficiency. I discussed with S.A. Moiseev the analogous resonator-based optical quantum memory, and together we compared the result with the state of art. As a result, I produced Figures 3.2–3.4, Tables 3.1–3.2 and corresponding captions, while S.A. Moiseev created Figure 3.1 and its caption. The chapter is largely taken from the article I wrote with S.A. Moiseev. Specifically, in that article I wrote sections

about the proposed scheme, comparison with other protocols and possible experimental implementation. S.A. Moiseev wrote the introduction and the conclusion.

In Chapter 4, I present a proposal for extending the bandwidth of impedance-matched quantum memory. The concept for Chapter 4 was proposed by S.A. Moiseev with novelty being use of compensating dispersion for extending the bandwidth. I developed the proposal into a full scheme, derived and wrote the mathematical expressions for describing cavity-enhanced Raman storage on a three-level atomic medium accompanied by the Raman gain medium. Together with A. Tashchilina we determined optimal parameters for cavity, storage and dispersion compensating media for desired optical quantum memory bandwidth extension while minimizing noise. Specifically, A. Tashchilina created Figure 4.3 and Table 4.1, while I created all the rest of figures and tables. I critically assessed feasibility for experimental proposal and have wrote an initial draft of the paper. I discussed the result with B.C. Sanders, he improved the writing especially by highlighting the central idea of the initial draft. None of the content of Chapter 4 is yet in the submitted manuscript, furthermore I wrote the corresponding chapter myself.

In Chapter 5, I present my study of noise in gradient echo memory, which was proposed by A.I Lvovsky. C. Kupchak, who was undertaking his PhD under supervision of A. I. Lvovsky, experimentally observed previously unreported noise in the retrieved optical field from the gradient echo memory. I built a mathematical model for the description of noise generation due to Raman scattering of the residual population in atomic vapor memory, and I successfully fitted the C. Kupchak's experimental data within my model. Then I developed a strategy for how to suppress the noise. I wrote Chapter 5 entirely by myself. None of the content of Chapter 5 is yet in the submitted manuscript.

In Chapter 6, I present my original idea for a quantum random access memory protocol. I developed a mathematical description for my idea, and constructed all Figures 6.1–6.5 and corresponding captions. I have discussed my concept with S.A. Moiseev and A.I. Lvovsky. The Chapter 6 reproduces the paper I coauthored together with S.A. Moiseev. In this paper

I wrote section about the description of the scheme, quantum addressing and experimental issues, which correspond to sections 6.2–6.4 of Chapter 6, respectively. In turn, S.A. Moiseev wrote the introduction and the conclusion.

In the last chapter, I conclude the results of the conducted research and discuss possible future studies. I wrote the chapter on my own with feedback from B.C. Sanders.

At the end of the dissertation, I present the bibliography and Appendices A and B for Chapters 5 and 6, respectively. The bibliography and Appendix A are written by myself with feedback from B.C. Sanders. Appendix B is based on the jointly written paper and is written on my own.

Acknowledgements

I would like to express my sincere gratitude to Professor Barry Sanders for all his support and advice during my studies. It was both an honor and a privilege to work with him.

My great appreciation goes to Arina Tashchilina, who is always a most reliable person and a great support in all the struggles and frustrations I faced. I give my special feeling of gratitude to my family members, Valery, Sergey and Olga, whose advice and words of encouragement kept my morale high. I owe a great deal of thanks to Patrick J. Irwin for always willing to discuss physics and for sharing kindness.

I would like to thank all wonderful people with whom I had an opportunity to collaborate with: Prof. Alexander Lvovsky, Dr. Connor Kupchak, Paul Anderson, Di Chang, Prof. Christoph Simon, Prof. Paul Barclay, Fang Yang, Shreyas Jalnapurkar and Prof. Arthur Lezamo.

Publication list

1. F. Yang, A. Tashchilina, E. S. Moiseev, C. Simon, A. I. Lvovsky. Far-field linear optical superresolution via heterodyne detection in a higher-order local oscillator mode. *Optica*, 3(10):1148-52, 2016.
2. E. S. Moiseev, S. A. Moiseev. Time-bin quantum RAM. *Journal of Modern Optics*, 63(20):2081-92, 2016. The material of the publication is presented in Chapter 6.
3. E. S. Moiseev and S. A. Moiseev. All-optical photon echo on a chip. *Laser Physics Letters*, 14(1):015202, 2016. The material of the publication is presented in Chapter 3.
4. P. Anderson, S. Jalnapurkar, E. S. Moiseev, D. Chang, P.E. Barclay, A. Lezama, A. I. Lvovsky. Optical nanofiber temperature monitoring via double heterodyne detection. *AIP Advances*, 8(5):055005, 2018.
5. S. Jalnapurkar , P. Anderson, E. S. Moiseev, P. Palittapongarnpim, A. Narayanan, P. E. Barclay, A. I. Lvovsky. Measuring fluorescence into a nanofiber by observing field quadrature noise. *Optics letters*, 44(7):1678-81, 2019.
6. E. S. Moiseev, A. Tashchilina , S. A. Moiseev , A. I. Lvovsky. Darkness of two-mode squeezed light in Λ -type atomic system. *New Journal of Physics*. 22(1):013014, 2020.
7. E. S. Moiseev, A. Tashchilina , S. A. Moiseev and B. C. Sanders. Broadband quantum memory in cavity with zero spectral dispersion (in preparation). The material of the manuscript is presented in Chapter 4.

8. E. S. Moiseev, C. Kupchak, A. Tashchilina and A. I. Lvovsky. Raman noise in gradient echo memory (in preparation). The material of the manuscript is presented in Chapter

5

Table of Contents

Abstract	ii
Preface	iii
Acknowledgements	vi
Publication list	vii
Table of Contents	ix
List of Figures and Illustrations	xii
List of Tables	xiii
List of Symbols, Abbreviations and Nomenclature	xiv
1 Introduction	1
1.1 Quantum memories	1
1.1.1 Duan-Lukin-Cirac-Zoller protocol	1
1.1.2 Electromagnetically induced transparency	3
1.1.3 Raman memory	4
1.1.4 Photon echo	5
1.1.5 Controlled reversal of inhomogeneous broadening	6
1.1.6 Atomic frequency comb	7
1.1.7 Revival of silenced echo	8
1.1.8 Cavity enhancement	9
1.2 Memory performance benchmarks	10
1.2.1 Efficiency	10
1.2.2 Fidelity	10
1.2.3 Lifetime	11
1.2.4 Multimodeness	12
1.2.5 Bandwidth	12
1.3 Benchmark records	12
1.3.1 High efficiencies	13
1.3.2 Fidelity	14
1.3.3 Lifetime	15

1.3.4	Multimodeness	16
1.3.5	Bandwidth	16
1.3.6	Current performance and perspective goal	17
1.4	Conclusion and research impact	17
2	Light-matter interaction	19
2.1	Ensemble of two-level atoms	19
2.1.1	Electric-dipole interaction	19
2.1.2	Rotating reference frame	22
2.1.3	Uniformity of an ensemble and inhomogeneous broadening	23
2.1.4	Heisenberg equations of motion	24
2.2	Λ system-based	25
2.2.1	Heisenberg equations of motion	25
2.2.2	Cavity enhancement	27
2.3	Conclusion	28
3	All-optical photon echo and memory on a chip	29
3.1	Introduction	29
3.2	Proposed scheme	30
3.3	Comparison with other protocols	35
3.4	Possible experimental implementations	38
3.5	Conclusion and discussion	40
4	White cavity	42
4.1	Introduction	42
4.2	Classical approach	44
4.3	Quantum mechanical approach: Model	48
4.4	Controlling the field storage by one and two additional off-resonant laser fields	51
4.5	Noises in the scheme	54
4.6	Experimental feasibility	56
4.7	Conclusion	59
5	Raman noises in gradient echo memory	61
5.1	Introduction	61
5.2	Experiment	62
5.3	Theoretical model	64
5.4	Noise analysis	69
5.4.1	Dominating noise mechanism	69
5.4.2	Raman noise analysis	70
5.5	Conclusion	74
6	Time-bin quantum random access memory	76
6.1	Introduction	76
6.2	Scheme	80
6.2.1	Single photon storage	80

6.2.2	Impedance matching conditions	84
6.2.3	Photonic transfer blockade	85
6.2.4	Echo photon retrieval	87
6.3	Quantum addressing	88
6.4	Possible experimental implementations	93
6.5	Conclusion	94
7	Conclusion and discussion	96
	Bibliography	99
A	Raman noises	129
A.1	Spontaneous Emission	129
A.1.1	The Wigner-Eckart theorem	133
A.2	Effect of spatial modulation	133
A.3	Simulation parameters	135
B	Time-bin quantum random access memory	136
B.1	Hamiltonian and equations of motions	136
B.2	Readout stage	139
B.3	Blockade and wave function of the QM atomic system	140

List of Figures and Illustrations

1.1	Various quantum memory protocols	3
1.2	The Hahn spin-echo.	5
1.3	Quantum regime of echo memory.	6
2.1	Three level diagram	25
3.1	The schematic of the proposed memory and delay line	31
3.2	The time domain recall of three pulses input and efficiency of the scheme as a function of the comb finesse	33
3.3	Effect of the coupling constant on the retrieval times of the scheme	34
3.4	Normalized intensities of the input and output light pulses for different coupling constants	35
3.5	The principle schemes of SCISSOR and CROW.	36
4.1	Classical model	47
4.2	Atomic level system	49
4.3	Numerical simulation of the storage bandwidth	52
4.4	Noise spectrum	55
5.1	Schematic of the experiment	62
5.2	Level diagram of the atomic transition	64
5.3	Level populations and absorption line	68
5.4	Noise dependence on control parameters	70
5.5	Noises detected in the experiment with theoretical fits	71
5.6	Noise dependencies on experimental parameters: detuning, power, and angle	73
5.7	Possible Λ schemes for better noise suppression	74
6.1	Bucket-brigade scheme	77
6.2	Quantum RAM scheme	80
6.3	Spectral transfer funciton	82
6.4	Efficiency of the echo revival	88
6.5	Temporal quantum addressing	89

List of Tables

3.1	Comparison of delay times for SCISSOR- and CRC schemes	39
3.2	Time delays for different possible experimental implementations.	40
4.2	Parameters used to find the noise spectrum	56
4.3	Potential candidates for implementation of the off-resonant Raman QM . . .	56
4.4	Recent telecom quantum memory realizations	59
5.1	Parameters used in calculations.	73
A.1	Parameters used to fit an experimental data	135

List of Symbols, Abbreviations and Nomenclature

AFC	atomic frequency comb
ATS	Autler-Townes splitting
CRC	chirped ring-cavity
CRIB	controlled reversal of inhomogeneous broadening
CROW	coupled resonator optical waveguide
DLCZ	Duan-Lukin-Cirac-Zoller
EIT	electromagnetically induced transparency
FSR	free spectral range
FWM	four-wave mixing
GEM	gradient echo memory
IM	impedance matching
QM	quantum memory
ROSE	revival of silenced echo
SCISSOR	side coupled integrated spaced sequence of resonators
WGM	whispering gallery mode
qRAM	quantum random access memory

Chapter 1

Introduction

1.1 Quantum memories

Quantum memory (QM) [1] is a device that is capable of writing in and reading out a qubit, an elementary bit of quantum information [2]. Following this definition, we can say that any qubit is a quantum memory. To distinguish a QM from a qubit, we assume that a useful quantum memory is capable of storing quantum information, in other words keeping the original quantum state for a long time and converting state into a qubit. In summary, a QM should not be capable of performing one- or two-qubits gates, but must be capable of storing and transferring a quantum information between itself and some given type of qubits.

1.1.1 Duan-Lukin-Cirac-Zoller protocol

The concept of QM is of special value for a quantum repeater in the context of long-distance quantum communication [1]. The quantum repeater was proposed as a tool to mitigate the limitation of the direct transmission of photonic qubits between two parties at long distances. The distance of direct quantum communication via a fiber-link is roughly limited to a few hundreds of kilometers due to absorption and the Rayleigh scattering of

photons in silica. The proposed way to handle this problem is to create an entanglement between QMs located at reasonably close distances by transmitting photons. The sequential swap of the entanglement between the neighbouring QMs transfers the entanglement to a distance twice the photons have traveled. The swapping can be done using a Bell-basis measurement device [3]. For ideal quantum repeaters the cost of communication becomes polynomial with distance in contrast to exponential for direct transmission [4]. However in practice the use of repeaters with non-ideal components can only reduce the exponential factor in comparison with direct transmission [4, 5].

The first practical proposal for a quantum repeater exploited homogeneous atomic ensembles serving as a source of entanglement between photons and a long-lived collective atomic excitation [6]. The protocol was called after the authors: Duan-Lukin-Cirac-Zoller (DLCZ). The atomic ensemble has a Λ transition with all atoms populating one level. An interrogation of the atomic ensemble with a detuned laser field induces Raman scattering of the laser photons and creates an atomic excitation (see Fig. 1.1 (a)). If a pair of such ensembles is used, the scattered photons can be sent to the ports of a 50/50 beam splitter at the output of which single-photon counting modules are installed. Due to indistinguishability of the photons a click of any of the single-photon counting modules would produce a delocalized excitation between two atomic ensembles, which itself is an entangled state. The collective nature of excitation and the corresponding coherence provides deterministically high probability of atomic excitation conversion into the photonic one by applying a laser on the proper transition. Thus the delocalized entanglement can be converted into the photonic and exploited by quantum optical techniques. The more elaborated schemes of the DLCZ protocol use additional polarization [7], temporal [8], and spatial multimodeness [9] in order to increase the rate and robustness of the entanglement creation.

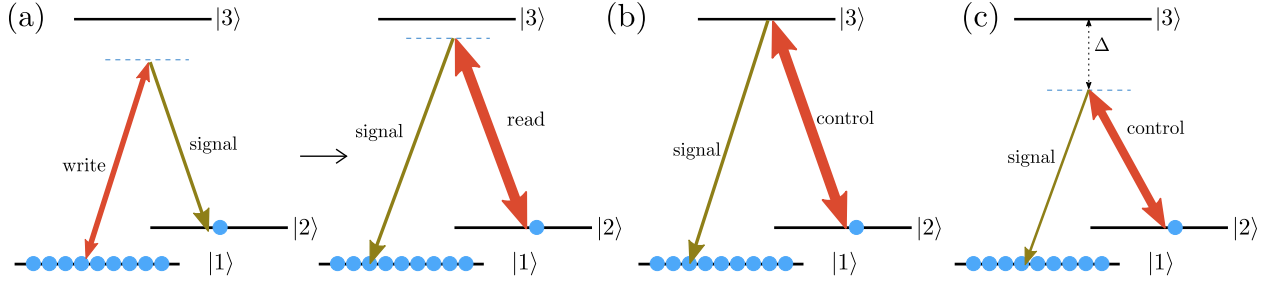


Figure (1.1) Different quantum memory protocols. (a) DLCZ protocol comprises of two steps: write-in and read out. During the first step a single atom is transferred from $|1\rangle$ to level $|2\rangle$. Simultaneously with that a signal photon is emitted and detected. The spin coherence between two lowest levels makes the read-out of the single excitation coherently enhanced. (b) In EIT scheme resonant control field creates a transparent window, while signal field is converted into a spin wave. (c) In Raman protocol signal and control fields are far detuned from the upper level, although are in a two-photon resonance. The three level system is mapped onto a two-level system.

1.1.2 Electromagnetically induced transparency

At the same time other protocols for quantum memory have been proposed. In contrast to DLCZ, where the system works as a memory and a generator of the quantum states, the so-called absorptive memories are designed for converting flying optical qubits into long-lived matter excitations, storing them, and deterministically reemitting them.

The memory protocol based on the electromagnetically induced transparency (EIT) exploits the resonant transparency window [10]. This window is induced by a strong control field acting resonantly on one transition of a Λ scheme (see Fig. 1.1 (b)). At the same time, the signal field is resonant with another transition, where most of the atomic population is located. Fundamentally, the transparency is based on an adiabatic conversion of the propagating signal field into an atomic spin wave in the limit of a long signal pulse. This spin wave is conserved during propagation, since atoms transit into an eigenstate of the interaction Hamiltonian with a zero eigenvalue. The match between the signal waveform and the bandwidth of the transparency window is necessary to ensure a full conversion of the signal field onto an atomic coherence. If the control field is adiabatically switched off [11, 12] while the signal field is within the atomic medium, the quantum statistical information of the field will stay within the medium encoded as an atomic coherence of the corresponding state.

Switching the control field back on converts the coherence back into an optical excitation and allows the signal to escape the medium.

1.1.3 Raman memory

Another type of memory, the Raman memory, also uses a Λ atomic scheme except with a large single photon detuning (see Fig. 1.1 (c)) [13, 14]. For large detunings between an atomic system resonance and a signal field, the upper level could be adiabatically eliminated [15]. Thus, the system is reduced to an effective two-level system composed of two ground levels. As in the EIT protocol, switching off the control field maps the quantum state onto the coherence between two ground levels. In contrast to the EIT protocol, where the control field creates the transparency window for signal field, in Raman memories a far-detuned control field permits an effective interaction for the signal field, which otherwise would pass the atomic medium without absorption. Properly shaped pulse of the control field permits an effective transfer without reemission and an effective read-out without reabsorption [12, 13]. The recall from the memory can be mathematically expressed as an integral convolution between the kernel of the process and an input field amplitude. In turn, the kernel can be decomposed into a normalized set of orthogonal eigenfunctions [16]. These eigenfunctions form a basis of possible orthogonal spin waves available for storage, while the corresponding eigenvalues represent the total efficiency of the memory. This means that using different control field waveforms allows the storage of multiple fields independently in the same media. Eventually, it provides the multimode capabilities to the Raman memory in contrast to the single-mode EIT protocol [16, 17].

A protocol combining the resonant interaction as in EIT with a fast operational speed as in Raman memory was also proposed [18, 19]. The use of resonant interaction reduces the need of a powerful control field, as required for EIT, while providing faster operation with similar multimodeness, as in Raman memory. The effect of dynamical Autler-Townes splitting was used to name the protocol as “ATS memory”. A demonstration of the memory

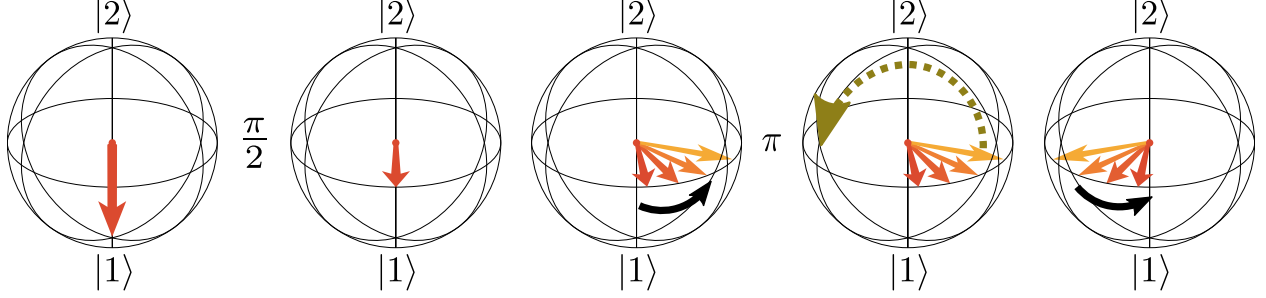


Figure (1.2) The Hahn spin-echo. a) The application of $\pi/2$ pulse creates coherent superposition between two levels: $\frac{|1\rangle+|2\rangle}{\sqrt{2}}$. b) The dephasing of different atoms destroys the collective coherence. c) The application of a π pulse reverts the phase accumulation and makes atoms to evolve towards the state with macroscopic coherence.

showed a potential for a large delay-bandwidth product [20, 21], which means that the short pulses could be stored effectively.

1.1.4 Photon echo

In all protocols of the above, homogeneous media are used for storage. This limits available types of media for storage. Therewith, the inhomogeneous spectral broadening allows the storage of multiple modes for a given optical depth [16, 22]. The memory protocols available for inhomogeneously broadened media are based on the idea of a photon echo that in turn was inspired by the Hahn spin echo [23, 24]. An initially polarized ensemble of atoms is transferred into a superposition of two levels by a $\pi/2$ pulse, as shown in Figure 1.2. The created collective dipole moment experiences decay due to the presence of an inhomogeneous frequency broadening, meaning that with time, atoms with different frequencies accumulate different phases and destructively interfere. The application of a π pulse at time τ after the $\pi/2$ pulse reverses the evolution, making ‘slower’ atoms ahead of the atoms with no broadening and the ‘fast’ ones trail behind. Eventually, the ‘fast’ atoms catch up with the unbroadened atoms and the ‘slow’ ones drift back toward them. The complete refocusing happens at time 2τ and produces a collective dipole that irradiates the echo in the direction defined by a phase matching. This technique is widely used in magnetic resonance and optics as a tool for studying the spectroscopic parameters of different materials [25, 26, 27]. As

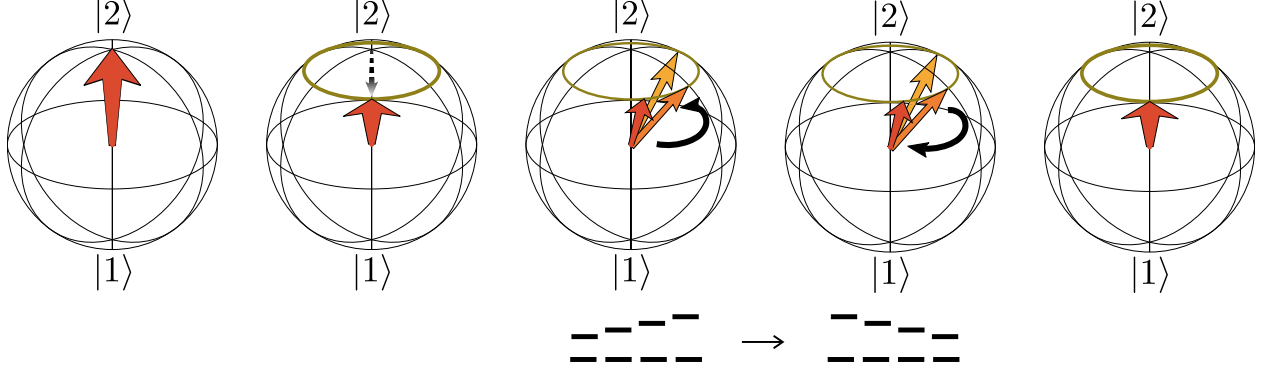


Figure (1.3) Quantum regime of echo memory. The applied weak light rotates the atomic Bloch vector towards the equator by the angle corresponding to pulse area of the stored light. The frequency gradient destroys the induced coherence. The reverse of the gradient performs a time reversal operation, which leads to subsequent echo irradiation.

well it was known for the operation as a classical optical memory with processing abilities [22, 28, 29, 30].

The described echo protocol is not suitable for operating in a quantum regime [31, 32], in which the dipole moment is created by an arbitrarily weak field instead of a $\pi/2$ pulse. The application of the refocusing π pulse completely inverts the population and provides a huge amplification to an echo induced by the initial signal. The amplification noise completely buries the quantum statistics of the stored field [33]. Several ways were proposed to mitigate this issue and we discuss them below.

1.1.5 Controlled reversal of inhomogeneous broadening

The first proposal exploited a different mechanism of refocusing [31, 34]. Instead of a π pulse, refocusing was induced by changing the sign of the inhomogeneous broadening at time τ . Because of that the phase is restoring to the initial value, which is the same for all atoms in the ensemble. After 2τ the phase returns to its initial value upon excitation and atoms coherently emit light. Since the essential part of this protocol is the manipulation of an inhomogeneous broadening, the protocol was later called controlled reversal of inhomogeneous broadening (CRIB). If the protocol is employed in a Λ system, where all atoms are

prepared in the ground state $|1\rangle$, an additional π pulse may be used on transition $|2\rangle \rightarrow |3\rangle$ to transfer the excitation into a long-lived level $|3\rangle$. In addition, this π pulse would allow a reemission of the signal in the backwards direction, eliminating a reabsorption of the emitted signal on transition $|1\rangle \rightarrow |2\rangle$.

For the best performance of the CRIB protocol, it is desirable to use a homogeneous broadened atomic system and induce an externally controlled broadening by magnetic or electric field gradients. It is worth noting that the CRIB protocol provides a perfect time reversibility that results in the reversed temporal shape of the echo signal with respect to the input signal pulse. A modified version of the CRIB is a so-called gradient echo memory (GEM) [35, 36] that uses a magnetic or electric gradient along the propagation of the signal field. The GEM, with a backward echo emission, coincides with CRIB. A spatially dependent atomic frequency shift allows the recall of the light into the forward direction without reabsorption. This is possible since the reemitted spectral components of echo are not in resonance with atoms. However, the forward GEM scheme loses its perfect time reversibility, which could lead to phase distortions [36].

The Λ -GEM [37, 38, 39] exploits the Raman transition induced by a control field acting on the $|2\rangle \rightarrow |3\rangle$ transition with broadening applied to the ground levels in a Λ scheme. The Λ -GEM allows storage of the light on the long-lived spin coherence without application of π pulses (as in CRIB), and without specially shaped control field (as in Raman memory). As in the usual GEM, the reversal of the applied gradient together with an application of the control field produces an echo in a forward direction.

1.1.6 Atomic frequency comb

One more approach of rephasing was proposed for inhomogeneously broadened atoms and is called the atomic frequency comb protocol (AFC) [40]. This protocol exploits simultaneously a large inhomogeneous linewidth of the rare-earth ions and relatively long coherence times of an individual ion. It is beneficial to have large ratio between inhomogeneous and

homogeneous linewidths. The idea is to isolate N absorbing homogeneously-broadened two-level atoms—equidistantly separated by Δ and spanned over bandwidth $N\Delta$. Isolating these two-level atoms can be done with the spectral hole-burning technique [41] in the way that ions with the frequency in between the absorbing peaks are pumped into metastable levels, which are not coupled by the fields. The incoming signal, having a waveform spanned over the frequency comb, gets converted into the superposition of excitations distributed along the peaks. The induced dipole dephases since each peak has a different frequency. Due to evolution at time $\tau = 2\pi/\Delta$ after the absorption, the atoms again become in phase and reemit the light. Thus, the AFC works as a delay line with a predefined storage time and with no on demand recall. In turn, the on demand recall can be realized similarly to the CRIB protocol with the help of an empty auxiliary level in a Λ configuration. The application of a π pulse may transfer the excitation into this auxiliary level, from where it can be returned back at an arbitrary time and re-emitted from the atomic comb. As well, storage on an auxiliary level enables recall in a backward direction that would mitigate the reabsorption in forward configuration as in CRIB.

While the AFC protocol was designed for a broadband operation, the creation of an efficient and broad spectral structure was limited by a hyperfine splitting. The optical hole burning moves the atoms into an auxiliary level, which is usually the other hyperfine sublevel of the ground state. Thus, the effective comb bandwidth could not exceed the splitting between these levels without degrading the comb properties [42]. In some materials an absorption profile could be shaped by pumping atoms to distant shelving states, located outside of the absorption bandwidth [43], extending the bandwidth to gigahertz.

1.1.7 Revival of silenced echo

Few protocols were proposed for exploiting the whole natural inhomogeneous broadening for storing short pulses [44, 45, 46]. The main idea behind the protocols is the use of two π pulses similarly to the traditional photon echo. After application of the first π pulse the

dipole induced by the signal pulse starts to rephase. In order to avoid the irradiation of the echo into the amplifying media, the echo is suppressed by the application of an external gradient during the rephasing [46], or by the phase-mismatching between the signal and π pulses [44, 45]. The second π pulse returns the population back to the initial state and the irradiated echo reproduces initial signal without amplification noise. From now on, this family of protocols will be called ‘ROSE-based’ after the basic principle of revival of silenced echo (ROSE). While this protocol demonstrates a high efficiency [47], the non-idealities of the π pulses produce significant noise.

1.1.8 Cavity enhancement

All of the mentioned protocols are based on the mapping of the photonic excitations onto the atomic ones. The ideal mapping is achieved only asymptotically for large optical depth, or for high number of interacting atoms [11]. Unfortunately, the straightforward increase of the atom number is usually accompanied by negative effects, such as an increase of decoherence. As in cavity quantum electrodynamics [48] the use of an optical resonator provides an enhancement of the light-atom interaction. All of the mentioned protocols can be used in the cavity configuration. However, in the EIT and Raman schemes a use of a cavity to increase an effective optical depth keeps the asymptotic scaling of the efficiency [49]. In turn, for the echo memory, the impedance matching guarantees ideal mapping for a finite optical depth [50, 51]. It becomes possible since the mapping between the light and atom occurs via the decay of the induced collective dipole moment, while for the EIT and the Raman the collective dipole moment does not experience degradation.

In the next section, we list main criteria used to assess performance of the memory. In the view of these criteria, in section 1.3, we discuss the advantages of every type of the memory and conclude whether these protocols are applicable for quantum communications.

1.2 Memory performance benchmarks

Nowadays there are several figures of merits of a quantum memory performance. Below we list these criteria and the best known experimental realizations. Moreover, we highlight how these requirements limit the amount of suitable physical systems.

1.2.1 Efficiency

Historically, quantum efficiency is an energy ratio between the input signal and the output or simply $\epsilon = \langle n_{\text{out}} \rangle / \langle n_{\text{in}} \rangle$, where $\langle n_{\text{out}} \rangle$ and $\langle n_{\text{in}} \rangle$ are the average photon numbers per pulse for the output and input mode, e.g. given time mode [52]. Knowing the efficiency, one can determine the validity of the memory for application in quantum repeaters and its ability to outperform the direct transmission. A noiseless memory could be thought of as an analog of an optical two-port beam-splitter, i.e., it restores the signal with a probability equal to an efficiency of the memory while admixing vacuum from a free port. Let us assume, that an input state for a such noiseless memory is a single photon state described by density matrix $|1\rangle\langle 1| \otimes \rho_{\text{in}}$, where ρ_{in} represents the density matrix of single photon degree of freedom used for quantum information encoding, e.g. polarization. Then an output of the memory can be represented as $((1 - \epsilon)|0\rangle\langle 0| + \epsilon|1\rangle\langle 1|) \otimes \rho_{\text{out}}$, for a completely noiseless memory the output reduced density matrix should be equal to an input $\rho_{\text{out}} = \rho_{\text{in}}$. Thus, the efficiency represents an upper limit of a possible achievable energy transfer, while this parameter does not include any information about a corruption of quantum information happening during the memory operation.

1.2.2 Fidelity

To quantify the change in the encoded quantum information after the storage, one can use an overlap between input and output quantum states. It is called fidelity and is generally found as $F = \left(\text{Tr}(\sqrt{\sqrt{\rho_{\text{in}}}\rho_{\text{out}}\sqrt{\rho_{\text{in}}}}) \right)^2$, where both input and output states are described

by density matrices ρ_{in} and ρ_{out} [2]. In this case ρ_{out} represents the post-selected reduced density matrices for a photonic degree of freedom, on which a useful quantum information is recorded, similarly to an above example with a single photon. By post-selection we mean, that an output density matrix is reconstructed only for cases when the memory has successfully emitted a photon. This is especially useful for characterization of quantum memory noise performance, where a qubit is encoded on orthogonal polarizational, spatial, angular momentum, frequency, or temporal modes [53]. If the input state is pure and represented by state $|\psi_{\text{in}}\rangle$, the fidelity simplifies to $F = \langle \psi_{\text{in}} | \rho_{\text{out}} | \psi_{\text{in}} \rangle$. It is worth noting, that in contrast to mentioned encoding, quantum information encoded in optical phase space and Fock basis experiences a decrease in fidelity by a factor equal to the efficiency [54].

Summarizing, a fidelity is not a universal metric of the quantum storage performance because of its state dependent nature. For this reason the state-independent benchmark was introduced [37]. It is called a $T-V$ diagram, as an analogy of transmission T and conditional variance δV used for describing a quantum channel [55]. The T coefficient represents a signal-to-noise ratio of a quantum channel, while the δV coefficient is a measure of the noise added to the output state.

1.2.3 Lifetime

The lifetime corresponds to the storage time of 50% decrease in efficiency. In a context of a quantum repeater, the lifetime is an effective time window during necessary quantum information operation—such as Bell-state measurements, purification, and photon transmission between the parties—can be implemented. In quantum repeaters a dominant time scale is set by a time required for photons to travel between the parties. Hence, the longer the lifetime is, the longer the possible communication distance potentially can be. Up-to-date the memory lifetime achieved is hundreds of milliseconds in the hot gas [56] with possible extension to a minute scale [57]. The laser cooled alkali atoms in optical dipole traps are capable of light storage on hyperfine coherence on the order of tens of seconds [58]. At

cryogenic temperatures, optically addressable nuclear spins of Non-Kramers ions in solids demonstrate coherence times ranging from a minute in $\text{Pr}^{+3}:\text{Y}_2\text{SiO}_5$ [59] to a few hours in $\text{Eu}^{+3}:\text{Y}_2\text{SiO}_5$ [60].

1.2.4 Multimodeness

An ability to store multiple optical modes allows to increase the rate of entanglement generation for quantum repeater [61]. In principle, the operation of quantum repeater could be based on different spatial [62, 63], polarization [64, 65], frequency or temporal modes [43] as well as combinations of any of them. In terms of cost-efficiency the implementation of temporal multimodeness may have the largest effect on the quantum entanglement generation rate increase [61].

1.2.5 Bandwidth

The bandwidth limits the maximum spectral width of the pulses that could be stored. It is defined as a full spectral width for a given relative efficiency reduction level [52]. The use of shorter pulses (which have larger bandwidth) allows faster performance of the memory, the corresponding delay-bandwidth product shows for how long the pulse can be stored in the units of the pulse duration. The gigahertz scale bandwidth were achieved in warm atomic vapor [66] and rare-earth ions [43].

1.3 Benchmark records

Let's consider memories which are most successful in fulfilling the mentioned requirements. All of the mentioned criteria should be considered in the context of the desired memory application. Among all the possible applications [67], quantum memory plays a central role for quantum communication and is an indispensable part of a quantum repeater. The use of memory in a quantum repeater for a given distance and desired entanglement

generation rate poses strong requirements on all of the above criteria [4, 68]. To be useful the overall fidelity¹ of the recalled qubit from the memory should be larger than the so-called no-cloning limit, which corresponds to the random guess [69] and is $2/3$ (or 66%). While the normalized fidelity in most of the implementations was higher than this value, getting efficiency above the no-cloning limit is the main problem [52]. In addition, an efficiency is of special importance for storing quantum information encoded in the continuous degrees of freedom, where a non-ideal efficiency decreases quantum properties of a state [70]. In contrast to this, optical qubits encoded in the discrete degrees of freedom have a decreased recall probability for the non-ideal efficiency without loss of quantum properties.

1.3.1 High efficiencies

The optimal strategy for achieving high efficiency is the use of perfect time reversal [11, 71], in other words the read-out and write-in operations should be identical up to an action of a time-reversal unitary operator. In theory, CRIB (or GEM), EIT, and Raman protocols can operate in the time-reversal regime. However, the time reversal requires the retrieval of the light into a backward direction, which may be challenging. The AFC and ROSE protocols violates the temporal reversibility, since Hamiltonians for the recall and storage are the same. It was shown that the violation of time reversibility can strongly affect the recovery efficiency in the case when the spectral width of the signal pulse becomes commensurate with the spectral width of the AFC structure [72].

Fundamentally, free-space AFC and ROSE protocols with forward reemission are limited by slightly more than 50% efficiency due to reabsorption. The backward scheme does not have such a problem, but it is difficult to realize because precise π pulse is needed. Overall, the most promising is to use the cavity-enhanced schemes for further improvement of the AFC protocol [73, 74, 75].

The efficiency above the no-cloning limit was achieved in most of protocols: 87% in GEM

¹efficiency multiplied by fidelity

[39], 92% in EIT [71], 80% in Raman [76] and 80% in DLCZ [77]. In all these experiments the fidelity was higher than measured efficiency, thus keeping the product of fidelity and efficiency above the non-cloning limit. The highest efficiency of 56% was demonstrated in AFC protocol in an impedance-matched cavity [73]. Thus this protocol seeks for further improvement to be useful for a quantum repeater.

1.3.2 Fidelity

All of the protocols claim to be noiseless and to provide a large fidelity. The ultimate experimental test of the fidelity is the storage of a non-classical quantum state, which is especially sensitive to noise. The nature of the DLCZ protocol equips it with the non-classical quantum states. Starting from the the first demonstrations [78] and further on [77] the DLCZ protocol proved to be operational in a quantum regime.

Due to compatibility between the DLCZ and the EIT in cold atoms the demonstration of non-classical storage was presented shortly in the EIT [79, 80], where the single photons prepared in the DLCZ were stored in an EIT medium. Later on, the EIT storage of the squeezed light generated by an optical parametric oscillator was presented [81]. The use of the quantum process tomography allowed to characterized the introduced noise by the memory [82] and revealed it to be on the order of 10^{-3} photons per pulse.

The storage of the correlated single-photon states from a spontaneous parametric down conversion source was demonstrated for AFC [42, 83, 84], where the fidelity of the recalled states was in the range from 70 to 90 %. The storage of non-classical quantum state of light was not performed in GEM. However, the result of small amplitude coherent state storage was used to claim the noiseless character of the memory with 98% fidelity [39].

The Λ system based memories are especially vulnerable to noise, since the strong control field may create an additional nonlinearities and produce an extra scattering. The effect of four-wave mixing (FWM) on an EIT memory performance and control field induced spontaneous Raman scattering was studied [85]. Later it was shown, that the radiation

limited broadening can reduced the negative effect of FWM noise [86].

1.3.3 Lifetime

The roadmap to long storage is the use of material with optically addressable hyperfine states with long coherence times. Nowadays, there are two major types of materials suitable for optical quantum memories, one of them are alkali gas, other are crystals doped with rare-earth ions. Alkali atoms naturally have the required atomic Λ scheme. At the same time, the rare-earth ions due to combination of large inhomogenous broadening and narrow homogeneous linewidth require special procedures for isolating homogeneous sub-ensembles² [88, 89].

For ATS, EIT and DLCZ it is preferable to have homogeneously broadened optical transition, thus these protocols are more favorable for implementation on the laser cooled alkali gas or specially prepared rare-earth ions. Raman and Λ -GEM memories are immune to inhomogeneous broadening on optical transition, as the use of large detuning compensates the effect of inhomogeneous broadening [90]. However, the small oscillator strength of rare-earth ions makes implementation of the Raman protocol on the whole inhomogeneous width difficult.

The storage with a lifetime exceeding hundreds of milliseconds was demonstrated in DLCZ [91, 92, 93], AFC [94], and EIT [95, 96, 59, 97] protocols. At the same time, the efficiency in these long storage time realizations was much less than the no-cloning limit with an exception for the cavity-enhanced DLCZ [92].

In several papers the long coherence lifetime was demonstrated for a macroscopically large nuclear spin coherence created by application of radio-frequency $\pi/2$ pulses [95, 60, 98]. The lifetime was extended by the use of dynamical decoupling series [95]. However, the storage of a single photon is prone to the fluctuation in the pulse area of a dynamical decoupling pulse and consequently resulting in much shorter actual lifetimes for the single photons [58, 99].

²The notable exception is rare-earth ions in stoichiometric crystal host [87], where the broadening is smaller than the hyperfine splitting of the ground state.

Therefore, if the long coherence lifetime exists, the ability to provide an efficient optical interface for storage on this coherence is the main problem of a quantum memory design.

1.3.4 Multimodeness

A possible multimode resource for atomic memories includes different polarization, time, frequency, spatial modes and angular-momentum degrees of freedom. However, for application in a quantum repeater the degrees of freedom should be efficiently convertible into ones used for multiplexing in fiber communication³, namely temporal, spatial and frequency degrees of freedom. The multimode capacity was demonstrated for AFC [43, 101], GEM [39, 102, 103], DLCZ [7, 8, 104, 105], and EIT [106, 107, 108, 109, 110]. Work [16] shows how a number of orthogonal time modes scales with an optical depth in each protocol. While the study shows that the multimodeness is possible for any protocol for large enough optical depth, the temporal multimodeness within a single QM unit is only practical for AFC, GEM, and a special version of DLCZ [111, 105, 112]. Among all of the protocols AFC has an advantage in multimode capacity, since its multimode capacity exploits natural inhomogeneous broadening.

1.3.5 Bandwidth

Bandwidths currently achieved range from several megahertz in EIT and DLCZ to a gigahertz in AFC. Bandwidth is determined mostly by an effective interaction rate. In EIT the bandwidth is determined by a transparency width window and the adiabaticity of the interaction, this limits bandwidth significantly. In Raman memory the bandwidth is the effective width of the Raman transition, which can be wide enough if the powerful control field is employed. The bandwidths from hundreds of megahertz to a gigahertz were demonstrated [66]. In AFC the storage is realized on the inhomogeneously broadened ensemble with the frequency span of few GHz, that potentially allows the use of this full bandwidth. Theoretical

³We exclude from consideration free space satellite-assisted schemes of the repeater [100]

proposal exists for storing sub-nanosecond pulses [113].

1.3.6 Current performance and perspective goal

Most of the protocols so far have demonstrated good performance only for a single criterion, but not all together in a single experiment. So far the best realizations include demonstration of cavity-enhanced DLCZ in optically trapped Rubidium 87 [92], where hundreds of milliseconds coherence lifetime in conjunction with an 76% efficiency was achieved. The EIT storage in praseodymium doped yttrium silicate with a lifetime of several seconds was demonstrated [59]. The efficiency of $\sim 75\%$ of this protocol in the same material was separately demonstrated by the same group [114]. However, high efficiency and long lifetime have not been demonstrated simultaneously in this crystal. Neither the quantum regime of storage has been implemented.

Moreover, two of the demonstrated high performance quantum memories use wavelength, which is not compatible with current telecom C or O bands. While the quantum wavelength conversion technique exists, its efficiency is relatively low $\sim 60\%$ [115, 116]. The only natural atomic candidate for the telecom C band compatible memory is Erbium. Recently it was shown [98], that at a large magnetic field (> 3 T) Erbium 167 doped in yttrium silicate has a spin coherence lifetime of a second. Thus, development of an efficient protocol for Erbium is of a special technological interest.

1.4 Conclusion and research impact

In this chapter, we considered promising quantum memory protocols. We listed the benchmarks that are requisite for quantum memory applications. Moreover, we named the best realizations of quantum memories up-to-date. We concluded that the current goal for a quantum memory is to outperform the classical transmission channel for which it is simultaneously required to have high fidelity and efficiency with a long lifetime. The

multimodeness is necessary for extending practical applications of the memories.

In Chapters 3, 4, and 6 we present newly proposed protocols, while in Chapter 5 the noise performance of a well-known gradient echo memory is studied. The first presented protocol, in Chapter 3, is the memory based on the cavity array with chirped frequency. The developed protocol opens a way for realization of the on-chip memory with whispering-gallery mode resonators and waveguides with an arbitrary storage times and large bandwidths. In addition to that, its reliance on the cavity makes it wavelength independent in contrast to the atomic based memories. Thus this design is applicable in a microwave domain for application in circuit quantum electrodynamics with a proper modification.

The second result (Chapter 4) is the proposed method for extending the bandwidth of the impedance matched cavity memory. While the method is general we propose to apply it for increasing a delay-bandwidth product for the atomic telecom memory by an order of magnitude.

The proposed protocol for the quantum random access memory is a new example of an atomic memory beyond the quantum repeater application. The proposed design significantly decreases the number of process units and the corresponding scalability issue by exploiting the time multimodeness of the atomic memory.

Chapter 2

Light-matter interaction

Most of the quantum memories are based on interaction of light and an atomic or atom-like system with a discrete spectrum. For the description of quantum memories we present the basic theory of light-matter interaction and apply it to a description of a free propagating field and a field constrained by a cavity mode.

2.1 Ensemble of two-level atoms

Depending on a quantum memory protocol usually two- or three-level systems are employed for realization of the memory. The state of an isolated single N -level atom can be simply described by wavefunction $|\Psi\rangle = \sum_{i=1}^N \alpha_i |i\rangle$, where $|i\rangle$ are the eigenstates of a free atomic system within truncated space of interaction interest.

2.1.1 Electric-dipole interaction

The interaction of atomic system with light is approximated by a dipole interaction [15]:

$$\hat{V} \approx -\hat{\mathbf{E}} \cdot \hat{\mathbf{d}}, \quad (2.1)$$

where $\hat{\mathbf{E}}$ is an electric field operator and $\hat{\mathbf{d}}$ is a dipole moment operator. The field propagating along z direction and having polarization \mathbf{e}_q can be expressed in terms of creation and annihilation operators [117]:

$$\hat{\mathbf{E}} = \sqrt{\frac{\hbar\omega_s}{2\epsilon_0 cS}} (e^{-i\omega_s t + ik_s z} \hat{a}(z, t) + \text{h.c.}) \mathbf{e}_q, \quad (2.2)$$

where ω_s and k_s are carrying frequency and wavevector respectively, and \mathbf{e}_q is the unit vector. Further we use the following notations of polarization unit vectors in spherical basis: $\mathbf{e}_{\pm 1} = \mp \frac{\mathbf{x} \pm i\mathbf{y}}{\sqrt{2}}$ and $\mathbf{e}_0 = \mathbf{z}$. For a classical field, i.e. field in a coherent state with large amplitude, the annihilation and creation operators can be replaced with complex number $\langle \hat{a}(z, t) \rangle \approx \langle \alpha \rangle$ [15]. In this case field amplitude operator $\hat{\mathbf{E}}$ simply becomes the classical wave with complex amplitude E :

$$\hat{\mathbf{E}} \approx (E \cdot e^{-i\omega_s t + ik_s z} + \text{h.c.}) \mathbf{e}_q. \quad (2.3)$$

For the derivation of the commutation relationship it is convenient to express the operator $\hat{a}(z, t)$ in the momentum space:

$$\hat{a}(z, t) = \int \frac{dk_z}{2\pi} \sqrt{\frac{\omega(k_z)}{k_s}} \hat{a}(k_z) e^{-i(\omega(k_z) - \omega_s)t + i(k_z - k_s)z}, \quad (2.4)$$

where operator $\hat{a}(k_z)$ obeys the usual bosonic commutation relationship

$$[\hat{a}(k_z), \hat{a}^\dagger(k'_z)] = 2\pi \cdot \delta(k_z - k'_z). \quad (2.5)$$

We find the commutation relationship for propagating field operator by using 2.5 together with expansion 2.4:

$$[\hat{a}(z, t), \hat{a}^\dagger(z', t)] = c \left(1 - \frac{i}{k_s} \frac{\partial}{\partial z} \right) \delta(z - z'). \quad (2.6)$$

Operator $\hat{a}^\dagger(z', t)\hat{a}(z', t)$ has a dimension of a photon number per second and the free Hamiltonian of the field is

$$\hat{H}_{f0} = \hbar k_s \int dz' \hat{a}^\dagger(z', t)\hat{a}(z', t). \quad (2.7)$$

Applying the commutator (2.6) reveals the Heisenberg equation of motion for $\hat{a}(z, t)$, which resembles the wave equation in the slowly varying envelope approximation:

$$\left(\frac{\partial}{\partial t} + c \frac{\partial}{\partial z} \right) \hat{a}(z, t) = -i\omega_s \hat{a}(z, t) + \frac{i}{\hbar} [\hat{V}, \hat{a}(z, t)]. \quad (2.8)$$

The collective dipole moment of the atomic system can be represented as the sum over individual atoms:

$$\hat{\mathbf{d}} = \sum_{k=1}^N \sum_{n \neq m} (\mathbf{d}_{nm} e^{-i\omega_{nm}t} |n\rangle_k \langle m|_k + \text{h.c.}), \quad (2.9)$$

where \mathbf{d}_{nm} is the dipole matrix element between the transition $|n\rangle \rightarrow |m\rangle$ and its value can be extracted from the radiation lifetime and the branching ratio as it is shown in Appendix A (Eq. A.5).

The resonant character of interaction between light and atoms allows to expand the dipole interaction into the interaction between the light and the dipole induced on the energetically closest transition. Here we consider an interaction between a single propagating quantum field and N two-level atoms with states $|n\rangle$ and $|m\rangle$. The corresponding Hamiltonian can be expressed in interaction picture as:

$$\hat{V} = \sqrt{\frac{\hbar\omega_s}{2\epsilon_0 c S}} \sum_{k=1}^N (e^{-i\omega_s t + ik_s z_k} \hat{a}(z, t) + \text{h.c.}) \left((\mathbf{d}_{nm} \cdot \mathbf{e}_q) e^{-i\omega_{nm}t} \hat{P}_{nm}^k + \text{h.c.} \right), \quad (2.10)$$

where $\hat{P}_{nm}^k = |n\rangle_k \langle m|_k$ is the projector from state $|m\rangle$ to state $|n\rangle$ for k 'th atom and ω_{nm} is the frequency of atomic transition. We use the rotating wave approximation neglecting the

energy non-conserving cross-terms oscillating on the sum of the atomic and field frequencies. This approximation is well tested and is valid for atoms having transitions in the visible range [33]:

$$\hat{V} \approx \sqrt{\frac{\hbar\omega_s}{2\epsilon_0 c S}} (\mathbf{d}_{nm} \cdot \mathbf{e}_q) \sum_{k=1}^N \left(\hat{a}(z, t) \hat{P}_{mn}^k e^{-i(\omega_s - \omega_{mn})t + ik_s z_k} + \text{h.c.} \right). \quad (2.11)$$

2.1.2 Rotating reference frame

The further simplification comes with an introduction of the rotating reference with frequencies of the atomic transitions, this makes the Hamiltonian independent of oscillatory terms. The introduction of the reference frame can be conveniently done via the following unitary transformation [118]:

$$\hat{V}_{\text{rf}} = \hat{U} \hat{V} \hat{U}^\dagger + i\hbar(\partial_t \hat{U}) \hat{U}^\dagger, \quad (2.12)$$

and the unitary transformation operator

$$\hat{U} = \prod_{k=1}^N e^{i(\omega_s - \omega_{mn})t \hat{P}_{mn}^k}. \quad (2.13)$$

After applying the Baker-Campbell-Hausdorff formula

$$e^{i\lambda\hat{G}} \hat{V} e^{-i\lambda\hat{G}} = \hat{V} + i\lambda[\hat{G}, \hat{V}] + \frac{(i\lambda)^2}{2!}[\hat{G}[\hat{G}, \hat{V}]] + \dots, \quad (2.14)$$

and in the rotating frame the Hamiltonian has the form:

$$\hat{V}_{\text{rf}} = \hbar \sum_{k=1}^N \left(\Delta \hat{P}_{mm}^k + g(\hat{a}(z, t) \hat{P}_{nm}^k e^{ik_s z_k} + \hat{a}^\dagger(z, t) \hat{P}_{nm}^k e^{-ik_s z_k}) \right), \quad (2.15)$$

where $\Delta = \omega_{mn} - \omega_s$ is the field-atom detuning, $g = \sqrt{\frac{\omega_s}{2\epsilon_0 \hbar c S}} (\mathbf{d}_{nm} \cdot \mathbf{e}_q)$ is the light-atom coupling constant, and we assumed $(\mathbf{d}_{nm} \cdot \mathbf{e}_q)$ to be a real number.

2.1.3 Uniformity of an ensemble and inhomogeneous broadening

For the sake of simplicity we assume atoms to be uniformly distributed along the volume of interest. Based on this we introduce the continuous atomic coherence and population operators in the form:

$$\hat{R}_{nm}(z, t) = \frac{1}{\sqrt{N}} \sum_k \hat{P}_{nm}^k \delta(z - z_k), \quad (2.16)$$

$$\hat{R}_{nn}(z, t) = \frac{1}{N} \sum_k \hat{P}_{nn}^k \delta(z - z_k), \quad (2.17)$$

with commutation relationship:

$$\left[\hat{R}_{mn}(z, t), \hat{R}_{nm}(z', t) \right] = \left(\hat{R}_{mm}(z, t) - \hat{R}_{nn}(z, t) \right) \delta(z - z'). \quad (2.18)$$

Assuming that the ensemble has a linear size L and density of atoms per unit of length is n the interaction of a two-level atomic ensemble and a free propagating field is expressed by means of

$$\hat{V}_{\text{rf}} = \hbar \int_{-L/2}^{L/2} dz \left(N \Delta \hat{R}_{mm}(z, t) + \sqrt{N} g \left(\hat{a}(z, t) \hat{R}_{nm}(z, t) e^{ik_s z} + \text{h.c.} \right) \right). \quad (2.19)$$

While the Hamiltonian (2.19) with a few modifications is useful for describing the dynamics of two-level atoms, most of the two-level quantum memory protocols, such as AFC, CRIB, and ROSE, are based on inhomogeneously broadened optical transitions. The inhomogeneity can be taken into account by dividing the whole ensemble into sub-ensembles with a given detuning Δ and introducing the normalized distribution of the inhomogeneous broadening $G(\Delta)$. One way to include this broadening into the system of equations is to modify the coherence operators $\hat{R}_{mn}(\Delta, z, t)$ to be parameterized by Δ . The commutation relationships

(2.18) are modified accordingly:

$$\left[\hat{R}_{mn}(\Delta, z, t), \hat{R}_{mn}(\Delta', z', t) \right] = \left(\hat{R}_{mm}(\Delta, z, t) - \hat{R}_{nn}(\Delta, z, t) \right) \delta(z - z') \frac{\delta(\Delta' - \Delta)}{G(\Delta)}. \quad (2.20)$$

All of the above transforms Hamiltonian (2.19) into

$$\hat{V}_{\text{rf}} = \hbar \int_{-\infty}^{\infty} d\Delta G(\Delta) \int_{-L/2}^{L/2} dz \left(N\Delta \hat{R}_{mm}(\Delta, z, t) + \sqrt{N}g \left(\hat{a}(z, t) \hat{R}_{mn}(\Delta, z, t) e^{-ik_s z} + \text{h.c.} \right) \right), \quad (2.21)$$

where operators $\hat{R}_{mn}(\Delta, z, t)$ and $\hat{R}_{nn}(\Delta, z, t)$ still have the dimensions of inverse length.

2.1.4 Heisenberg equations of motion

The basic requirement for further application of the two-level atoms for quantum memories is the linearity of the interaction and initial polarization of atoms, i.e., all N atoms are initially prepared in the ground state $\langle \hat{R}_{mm} \rangle \approx 1$ and $\langle \hat{R}_{mm} \rangle \gg \langle \hat{R}_{nn} \rangle$. These requirements bosonize the population. If these conditions are satisfied, the Heisenberg equations of motion are written as follows:

$$\left(\frac{\partial}{\partial t} + c \frac{\partial}{\partial z} \right) \hat{a}(z, t) = -i\sqrt{N}g \int_{-\infty}^{\infty} d\Delta G(\Delta) \hat{R}_{nm}(\Delta, z, t) e^{ik_s z}, \quad (2.22)$$

$$\frac{\partial \hat{R}_{nm}(\Delta, z, t)}{\partial t} = (-i\Delta - \gamma_{nm}) \hat{R}_{nm}(\Delta, z, t) - i\sqrt{N}g \hat{a}(z, t) e^{-ik_s z}, \quad (2.23)$$

where we have phenomenologically introduced the decay of coherence rate γ_{nm} . The presence of a decay constant should be accompanied by a stochastic quantum operator [15]. For the sake of simplicity we neglect this term here, although it will be introduced and studied in Chapter 5.

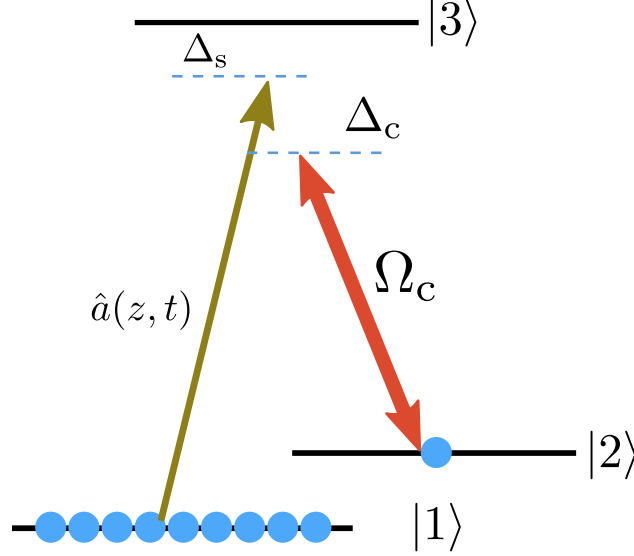


Figure (2.1) General three level diagram. Quantum field $\hat{a}(z, t)$ could be saved as a coherence between two lowest levels $|1\rangle$ and $|2\rangle$. Δ_s and Δ_c are detunings of the quantum field and the control field (Ω_c) frequencies from the corresponding transition.

2.2 Λ system-based

The quantum memories employing Λ atomic system mainly use one strong coherent field and a weak probe field, as shown in Figure 2.1. The strong coherent field controls atomic susceptibility that eventually allows to map the state of incoming field into a long-lived coherence.

2.2.1 Heisenberg equations of motion

We consider a three-level Λ atomic system interacting with classical control field acting on transition $|2\rangle \rightarrow |3\rangle$ with Rabi frequency $\Omega_c = \frac{\mathbf{d} \cdot \mathbf{E}_c}{\hbar}$ and wave number k_c . A weak quantum field described by annihilation operator $\hat{a}(z, t)$ with wave number k_s acts on transition $|1\rangle \rightarrow |3\rangle$. An effective Hamiltonian for such a system can be found analogously to (2.19) and has

a form

$$\begin{aligned} \hat{V}_{\text{rf}} = \hbar \int_{-L/2}^{L/2} dz \left(\sqrt{N}g \left(\hat{a}(z,t) \hat{R}_{31}(z,t) e^{ik_s z} + \text{h.c.} \right) + \left(\Omega_c(z,t) \hat{R}_{32}(z,t) e^{ik_c z} + \text{h.c.} \right) \right) - \\ - \hbar N \int_{-L/2}^{L/2} dz \left(\Delta_s \hat{R}_{11}(z,t) + \Delta_c \hat{R}_{22}(z,t) \right). \end{aligned} \quad (2.24)$$

The system of Heisenberg equations for the operators are found in analogy with the two-level atom in a presence of an inhomogeneous broadening of level $|3\rangle$ (Eqs. 2.22–2.23):

$$\left(\frac{\partial}{\partial t} + c \frac{\partial}{\partial z} \right) \hat{a}(z,t) = -i\sqrt{N}g \int_{-\infty}^{\infty} d\Delta G(\Delta) \hat{R}_{13}, \quad (2.25)$$

$$\frac{\partial \hat{R}_{13}}{\partial t} = -i(\Delta_s + \Delta) \hat{R}_{13} - i\sqrt{N}g \hat{a}(z,t) \left(\hat{R}_{11} - \hat{R}_{33} \right) - i\Omega_c(z,t) \hat{R}_{12}, \quad (2.26)$$

$$\frac{\partial \hat{R}_{23}}{\partial t} = -i(\Delta_c + \Delta) \hat{R}_{23} - i\sqrt{N}g \hat{a}(z,t) \hat{R}_{21} - i\Omega_c(z,t) \left(\hat{R}_{22} - \hat{R}_{33} \right), \quad (2.27)$$

$$\frac{\partial \hat{R}_{12}}{\partial t} = -i(\Delta_s - \Delta_c + \Delta) \hat{R}_{12} + i\sqrt{N}g \hat{a}(z,t) \hat{R}_{32} - i\Omega_c(z,t) \hat{R}_{13}, \quad (2.28)$$

where the annihilation operator and Rabi frequency absorbed the wave vector phase factor, as such $\hat{a}(z,t) e^{ik_s z} \rightarrow \hat{a}(z,t)$. The inhomogeneous broadening is represented by random value Δ , which is assumed to have normalized probability distribution function $\int_{-\infty}^{\infty} d\Delta G(\Delta) = 1$. We have omitted notation that states the dependence of coherence operators on the parameters $\hat{R}_{mn}(\Delta, z, t) \rightarrow \hat{R}_{mn}$.

This is a general system of equations capable of describing EIT, Raman, fast memory, and others both homogeneously and inhomogeneously broadened. Usually the system is linearized, i.e., the terms which are proportional to multiplication of two operators are neglected. For this, all atoms are assumed to populate a single level, thus $\hat{R}_{22} \approx \hat{R}_{33} = 0$ and $\hat{R}_{11} \approx 1$. Furthermore, terms proportional to a quantum field operator multiplied by a coherence operator ($\propto \hat{a}(z,t) \cdot \hat{R}_{mn}$) are of the second order of perturbation and could be neglected [11].

2.2.2 Cavity enhancement

For cavity enhanced scheme the description is slightly different due to the presence of a single mode instead of continuum as in free space. Next we consider a single-sided cavity, which is a good approximation for a cavity formed by mirrors with significant difference in reflection.

The cavity mode interaction with free space field in the limit of high quality factor, i.e. cavity linewidth is much smaller than a free spectral range, can be described by the input-output formalism [119]. It allows to conveniently separate free space field into two components: the incident on cavity (or input free space field) and reflected from the cavity (or output field). The cavity field amplitude is related to the free space input and output by the following expression:

$$\hat{a}_{\text{in}} + \hat{a}_{\text{out}} = \sqrt{\kappa}\hat{a}, \quad (2.29)$$

where κ is the inverse photon lifetime in the cavity, $\hat{a}_{\text{in(out)}}$ represents input (output) free space field. The interaction of the cavity with the media inside can be described by the Heisenberg equation of motion written for the cavity annihilation operator:

$$\frac{d\hat{a}}{dt} = -i \left[\hat{V}_{\text{int}}, \hat{a} \right] + \sqrt{\kappa}\hat{a}_{\text{in}}. \quad (2.30)$$

The interaction Hamiltonian \hat{V}_{int} for a cavity and N two-level atoms almost coincides with the one used in a free space Eq. 2.15, with a key difference of replacing interaction volume in constant g with effective volume of the cavity mode V :

$$g = \sqrt{\frac{\omega_s}{2\hbar\epsilon_0 V}} (\mathbf{d}_{nm} \cdot \mathbf{e}_q), \quad (2.31)$$

If a standing wave is formed in the cavity mode, the interaction constant longitudinally may vary from atom to atom, which is true for a Fabry-Perot cavity. On the contrary, a ring

cavity allows uniform coupling for the whole ensemble. The resulted interaction Hamiltonian is:

$$\hat{V}_{\text{int}} = \hbar \sum_{k=1}^N \left(g^j (\hat{a} \hat{P}_{nm}^k e^{ik_s z_k} + \hat{a}^\dagger \hat{P}_{nm}^k e^{-ik_s z_k}) \right). \quad (2.32)$$

Similarly the interaction with the Λ system can be expressed as in (2.24) with the replacement of the continuous quantum field on the cavity field and introduction of the input and output fields. The resulted equation can be used for description of cavity enhanced memory protocol such as Raman, EIT, DLCZ or impedance matched echo protocols.

2.3 Conclusion

In this chapter we introduced the mathematical framework that describes interaction between ensemble of atoms and quantum fields. We have considered separately: two-level and three-level atoms, atoms interacting with a free space fields and atoms interacting with a field confined in a cavity. We discussed how to mathematically include an inhomogeneous broadening. The same system of equations are going to be generalized to find quantum noises accompanying quantum memories.

Chapter 3

All-optical photon echo and memory on a chip

3.1 Introduction

A photon echo [120, 121] is a broad class of optical phenomena when a coherence induced in a quantum system by an optical field is emitted in a form of a well-resolved intense optical signal, similar to the spin echo in nuclear magnetic resonance. Over decades photon echo has been proven to be a powerful method of coherent spectroscopy, providing unique information on transient processes in gases, liquids, and solids [122]. As an example, photon-echo revivals in molecular rotational coherences have been shown to enable efficient quantum control of molecular alignment [123], photochemical reactions [124], as well as synthesis of ultrashort field waveforms [125]. Together with that photon echo is a promising strategy for quantum data storage [31, 39, 51, 126, 127, 128, 129].

Here we show that a photon echo can be implemented by purely optical means using an array of on-chip high-finesse ring cavities whose parameters are chirped in order to support equidistant spectra of cavity modes. Classical or quantum optical signal, launched into such a system, becomes distributed between individual cavities, giving rise to the coherence

revivals at well-defined delay times, controlled by the chirp of cavity parameters. This effect enables long storage times for high-throughput broadband optical delay and consequentially quantum memory. The proposed scheme is notably different from the conventional and silenced [130] photon echo by an absence of the applied π -pulse, which is harmful due to spontaneous emission. Thus the scheme is of special value for quantum protocols, where only a few excitations in the media exist and the excessive noise due to a π -pulse is especially harmful [47].

While the proposed way of light storage is conceptually similar to the AFC protocol [40], the waveguide-cavity coupling provides an advantage. We show that optimal coupling between cavity and waveguide exists and ensures complete conversion of the input field into the superposition of the cavity excitations. It contrasts with AFC, where an infinite optical depth is required for complete conversion of input light into the atomic excitation. In that sense our scheme resembles AFC in an impedance matched optical cavity [131], where a complete conversion is possible. In this chapter we find a condition when this scheme can work as a classical delay line and an efficient QM. Moreover, we discuss possible experimental implementations and further development of the protocol for a long lived storage.

3.2 Proposed scheme

We consider an array of N single-mode high-finesse chirped cavities with an equidistant spectrum of modes with mode spacing Δ (Fig. 3.1). An optical field coupled into such an array remains distributed between the cavities until all of them can re-emit in phase, giving rise to intense photon-echo signals at the output. With appropriate coupling between the nanofiber and the cavities, which is possible, e.g., with a fiber tapered to a submicron diameter [132, 133, 134], the entire field stored in the cavity array can be retrieved within the first echo signal with a time delay $t_{\text{echo}} \cong 2\pi/\Delta$.

In the considered chirped ring-cavity (CRC) scheme (or frequency comb all-pass filter),

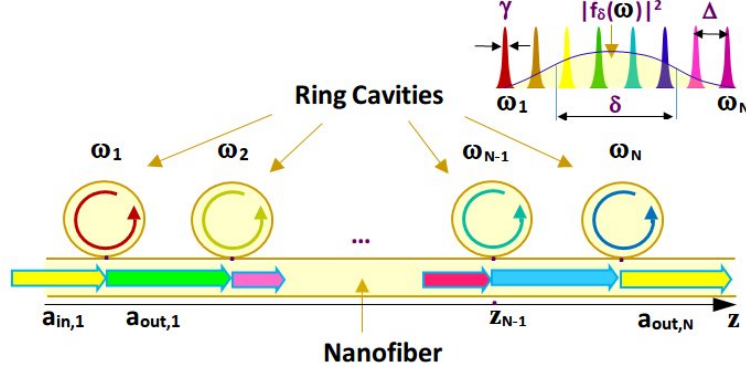


Figure (3.1) An array of chipped ring cavities coupled to a common optical fiber. The spectrum of cavity modes $\omega_n = \omega_o + n\Delta$ with $\gamma < \Delta$ is shown in the inset. The spectrum of the input signal with a bandwidth δ is shown by the solid blue line.¹

the spectrum of cavity modes is equidistant and consists of narrow lines centered at cavity eigenfrequencies ω_n : $\omega_n = \omega_0 + n\Delta - i\gamma_n$, where $\gamma_n < \Delta$ is the n th mode linewidth, and $n = 0, 1, \dots, N-1$. Further on, we consider non-Hermitian free Hamiltonian for the cavities, where the finite lifetime of the photon is included as an imaginary frequency. The Hamiltonian of the CRC system is written as $\hat{H} = \hat{H}_c + \hat{H}_f + \hat{V}$, where $\hat{H}_c = \hbar \sum_{n=1}^N \omega_n \hat{b}_n^\dagger(\omega) \hat{b}_n(\omega)$ is the Hamiltonian of N ring cavities, $\hat{H}_f = \hbar \int d\omega \omega \hat{a}^\dagger(\omega) \hat{a}(\omega)$ is the Hamiltonian of optical-fiber modes, and

$$\hat{V} = \hbar \sum_{n=1}^N \int d\omega (g_n \hat{b}_n^\dagger(\omega) \hat{a}(\omega) e^{ik_\omega z_n} + g_n^* \hat{b}_n(\omega) \hat{a}^\dagger(\omega) e^{-ik_\omega z_n}) \quad (3.1)$$

is the cavity-fiber interaction Hamiltonian, with z_n being the coordinate of the n th cavity ($z_n \neq z_m$ for $n \neq m$) and $\hat{a}(\omega)$, $\hat{a}^\dagger(\omega)$, $\hat{b}_n(\omega)$, and $\hat{b}_n^\dagger(\omega)$ being bosonic annihilation and creation operators of the optical-fiber and cavity modes.

An input optical light field is launched into the CRC system at the time moment $t = 0$ along the z axis as shown in Figure 3.1. Applying the input-output formalism [134, 33] for the interaction of the light field with ring-cavity modes, which are assumed to be in the ground state at a room temperature, we arrive at the following set of equations for the field

¹The figure and the caption were created by S.A. Moiseev.

amplitude inside n th cavity:

$$\frac{d\hat{b}_n(\omega)}{dt} = -(i\omega_n + \kappa_n/2 + \gamma_n)\hat{b}_n(\omega) + \sqrt{\kappa_n}\hat{a}_{\text{in},n}(\omega). \quad (3.2)$$

To find the field amplitudes for each cavity $\hat{b}_n(\omega)$ and fiber $\hat{a}_{\text{in},n}(\omega)$, we use the condition $\hat{a}_{\text{in},n}(\omega) + \hat{a}_{\text{out},n}(\omega) = \sqrt{\kappa_n}\hat{b}_n(\omega)$ [119], where κ_n is a coupling constant of the n th cavity mode with the nanooptical fiber. Additionally, the fiber fields before and after the interaction with the n th cavity are related as $\hat{a}_{\text{in},n+1}(\omega) = e^{-ik(z_{n+1}-z_n)}\hat{a}_{\text{out},n}(\omega)$, where an intermediate position is $z_{n+1} > z > z_n$. Applying conditions from the above and Fourier transformation $\hat{b}_n(t) = \int d\omega \hat{b}_n(\omega)e^{-i\omega t}$ and $\hat{a}_{\text{in},n}(t) = \int d\omega \hat{a}_{\text{in},n}(\omega)e^{-i\omega t}$ to Eq. (3.2), we find the fiber field:

$$\hat{a}_{\text{out},n}(\omega) = -\frac{\kappa_n/2 - \gamma_n - i(\omega_n - \omega)}{\kappa_n/2 + \gamma_n + i(\omega_n - \omega)}\hat{a}_{\text{in},n}(\omega). \quad (3.3)$$

Generalizing this formula for the whole array we find the output fiber field

$$\hat{a}_{\text{out},N}(\omega, z > z_N) = e^{ik_\omega(z-z_N)}U_\omega^N\hat{a}_{\text{in}}(\omega), \quad (3.4)$$

where

$$U_\omega^m = (-1)^m e^{ik_\omega(z_m-z_1)} \prod_{n=1}^m \frac{\kappa_n/2 - \gamma_n - i(\omega_n - \omega)}{\kappa_n/2 + \gamma_n + i(\omega_n - \omega)}, \quad (3.5)$$

determines the fiber mode amplitude behind the m th cavity. We use new notation $\hat{a}_{\text{in}}(\omega) = \hat{a}_{\text{in},1}(\omega, z_1)$ for the Fourier-transformed input field. Following the same line of derivations we find n th cavity mode amplitude

$$\hat{b}_n(t) = \int d\omega \beta_n(\omega) U_\omega^{(n-1)} e^{-i\omega t} \hat{a}_{\text{in}}(\omega) \quad (3.6)$$

with $\beta_n(\omega) = \frac{\sqrt{\kappa_n}}{\kappa_n/2 + \gamma_n + i(\omega_n - \omega)}$.

As can be seen from Eqs. 3.4 and 3.5 the output field is independent from the order

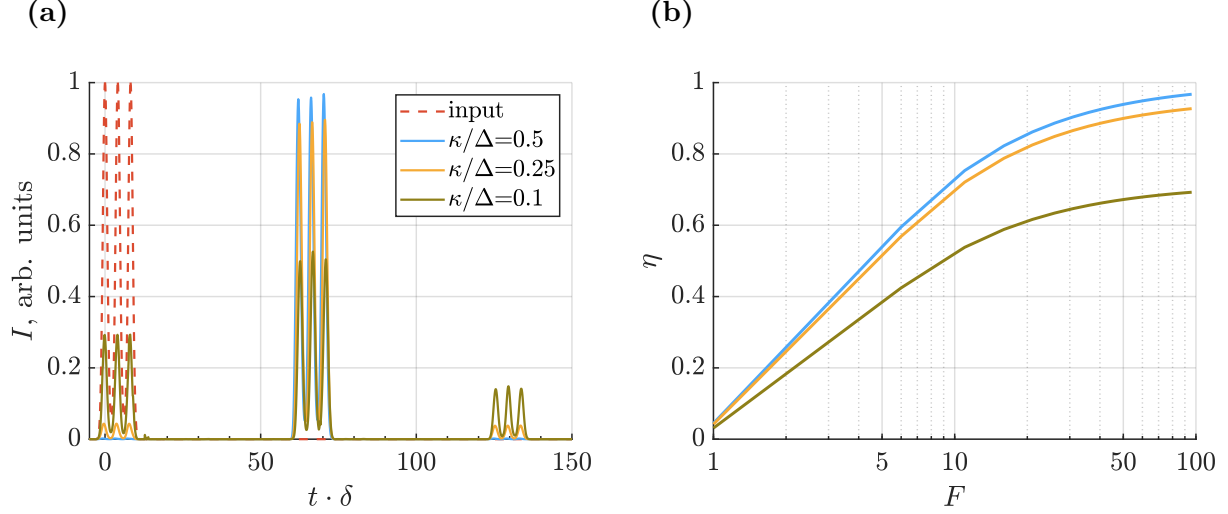


Figure (3.2) (a) The input and output field intensities ($I = |A_{\text{in}}(t)|^2, |A_{\text{out}}(t)|^2$) as functions of time (in units of δ^{-1}) for a three-pulse input field (left dashed red curve) for $\kappa/\delta = 0.01$ (green line), 0.025 (yellow line), and 0.05 (blue line). The mode spacing is $\Delta = 0.1\delta$. The finesse of ring cavities is $F = 50$, number of cavities $N = 61$. (b) Quantum efficiency η echoes of signal retrieval as a function of the cavity finesse F for a Gaussian pulse in a cavity array with $N = 61$. The mode spacing and coupling constants are the same as in (a). The efficiency is calculated over all possible echoes.

in which the cavities are arranged in the array. For a single-photon initial state $|\psi_\delta\rangle = \int d\omega f_\delta(\omega) \hat{a}_{\text{in}}^\dagger(\omega) |\emptyset\rangle$, where $|\emptyset\rangle$ is the vacuum state and $f_\delta(\omega)$ is the wave-function normalized by $\int d\omega |f_\delta(\omega)|^2 = 1$ with bandwidth δ , the probability amplitude of the output light field $A_{\text{out}}(t, z) = \langle \emptyset | \hat{a}_{\text{out},N}(t, z) | \psi_\delta \rangle$ is given by

$$A_{\text{out}}(t, z) = \int d\omega e^{-i(\omega t - k_\omega(z - z_N))} U_\omega^N f_\delta(\omega). \quad (3.7)$$

In Figure 3.2a, we plot the output field amplitude $A_{\text{out}}(t)$ calculated for a three-pulse input signal as a function of time for three different values of the coupling constant κ and fixed decay rate γ , with $\kappa = \kappa_1 = \dots = \kappa_N$, $\gamma = \gamma_1 = \dots = \gamma_N$. The cavities are qualified with two parameters: finesse defined as $F = \Delta/(2\gamma)$ and the cavity quality factor $Q = \omega_0/(2\gamma)$. In the regime of weak coupling, $\kappa \ll \Delta$, some fraction of the input light is transmitted through the entire CRC system, experiencing no delay, giving rise to a signal at $t \approx 0$ in Figure 3.2a.

The remainder of the input field is distributed between the first, second, and subsequent echo signals, observed at t_{echo} , $t_{\text{echo},2} \approx 2t_{\text{echo}} = 4\pi/\Delta$, and $t_{\text{echo},n} \approx nt_{\text{echo}}$, respectively.

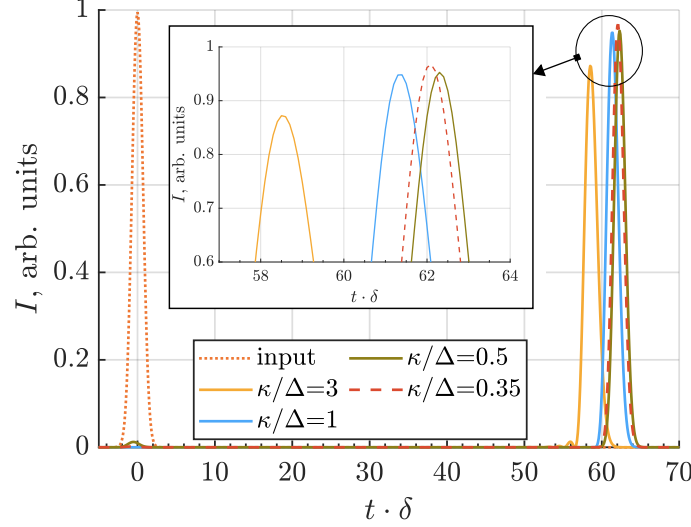


Figure (3.3) Intensities of the input signal pulse and retrieved echo pulses ($I = |A_{\text{in}}(t)|^2$, $|A_{\text{out}}(t)|^2$) for ring cavity QM vs coupling constant κ ; spectral distance $\Delta = 0.1\delta$, number of cavities $N = 61$, $\gamma = 10^{-4}\delta$ (finesse $F = \Delta/(2\gamma) = 500$), δ is a spectral width of the input light pulse.

Remarkably, the storage time in the considered cavity array is mainly determined by the frequency spacing Δ , but is also sensitive for large enough coupling constant $\kappa > \Delta/2$. The change in the recall time is depicted in Figure 3.3 for different coupling constants. The presented advance of the pulse recall for a large coupling constant is due to the faster formation of coherence in the ‘overcoupled’ cavities. The resulting recall time is modified as

$$t_{\text{echo}} \sim \frac{2\pi}{\Delta} - \frac{\kappa}{\Delta\delta}.$$

We can define quantum efficiency $\eta(t)$ of the field retrieved in the first echo pulse as

$$\eta(t) = \frac{\int dz A_{\text{out}}^*(t, z) A_{\text{out}}(t, z)}{\int dz A_{\text{in}}^*(t_0, z) A_{\text{in}}(t_0, z)}, \quad (3.8)$$

where $A_{\text{in}}(t_0, z) = \langle \emptyset | \hat{a}_{\text{in}}(t_0, z) | \psi_\delta \rangle$ is the input field amplitude. Calculations presented in Figure 3.2b show that for a finesse higher than 50 the first echo provides signal retrieval with efficiency more than 90%. As can be seen in Figures 3.2a and 3.2b coupling constants

κ close to 0.5Δ are required for efficient signal retrieval.

3.3 Comparison with other protocols

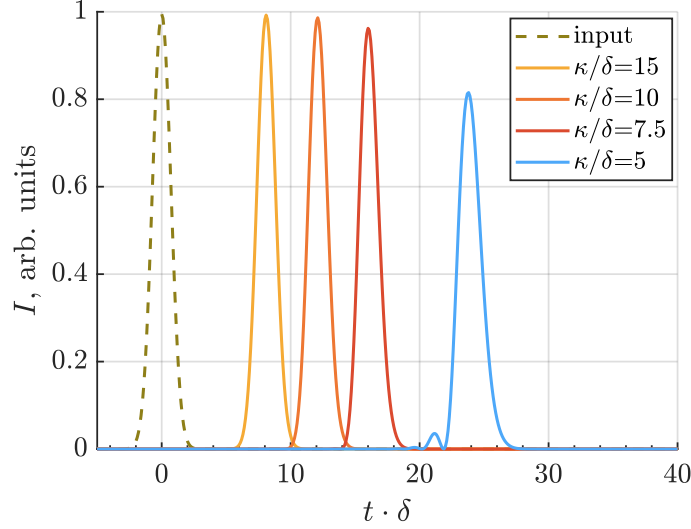


Figure (3.4) Intensities of the input and output light pulses ($I = |A_{\text{in}}(t)|^2, |A_{\text{out}}(t)|^2$) in the SCISSOR scheme [135] for different coupling constants normalized to the spectral width of signal pulse κ/δ shown in the legend; number of cavities $N = 61$, all the cavities have equal frequencies (i.e., $\Delta = 0$), $\gamma = 10^{-4}\delta$, δ is a spectral width of the input light pulse. The presented time delay is totally due to the interaction between the cavities and the incoming pulse.

We emphasize that, while the CRC array considered here stores light—classical or quantum—in the form of a field distributed between individual cavities, its ability to provide long storage times is due to periodic coherence revivals, occurring at the instants of time when the fields circulating in individual cavities are all emitted in phase. In this respect, it is instructive to compare the delay-line performance of the CRC-array scheme considered here with a delay-line architecture based on all-pass filter called also as a side coupled integrated spaced sequence of resonators (SCISSOR) [135, 136, 137]. In contrast to the CRC-array, SCISSOR scheme consists of the ring cavities with equal central frequencies. The SCISSOR technique and the coupled resonator optical waveguide (CROW) configuration [138] are two

complementary basic standards of an on-chip integrated optical delay line [139, 140, 141], the principle schemes for both delay lines are presented in Figure 3.5.

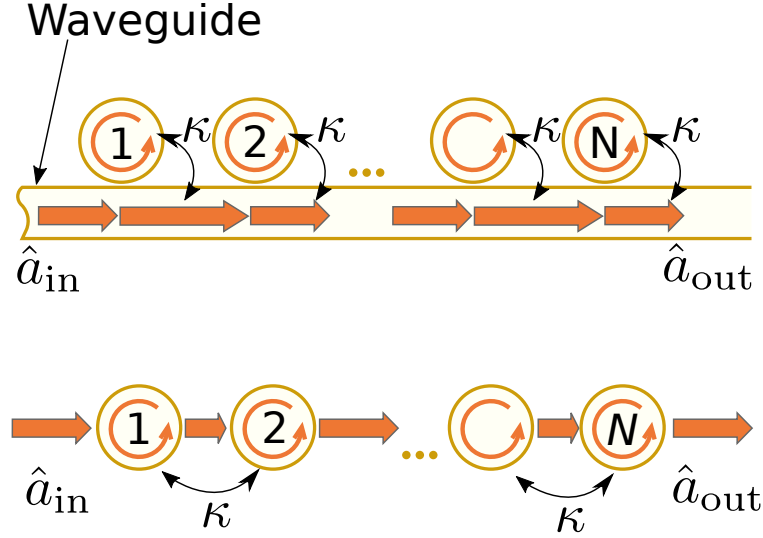


Figure (3.5) The principle schemes of SCISSOR (above) and CROW (below). SCISSOR consists of an array of identical cavities coupled to a common waveguide. The input light \hat{a}_{in} from the coupling fiber enters the first resonator, where it is delayed by the time proportional to the inverse coupling constant κ . The procedure is repeated N times, where N is number of resonators. CROW consists of a resonator array with closest neighbours being coupled to each other. The input light experiences reduced group velocity due to large dispersion of the array. An overall delay is the same for both schemes $\sim N/\kappa$.

Time delay in both schemes is mainly determined by their bandwidth windows where an effective group velocity of light can be reduced to $c/100$. Herein, CROW, where the ring cavities are coupled to each other without additional common optical fiber, can work within wider spectral range even in the presence of weak coupling between the resonators (i.e., $\delta \gg \kappa$). In addition, while SCISSOR scheme can demonstrate a longer time delay, it is associated with relatively higher losses, which are caused by a significant role of resonant interaction with the light field. Below we show that the CRC-array scheme can considerably exceed the basic characteristics of SCISSOR scheme and reach properties close to the CROW scheme.

A comparison of CRC and SCISSOR schemes shows (see Figures 3.3, 3.4 and Tables 3.1, 3.2) that both schemes can provide comparable efficiencies, $\eta \approx 95\%$ for the same input light

pulses. Moreover, both schemes can provide a superb fidelity, with the shape of the retrieved signal accurately following the shape of the input pulse (Figures 3.2a, 3.3, and 3.4). Finally, the coupling constants needed to achieve comparable delay times are much lower for CRC arrays. Additionally, for comparable efficiencies the delay times provided by a CRC array are substantially longer than the delay times attainable with the SCISSOR design.

Specifically, calculations presented in Figures 3.3 and 3.4 give $\tau \approx 2\pi/\Delta \approx 62.8/\delta$ for the CRC array with $\kappa = 0.05\delta$ versus $\tau \approx 16.8/\delta$ for SCISSOR with $\kappa = 7.5\delta$. Large difference in the coupling constants κ follows from the fact that maximum bandwidth δ of SCISSOR scheme is determined by the coupling constant of an individual resonator (or loaded Q-factor), while the total group delay results from a summation of the delays of all individual resonators. In turn, CRC can provide larger time delay for broadband light pulses of an order $t \approx 2\pi/\Delta \gg \delta^{-1}$ due to the presence of spectral frequency combs $N\Delta \geq \delta$ for relatively weak coupling $\kappa \ll \delta$. Accordingly, the predominant interaction of signal fields with CRC array occurs for the off-resonant condition with the ring cavity modes that will provide lower losses similar to CROW.

CRC scheme can be used for noiseless quantum storage due to its passive nature. In contrast to a free space AFC protocol [126], the described CRC scheme uses purely optical tools and can operate at a room temperature. It is also important that the CRC scheme provides an efficient light retrieval in a forward direction that allows practical implementation with high quantum efficiency. At the same time, a conventional AFC-protocol works efficiently only for backward light retrieval that requires the use of additional control laser pulses. Another unobvious property of the CRC scheme is an efficient quantum storage at the optimal coupling $\kappa = 0.5\Delta$ that distinguishes this scheme from the free space AFC protocol [126] and from its recent spatial-frequency version [142].

The optimal coupling makes the CRC protocol similar to the impedance matching QMs [131, 50, 143], although CRC does not use any common single mode resonator providing an optimal coupling with all the CRC modes. This property exposes another physical nature in

the emergence of optimal conditions in the CRC scheme and in the quantum random-access memory [144] indicating the possibility of more common manifestation of the impedance matching effects for light field evolution in the integrated optical devices.

3.4 Possible experimental implementations

The proposed purely optical scheme can be experimentally implemented with whispering gallery modes of the ring cavities [132] or by using an on-chip approach [145]. The cavities from these works [132] and [146] are characterized by very high intrinsic quality factors, $Q = 10^8$ and $Q = 10^{10}$, while the cavities can still be efficiently coupled to a nanofiber [147]. Below we analyze a possible implementation of CRC by means of on-chip array of ring cavities [146].

Following work [146], we choose the parameters of a single-mode ring cavity: $\omega_0 = 2\pi \cdot 200$ THz (telecommunication band $\lambda = 1.5 \mu\text{m}$), cavity diameter $D = 90 \mu\text{m}$, free spectral range $\omega_{\text{FSR}} = 2\pi \cdot 790$ GHz, and linewidth $\gamma_n = \gamma = 1/(2\tau_{\text{crit}}) = 2\pi \cdot 1.6$ MHz determined by an intrinsic quality factor $Q = 1.25 \cdot 10^8$. By taking into account that total number of the cavities can be as high as a hundred [139], we pick an intermediate number $N = 61$ that determines a maximum intermode spacing to be $\Delta = \omega_{\text{FSR}}/60 = 2\pi \cdot 13.16$ GHz.

The optimal coupling constant $\kappa = \Delta/2 = 2\pi \cdot 6.58$ GHz (see Figure 3.3) can be obtained experimentally by tuning distance between the microcavities and a waveguide [139]. For instance, n th cavity could have spectral detuning of $n\Delta$ by using slightly different diameter $D_n \cong D - n\Delta D/\omega_0$ (where $\Delta D/\omega_0 = 7.37 \cdot 10^{-4}D = 63$ nm). The precision of 63 nm is attainable by the current nanooptical technologies [134]. Other ways to realize an arbitrary spectral offsets $n\Delta$ for microresonators are thermo-optics, electro-optics, or free-carrier dispersion control, which varies refraction index [139, 148].

As an evaluation of light pulse retrieval efficiency we use numerical results with mode spacing ten times smaller than the bandwidth of the input light $\Delta = 0.1\delta = (10t_s)^{-1}$.

Q	t_s	$t_{\text{delay, SCISSOR}}$	$t_{\text{delay, CRC}}$
10^8	1.2 ps	20.2 ps	75.4 ps
	32 ps	0.54 ns	2 ns
10^{10}	0.12 ns	2.02 ns	7.54 ns
	3.2 ns	54 ns	0.2 μ s

Table (3.1) Time delay of the retrieved pulse in SCISSOR- and CRC schemes with quantum efficiency $\eta \approx 0.95$ related to the results of Figures 3.4, 3.3 for two intrinsic quality factors Q ; coupling constant $\kappa = 7.5\delta$ for SCISSOR and $\kappa = 0.05\delta$ for CRC scheme, $\delta = t_s^{-1}$ is a spectral width of the signal pulse, t_s - its temporal duration, $\delta = 10\Delta$, number of microcavities $N=61$, finesse $F = 500$.

However, the spectral width of light pulse $\delta = t_s^{-1}$ can also be in the range from few Δ to several dozen of Δ . By using two possible intrinsic quality factors ($Q = 10^8$ and $Q = 10^{10}$), we find the time delays t_{delay} for the same quantum efficiency $\eta \approx 0.95$ of SCISSOR and CRC schemes. This data is also summarized in Table 3.1. Efficient quantum storage is possible for pico- and nanosecond pulses where time delays in CRC scheme can reach $t_{\text{echo}} \cong 2$ ns (for $t_s = 32$ ps and $Q = 10^8$) and $t_{\text{echo}} \cong 0.2$ μ s (for $t_s = 3.2$ ns, $Q = 10^{10}$).

Additional time delay of light pulse due to propagation in the common optical fiber, being 6 mm long² with refractive index 1.5, will be ≈ 30 picoseconds. This time delay is 60 or $6 \cdot 10^3$ times shorter than t_{delay} in CRC scheme for quality factors $Q = 10^8$ and $Q = 10^{10}$. This is a significant advantage of CRC for on-chip optical schemes in comparison with a usual SCISSOR scheme.

Storage time in the CRC scheme $t_{\text{echo}} \cong 2\pi/\Delta$ can be further increased for the cavities with smaller frequency spacing Δ (i.e., for lower finesse F) but at the expense of reducing the quantum efficiency. We summarize the numerical data results, presented in Fig. 3.2b, in Table 3.2, where we provide possible time delays for the CRC scheme with appropriate quantum efficiencies. From this data it is seen that the time delay reaches $t_{\text{delay}} \cong 334.7$ ns for the light pulse duration $t_s = 5.33$ ns, quality factor $Q = 10^8$, and quantum efficiency $\eta \approx 0.35$. For higher quality factor, $Q = 10^{10}$, the time delay can reach 33.5 μ s. This time delay is shorter by one order of magnitude than the light lifetime in a single ring cavity. It

²Spatial size of the described array consisting of 61 cavities can be estimated as $L = 60 \cdot 100$ μ m=6 mm, where 100 μ m is the distance between the centers of two nearest cavities.

Q (CRC)	F	η	t_s	t_{delay}
10^8	10	0.72	1.6 ns	100.5 ns
	3	0.35	5.33 ns	334.7 ns
10^{10}	10	0.72	0.16 μs	10.05 μs
	3	0.35	0.533 μs	33.5 μs

Table (3.2) Time delay of the retrieved pulse in CRC schemes in accordance with results of Figs. 3.2b for two different finesse: $F = 3$ and $F = 10$ and for two quality factors Q ; coupling constant $\kappa = 0.05\delta$, $\delta = 10\Delta$ ($\delta = t_s^{-1}$), $N=61$.

is worth noting new nanooptical technologies which could be useful for fabrication of the studied CRC scheme. For example, it may be monolithic semiconductor microcavities and cavity arrays in photonic crystals and other materials [134, 139].

3.5 Conclusion and discussion

We have shown that a system of frequency comb ring cavities coupled to a nanofiber can be used for implementation of on-chip broadband delay line operating at room temperature. In comparison with usual SCISSOR configuration [135, 136, 137], the proposed CRC scheme provides longer temporal delay with much weaker coupling constant—two orders of magnitude—between the cavities and optical fiber and it promises lower losses in practice. Moreover, the CRC scheme provides operation in a wider spectral range, $\delta \gg \kappa$, if compared with the SCISSOR configuration.

On demand retrieval in CRC scheme can be realized by adiabatically fast equalizing the cavity frequencies after complete absorption of an input light pulse but before its irradiation in an echo pulse at $t \cong 2\pi/\Delta$. The control of cavity frequencies can be implemented via existing methods described in these works [139, 148, 149] providing sufficiently fast switching of the microresonator with frequencies up to hundreds of GHz. The equalized cavity frequencies will lead to freezing of relative phases of CRC modes and to complete stop of the input light pulse in the CRC arrays. The light retrieval will be possible only after recovering the initial cavity frequencies at the times being multiples of $2\pi/\Delta$. Although the maximum storage time in this case is limited by the intrinsic cavity mode Q-factor and by additional

losses caused by the non-ideal switching, this technique opens a direct way for the fast and on demand retrieval of the stored light pulses.

Longer storage in CRC arrays can be implemented by placing resonant atoms in the ring cavity volume. Herein, one can reversibly transfer the cavity mode excitation to the long-lived atomic/spin coherence (for example on the hyperfine sublevels of an NV-center [150, 151, 152, 153, 154]) by applying an additional control laser field and forming cavity enhanced Λ -transition. In particular, single atom with a suitable Λ scheme should be placed in each ring cavity. It demands control of single atoms in 61 individual cavities for the storage of a single photon field on long-lived atomic transition. Remarkably, the non-uniform distribution of coupling constants κ allows to achieve efficient delay with only four cavities [155] and simplifies the scaling problem significantly. Meanwhile, the implementation of the slow light dispersion by incorporating Erbium ions into silica-fused WGM resonator showed the possibility to extend the cavity quality factor to the value of 10^{11} [156] at room temperature. The use of such resonator seems promising but may require additional analysis of the noises created by the presence of Erbium ions.

All discussed observations indicate promising opportunities of the CRC scheme for practical implementation of the frequency comb based quantum repeater. The detailed studies of long-lived CRC based quantum memory schemes will be a subject of further research. The described properties of all-optical photon echo on the chirp ring cavity array coupled with nanofibers demonstrate a promising credit to the room temperature time delay line and optical quantum memory suitable for application in integrated optics.

Chapter 4

White cavity

4.1 Introduction

Quantum information encoded in photons has to be reversibly converted into a matter excitation with a lifetime long enough for a given task. Nowadays there are a number of practical implementations, which include the use of cavities [157], neutral atoms at low [92] or high temperatures [97], quantum dots [158], vacancy centers and phonons in diamond [159, 160], and solids doped with rare ions [161]. Among them the use of a single quantum emitter or ensemble of atoms situated in a strongly coupled cavity [162, 163, 164] is considered promising for use in quantum processing [165, 166, 167]. However, such a memory allows an efficient storage only for flying qubits with special temporal modes, which, in particular, require high-precision match of the signal and control light pulses [49]. Moreover, the finite coupling constant of cavity-atom interaction limits the quantum storage of broadband light fields.

In contrast to single atoms in a high-quality resonator that can only store quantum states of single photon fields, the multi-atomic coherent ensembles provide universal and robust media for storage of arbitrary quantum fields [128, 67, 168, 129, 169]. In addition, atomic ensembles can be used both in free space [13] and in resonators [49]. Both of these

approaches have their advantages and drawbacks and therefore they are under investigations for improvements [67].

The quantum memory protocols require a considerable enhancement of the coherent interaction between resonant photons and atoms, for example, by increasing the number of atoms in the ensemble. This implies using longer cells for hot gases or denser traps for cold gases, such as 2D magneto-optical traps [170] or special sub-wavelength arrangement of atoms [171]. For solid-state media such as rare-earth ions doped crystals increasing optical depth is more challenging. Detailed experimental studies show that absorption coefficient in birefringent materials generally varies with length [172]. This means that absorption will not increase linearly by increasing the crystal length which could in principle limit the maximal optical depth. In addition, bulk crystals are inconvenient for integration in the compact optical systems. Therefore, atomic ensembles placed in resonators are considered as a promising practical platform for quantum storage, but requiring further research and the use of new technological solutions.

The first work [49] devoted to the study of the amplification of the interaction of light with atomic ensembles in an optical resonator showed an asymptotic tendency of quantum efficiency to unity with an increasing collective cooperativity parameter, that is, the maximum possible increase in the collective coupling constant between the cavity mode and atoms. Further improvement came with so-called impedance-matched (IM) configuration [173, 131]. Where an optimal coupling constant between an atomic ensemble and resonant cavity mode for realization of unit quantum efficiency was demonstrated [174, 74, 75, 175].

The combination of this approach with the off-resonant Raman memory [143] allows to efficiently store light on a long-lived ground state hyperfine coherence of some rare-earth ions without application of noisy control π pulses. Here, the reflected wave is suppressed by matching the single-sided cavity Q-factor with an effective optical depth of the media. Simultaneously with this, an incoming wave is fully converted into the ground state hyperfine excitation. As a result, time-reversible absorptive QM under IM condition is capable of

complete absorption and retrieval of incoming light pulses at finite atomic optical depth.

For samples with low optical depth the IM scheme of quantum storage demands a high quality factor. However, an increase of the quality factor leads to proportional narrowing of the cavity linewidth and the QM bandwidth [174]. Together with weak oscillator strength of the ions it makes impossible to store short signal pulses. It was found [173, 176] that the additional IM conditions can provide efficient, $> 90\%$, quantum storage in wider spectral range, but still limited by a spectral width of the cavity mode.

Here we propose to extend the bandwidth of impedance matched QM by exploiting the white cavity effect [177]. The general idea can be expressed as extending impedance matching over the broader spectral bandwidth by introducing the dispersion interaction of atoms with additional control field providing zero spectral dispersion for the signal field. The dispersion interaction compensates the round-trip phase shift for different spectral components of the incoming signal field to keep them under IM conditions.

The chapter is structured as follows. First we present a classical model for describing white cavity impedance matching. Next we present the quantum treatment for storage of the incoming field in Raman echo QM operating in IM white cavity regime and show the extension of the memory's bandwidth. At the end we analyze the noise induced by the imaginary part of the abnormal dispersion and present a regime of a noise free operation. Finally we discuss possible experimental implementations.

4.2 Classical approach

Let us consider the simplest cavity consisting of two mirrors with amplitude reflection coefficients r_1, r_2 . The cavity is driven by an incident plane wave with wave-vector $k = \frac{2\pi\nu}{c}$, where c is the speed of light and ν is the central frequency. If the cavity is filled with a linear medium having a complex refractive index $\underline{n}(\nu) = \sqrt{1 + \chi(\nu)}$, where electric susceptibility of the media $\chi(\nu) = \chi'(\nu) + i\chi''(\nu)$ consist from real $\chi'(\nu)$ and imaginary $\chi''(\nu)$ parts. We

can obtain equations for the reflected field amplitude and intensity from the cavity [178]:

$$E_{\text{ref}} = E_{\text{in}} \frac{r_2 e^{i2kl\sqrt{1+\chi(\nu)}} - r_1}{1 - r_1 r_2 e^{i2kl\sqrt{1+\chi(\nu)}}}, \quad (4.1)$$

$$I_{\text{ref}} = I_{\text{in}} \frac{(r_1 - r_2 e^{-2kl\cdot\alpha(\nu)})^2 + 4r_1 r_2 e^{-2kl\cdot\alpha(\nu)} \sin^2\left(\frac{\pi\nu n(\nu)}{\text{FSR}}\right)}{(1 - r_1 r_2 e^{-2kl\cdot\alpha(\nu)})^2 + 4r_1 r_2 e^{-2kl\cdot\alpha(\nu)} \sin^2\left(\frac{\pi\nu n(\nu)}{\text{FSR}}\right)}, \quad (4.2)$$

where l is a length of the cavity and $\text{FSR} = c/(2l)$ is its free spectral range (FSR). The losses due to the media are expressed as extinction coefficient $\alpha(\nu)$, while the phase retardation is expressed as refractive index $n(\nu)$:

$$\alpha(\nu) = \sqrt{\left(\sqrt{(1 + \chi'(\nu))^2 + (\chi''(\nu))^2} - 1 - \chi'(\nu)\right) / 2}, \quad (4.3)$$

$$n(\nu) = \sqrt{\left(\sqrt{(1 + \chi'(\nu))^2 + (\chi''(\nu))^2} + 1 + \chi'(\nu)\right) / 2}. \quad (4.4)$$

In the absence of the medium ($\chi', \chi'' = 0$) the resonance occurs for a frequency equal to the multiple of FSRs: $\nu = m \cdot \text{FSR}$, where $m \in \mathbb{N}$. In turn, the impedance matching occurs ($I_{\text{ref}} = 0$) at resonance, when the reflection coefficient of the input mirror equals to the round trip losses: $r_1 = r_2$, that corresponds to the full transmission of the wave from the input to the output mirror. If the medium is present, the impedance matching condition is modified to be

$$r_1 = r_2 e^{-2kl\cdot\alpha(\nu)}. \quad (4.5)$$

One can think, that if the media is able to provide dispersion profile with inverse frequency dependence $n(\nu) \sim \frac{1}{\nu}$, the broadbandness is realized since the argument of the sinus in Equation (4.2) is constant. Unfortunately, this dispersion is going to be accompanied by logarithmically increasing absorption $\alpha(\nu) \sim \log \nu$ because of the Kramers–Kronig relations. This additional absorption would ruin the impedance matching at larger frequency range. Therefore, the realization of large broadbandness covering several FSRs seems not feasible.

However we still can try to consider a single resonance and expand its bandwidth by finding suitable compensating dispersion.

For further analysis we consider a single resonance occurring at frequency ν_0 and expand the small frequency deviation $\delta\nu$ with respect to ν_0 . In this case the Taylor expansion gives next result:

$$\sin^2 \left(\frac{\pi\nu n(\nu)}{\text{FSR}} \right) \approx \left(\frac{d}{d\nu} \sin \left(\frac{\pi\nu n(\nu)}{\text{FSR}} \right) \Big|_{\nu_0} \delta\nu + \mathcal{O}(\delta\nu^2) \right)^2. \quad (4.6)$$

The first order broadbandness is realized when the linear term in the expansion is suppressed

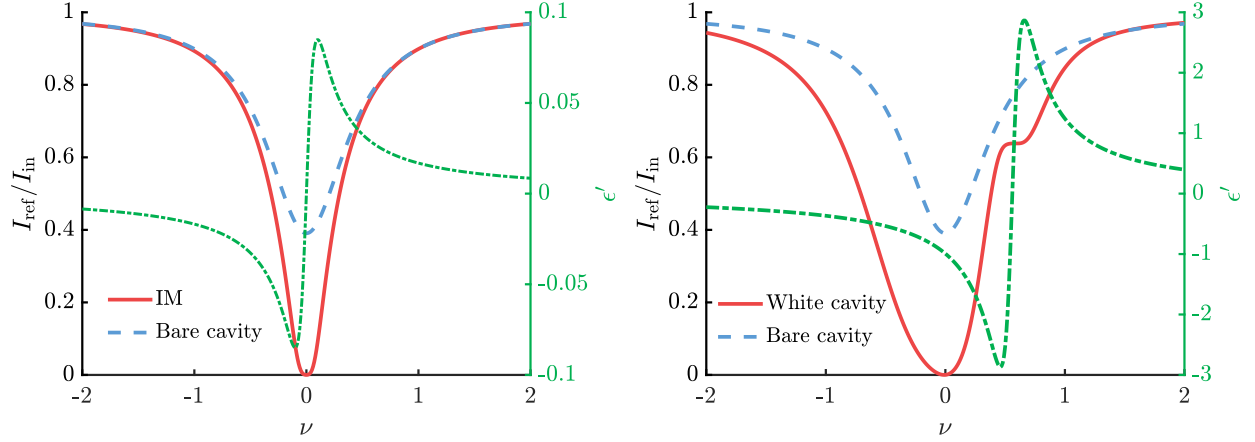
$$\left(n(\nu) + \nu \frac{dn(\nu)}{d\nu} \right) \Big|_{\nu_0} = 0. \quad (4.7)$$

Therefore the realization of the first order broadness requires a slow negative slope of the dispersion. In principle, the condition is not that strict, since slow negative slope dispersion is not exotic material and it would be accompanied by small flat absorption, that should not ruin the impedance matching. Similarly, the second order in the Taylor expansion can be eliminated :

$$\left(2 \frac{dn(\nu)}{d\nu} + \nu \frac{d^2n(\nu)}{d^2\nu} \right) \Big|_{\nu_0} = 0 \quad (4.8)$$

Since our goal is to extend the bandwidth for high efficient quantum memory, we may need two types of medium. The first is used to absorb the incoming light and convert it into long-lived atomic coherence. In turn, the second medium guarantees the desired dispersion necessary for the broadbandness. Thus it is important to make sure that the actual storage is realized on the proper medium. This problem is studied in the Section 4.3 where quantum mechanical treatment is used to assess the problem.

If we assume, that the cavity is single-sided $r_2 = 1$, the conditions (4.7) and (4.5) put restrictions for superposition of storage and compensation medias $\chi(\nu) = \chi_s(\nu) + \chi_c(\nu)$,



(a) Impedance matching, $A=0.017$, $\nu_0=0$

(b) White cavity, $A=0.574$, $\nu_0=0.56$

Figure (4.1) Parameters used in calculations $\text{FSR}=20$, $r_1=0.8$, $r_2=0.95$. $\epsilon' = \frac{A(\nu-\nu_0)}{\gamma^2+(\nu-\nu_0)^2}$

where

$$r_1 = \exp \left(-2kl \sqrt{\left(\sqrt{(1 + \chi'(\nu))^2 + (\chi''(\nu))^2} - 1 - \chi'(\nu) \right) / 2} \right), \quad (4.9)$$

$$\frac{(1 + \chi'(\nu))^2 + (\chi''(\nu))^2 + \frac{\nu_0}{2} (\dot{\chi}'(\nu)(1 + \chi'(\nu)) + \dot{\chi}''(\nu) \cdot \chi''(\nu))}{\sqrt{(1 + \chi'(\nu))^2 + (\chi''(\nu))^2}} + \left(1 + \chi'(\nu) + \frac{\nu_0}{2} \dot{\chi}'(\nu) \right) = 0, \quad (4.10)$$

where we evaluate the spectral properties of different susceptibilities and their performance for extending the impedance matching. For this purpose we introduce simple bandwidth benchmark as 90% absorption band, instead of conventional 50%.

In order to see how the cavity field is modified we consider the medium with Lorentzian profile. In turn the media consists from non-interacting two-level atoms with linear density ρ (numbers of atoms per unit length), resonant transition frequency ν_0 , natural linewidth γ , and transition dipole moment d . The susceptibility of the medium is [15]

$$\chi(\nu) = i \frac{\rho \nu d^2}{\hbar c \epsilon_0} \frac{1}{\gamma - i \cdot (\nu - \nu_0)}, \quad (4.11)$$

where \hbar is the Plank constant, ϵ_0 is the vacuum permittivity and we have assumed the

intensity of electromagnetic wave to be much lower than medium's saturation intensity. As shown in Figure 4.1a, the absorber consisting from two-level atoms achieves a complete suppression of the reflection. The additional Lorentzian profile in Figure 4.1b with negative dispersion increases the effective 90% bandwidth by a factor of ~ 5 .

4.3 Quantum mechanical approach: Model

Next we consider full quantum treatment of the memory protocol in the presence of the compensation medium. We assume that an atomic ensemble is placed inside a one-sided high-quality factor single-mode cavity as it is depicted in Figure 4.2. We use the double- Λ scheme of the atomic transition where the ground atomic levels $|1\rangle$ and $|4\rangle$ are initially populated, while other ground levels $|2\rangle$ and $|5\rangle$ are depopulated. Signal field \hat{a}_{in} is launched into the cavity in the presence of two control laser fields propagating at some angles to the cavity axis. One control field is characterized by the wave vector \vec{k}_L , carrier frequency ω_L and Rabi frequency Ω_L . This field couples atomic states $|2\rangle$ and $|3\rangle$ and provides a usual off-resonant Raman interaction with the cavity mode field \hat{a}_s on the Λ transition $|1\rangle \rightarrow |3\rangle \rightarrow |2\rangle$ through optically excited state $|3\rangle$ with spectral detuning on optical transition Δ_L . Second control field with wave vector \vec{k}_n and carrier frequency ω_n couples atomic states $|4\rangle$ and $|6\rangle$ with Rabi frequency Ω_n and provides an off-resonant interaction of the cavity mode field with atomic transition $|4\rangle \leftrightarrow |5\rangle$ through the optical state $|6\rangle$ with detuning Δ_n .

We note that in contrast with the first Λ scheme, the signal and second control laser fields do not result in a resonant transition between atomic states $|4\rangle$ and $|5\rangle$. Large two-photon detuning δ governs the dispersion type of interaction on transition $|4\rangle \rightarrow |6\rangle \rightarrow |5\rangle$ between the signal light and atoms (see Figure 4.2). Moreover, in contrast with usual off-resonant interaction on the atomic transition $|1\rangle \rightarrow |3\rangle \rightarrow |2\rangle$, the signal light field interacts on the transition $|4\rangle \rightarrow |6\rangle \rightarrow |5\rangle$ with an inverted atomic population leading to the inverted spectral dispersion. By controlling the parameters of inverted dispersion

we find the condition of impedance matched QM in a broad spectral range due to strong compensation of the negative spectral effects in light-atom interaction in this spectral range.

As usual, we consider the light-atom interaction in the limit of a weak signal field, when it is sufficient to take into account a linear atomic response to the input signal field. By using an input-output formalism [119], we get the following system of equations for slowly varying operators of the cavity mode \hat{a}_s and atomic coherences for j th atom $\hat{P}_{pq}^j = |p\rangle_{jj} \langle q|$ ($p, q=1, \dots, 6$):

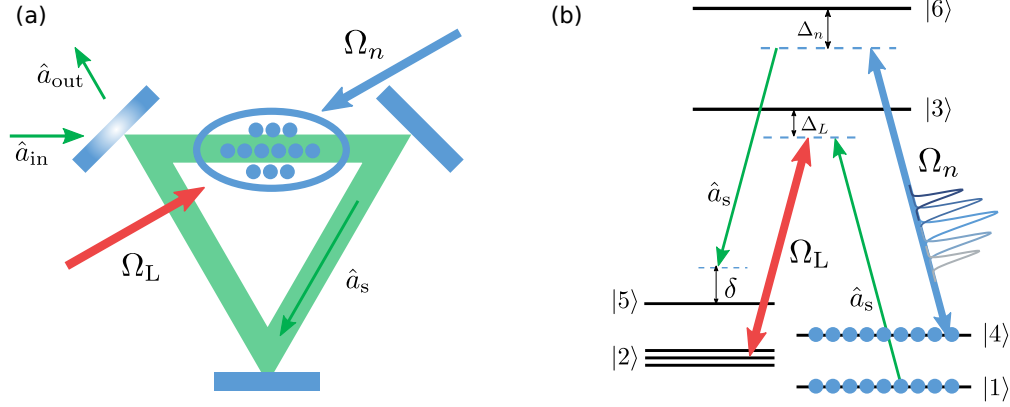


Figure (4.2) (a) The atomic media is coupled to a running-wave cavity. (b) The atomic levels and quantum transitions: strong control laser field Ω_L provides an absorption for optical cavity field \hat{a} via two-photon Raman transition $|1\rangle \rightarrow |3\rangle \rightarrow |2\rangle$; the additional control field Ω_n through the Raman scattering on second lambda scheme $|4\rangle \rightarrow |6\rangle \rightarrow |5\rangle$ realizes dispersion compensation mechanism for extending impedance matched cavity linewidth.

$$\frac{d}{dt}\hat{a}_s = -\left(\frac{\kappa}{2} + i\omega_s\right)\hat{a}_s - i\sum_{j=1}^N \left(g_1^j\hat{P}_{13}^j + g_2^j\hat{P}_{56}^j\right)e^{-i\vec{k}_s\vec{r}_j} + \sqrt{\kappa}\hat{a}_{in}, \quad (4.12)$$

$$\frac{d}{dt}\hat{P}_{13}^j = -(\gamma_{13} + i\omega_{31}^j)\hat{P}_{13}^j - ig_1^{j*}e^{i\vec{k}_s\vec{r}_j}\hat{a}_s\langle\hat{P}_{11}^j\rangle - i\Omega_L e^{-i(\omega_L t - \vec{k}_L\vec{r}_j)}\hat{P}_{12}^j, \quad (4.13)$$

$$\frac{d}{dt}\hat{P}_{12}^j = -(\gamma_{12} + i\omega_{21}^j)\hat{P}_{12}^j - i\Omega_L^* e^{i(\omega_L t - \vec{k}_L\vec{r}_j)}\hat{P}_{13}^j, \quad (4.14)$$

where ω_s and \vec{k}_s are a resonant frequency and a wave vector of the cavity mode, g_1^j and g_2^j are the coupling constants for the cavity mode interacting with atomic transitions $|1\rangle \leftrightarrow |3\rangle$ and $|5\rangle \leftrightarrow |6\rangle$, γ_{nm} are the decay constant on the atomic transition $|n\rangle \leftrightarrow |m\rangle$, κ is

the coupling constant of this mode with the external field modes. In accordance with the photon echo QM protocol [143], it was also assumed a presence of controllable inhomogeneous broadening on the atomic transition $|1\rangle \rightarrow |2\rangle$.

The atomic coherence excited on the transition $|4\rangle \rightarrow |6\rangle \rightarrow |5\rangle$ is governed by the following equations for the atomic coherences:

$$\frac{d}{dt}\hat{P}_{46}^j = -(\gamma_{46} + i\omega_{64})\hat{P}_{46}^j - i\sum_{n=1}^{n_c}\Omega_n e^{-i(\omega_n t - \vec{k}_n \vec{r}_j)} \langle \hat{P}_{44}^j \rangle, \quad (4.15)$$

$$\frac{d}{dt}\hat{P}_{56}^j = -(\gamma_{56} + i\omega_{65})\hat{P}_{56}^j - i\hat{P}_{54}^j \sum_{n=1}^{n_c}\Omega_n e^{-i(\omega_n t - \vec{k}_n \vec{r}_j)}, \quad (4.16)$$

$$\frac{d}{dt}\hat{P}_{45}^j = -(\gamma_{45} + i\omega_{54})\hat{P}_{45}^j + i\hat{P}_{65}^j \sum_{n=1}^{n_c}\Omega_n e^{-i(\omega_n t - \vec{k}_n \vec{r}_j)} - ig_2^j e^{i(\omega_s t - \vec{k}_s \vec{r}_j)} \hat{a}_s^\dagger \hat{P}_{46}^j, \quad (4.17)$$

where the sum is taken over a number of additional control laser fields n_c with Rabi frequencies Ω_n , carrier frequencies ω_n , and wavevectors \vec{k}_n . We simplify Eqs. 4.15–4.17 by taking into account off-resonant interaction of light fields with atoms and assuming a sufficiently large spectral detunings of additional control laser fields $|\omega_{64} - \omega_n| \gg \delta\omega_f$.

Eqs. 4.12–4.14 are common for the off-resonant Raman QM [13]. By transferring to slowly varying fields $\{\hat{a}_s; \hat{a}_{in}\} = e^{i\omega_s t} \{\hat{a}_s; \hat{a}_{in}\}$ and atomic coherences $\hat{P}_{12}^j = \hat{\tilde{P}}_{12}^j e^{-i(\omega_s - \omega_L)t}$, $\hat{P}_{13}^j = \hat{\tilde{P}}_{13}^j e^{-i(\omega_s t - \vec{k}_s \vec{r}_j)}$ and after performing the Fourier transformation:

$$\{\hat{\tilde{P}}_{kl}^j(t), \hat{\tilde{a}}_s(t), \hat{\tilde{a}}_{in}(t)\} = \frac{1}{\sqrt{2\pi}} \int d\omega e^{-i\omega t} \{\hat{\tilde{P}}_{kl}^j(\omega), \hat{\tilde{a}}_s(\omega), \hat{\tilde{a}}_{in}(\omega)\}, \quad (4.18)$$

we deduce from Eqs. 4.13–4.17:

$$\hat{\tilde{a}}_s(\omega) = \frac{\sqrt{\kappa}}{\kappa/2 + \beta_1(\omega) - i\beta_2(\omega) - i\omega} \hat{\tilde{a}}_{in}(\omega), \quad (4.19)$$

$$\beta_1(\omega) = \langle \hat{P}_{11} \rangle \sum_{j=1}^N \frac{|g_1^j|^2}{\gamma_{13} + i(\Delta_L - \omega) - i\frac{|\Omega_L|^2}{(\delta_{21}^j - \omega - i\gamma_{12})}}, \quad (4.20)$$

$$\beta_2(\omega) = \langle \hat{P}_{44} \rangle \sum_{j=1}^N |g_2^j|^2 \frac{\sum_{n=1}^{n_c} \frac{1}{(\omega - \delta_n + i\gamma_{45})} \frac{|\Omega_n|^2}{(\Delta_n + i\gamma_{46})}}{(\Delta_1 + \delta_1 - \omega - i\gamma_{56}) + \sum_{n=1}^{n_c} \frac{|\Omega_n|^2}{(\omega - \delta_n + i\gamma_{45})}}, \quad (4.21)$$

where δ_{21}^j is individual detuning of atom due to inhomogeneous broadening of level $|2\rangle$. We note that $\beta_1(\omega)$ characterizes spectral properties of the absorption and dispersion in the off-resonant interaction of signal light with atoms [143]. While term $\beta_2(\omega)$ is responsible only for the additional spectral dispersion effects caused by the presence of additional control laser fields Ω_n . Now we can find the output field by using input-output relation $\hat{a}_{\text{out}} = \sqrt{\kappa}\hat{a}_s - \hat{a}_{\text{in}}$ [119] and Eq. 4.19 we have $\hat{a}_{\text{out}}(\omega) = R(\omega)\hat{a}_{\text{in}}(\omega)$, where

$$R(\omega) = \frac{\kappa/2 - \beta_1(\omega) + i\beta_2(\omega) + i\omega}{\kappa/2 + \beta_1(\omega) - i\beta_2(\omega) - i\omega} \quad (4.22)$$

is a spectral reflection coefficient of the input signal field, which characterizes the properties of the studied QM scheme. Input signal light within spectral range with reflection coefficient $R(\omega) = 0$ is efficiently mapped on the spin coherence. The process is accompanied by a strong rephasing of the spin atomic coherence created on the transition $|1\rangle \leftrightarrow |2\rangle$ by inhomogeneous broadening. In accordance with cavity assisted photon echo QM scheme, the retrieval of the input signal is realized by active rephasing of the spin coherence in a presence of control laser fields [143]. In the studied case, we have to apply two additional control laser fields Ω_L and Ω_n . An efficient echo emission is guaranteed by the temporal reverse scenario of the light-atom interaction which can be even generalized for irradiation of echo pulse with another temporal duration and carrier frequency [179]. Below we analyze the particular cases of broadband off-resonant quantum storage with the application of dispersion compensation laser field Ω_n .

4.4 Controlling the field storage by one and two additional off-resonant laser fields

1) One control field ($n = n_c = 1$). By assuming that all the decay constants on the optical and spin transitions are close to each other $\gamma_{46} = \gamma_{56} = \Gamma$ and $\gamma_{45} = \gamma_{12} = \gamma$, we can

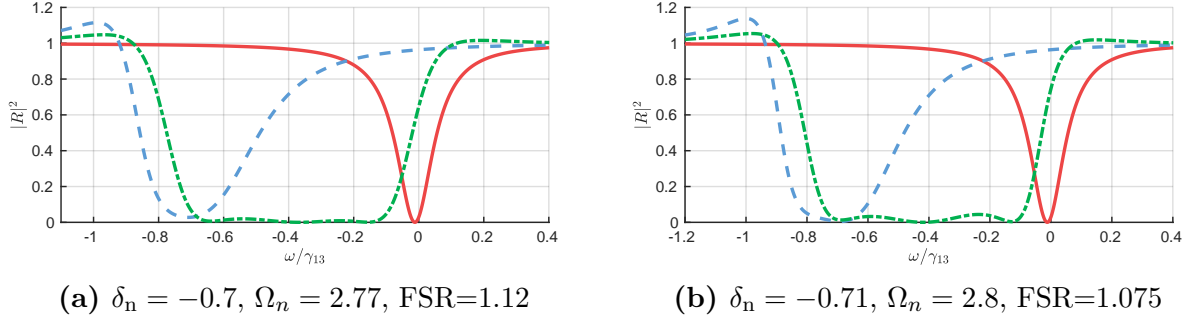


Figure (4.3) Numerical simulation of the reflected field from one-sided cavity, where the solid red line corresponds to usual IM condition without additional dispersion compensation fields $\Omega_n = 0$, $\Omega_L = \sqrt{\frac{\Delta_s^2 \Delta_{\text{in}}}{2C\gamma_{13}}} \cong 8.47$; the blue dashed line reflects the situation of applied dispersion compensation field having a single central frequency and Rabi frequency $\Omega_n = 2.2$; the green dotted line corresponds to the case dispersion compensation fields with two sideband $\Omega_1 = \Omega_2 \approx 0.4$ ($n_c = 1$) detuned by one FSR away. All parameters used in calculations are given in units of γ_{13} and are $\delta_{21}^j = 2.84$, $\Delta_s = 9.2$, $\Delta_n = 1.44$, $\gamma_{12} = 0$, $\gamma_{45} = 0.0074$, $\gamma_{46} = 0.005$, $\gamma_{56} = 0.555$, $\langle P_{11} \rangle = \langle P_{44} \rangle = 1$, $\kappa = 0.0705$; cooperativity parameter $C = N \frac{|g_1|^2}{\kappa \gamma_{13}} \approx 16.7$.¹

simplify $\beta_2(\omega)$ as follows

$$\beta_2(\omega) = \frac{\langle \hat{P}_{44} \rangle}{(\Delta_1 + i\Gamma)} \frac{|\Omega_1|^2 \sum_{j=1}^N |g_2^j|^2}{[(\delta_1 + \Delta_1 - \omega - i\Gamma)(\omega - \delta_1 + i\gamma) + |\Omega_1|^2]}. \quad (4.23)$$

In Figure 4.3, we present a numerical simulation of reflection coefficient $|R(\omega)|^2$ for the usual case of impedance matching storage ($n_c = 0$, red, solid line) and for the quantum storage in a presence of a single control laser field ($n_c = 1, \Omega_1 \neq 0$, blue dashed line). Strong suppression of the field reflection in broad spectral range means broadband IM and efficient absorption of the input light field. It is seen that applying just a single dispersion compensation laser field makes the impedance matched spectral width 8 times wider on the level of spectral quantum efficiency 99%.

2) $n_c = 3$.

We consider three additional dispersion compensation fields because of the it is easy to

¹The figure and the caption were created by A. Tashchilina.

²The table and the caption were created by A. Tashchilina

γ_{12}	γ_{13}	γ_{45}	γ_{46}	γ_{56}	κ	Ω_L	Ω_n	Δ_L, Δ_s	δ_n	δ_{21}^j	Δ_n
0	1	0.0074	0.005	0.555	0.0705	8.4733	2.8	9.2	-0.7	2.84	1.44

Table (4.1) Parameters are normalized by γ_{13} and used for calculation to produce Figure 4.3. ²

get them via phase modulation of single dispersion compensation field. The case of three additional dispersion compensation fields $(\Omega_1, \Omega_2, \Omega_3)$ depicted by a green line in Figure 4.3 provides 2 times larger spectral width of impedance matching in comparison with the previous case $n_c = 1$. And it is - 16 times broader than it is for usual spectral impedance matching QM. We note that the control fields $\Omega_{1,2,3}$ lead to additional optical Stark-shifts in off-resonant Raman transition, as it is seen for the central part of small reflection coefficient in the Figure 4.3. Moreover, it is also seen that large decay constant γ_{23} on the atomic transition $|2\rangle \leftrightarrow |3\rangle$ could lead to the amplification of the signal field (see a peak near $\omega/\gamma_{13} \approx -1.0$). The main contribution to the amplification is imaginary part of Raman gain, which bandwidth start to coincides with shifted broad impedance matched resonance. Fortunately in the case of modulated pump (green dotted line), the Stark shift plays positive role and keeps the resonance away from the noise bandwidth. In addition it is possible to suppress the amplification by using a sufficiently large spectral detunings $\Delta_{1,2,3} \gg \gamma_{23}$ where there is only a dispersive atomic response to the input signal field due to the strong detuning of the resonant interaction.

Strong suppression of the light reflection for the frequency range: $-0.75 < \omega/\gamma < -0.55$ (where $|R(\omega)|^2 < 0.01$) means an efficient transfer of the signal field $\hat{a}_s(\omega)$ in the atomic coherence \hat{P}_{12}^j . Herein the absence of the signal field in the cavity leads to the absence of atomic coherence on the adjusted atomic transition $|4\rangle \leftrightarrow |6\rangle$. Finally we see about 12 and 20 times increase of the bandwidth at 90% and 95% absorbing levels respectively.

4.5 Noises in the scheme

There are several possible noise sources in the proposed scheme. It includes four-wave mixing process induced by the cavity signal field, the control field acting on transition $|1\rangle \rightarrow |3\rangle$ and $|2\rangle \rightarrow |3\rangle$, and an auxiliary idler field. When pump is not collinear with the cavity mode such process can be dumped by the absence of geometrical phase-matching. For the collinear configuration the proper choice of the cavity frequency still can dump the four-wave mixing since the cavity may not provide necessary state for the idler field to fulfill energy conversion law. The proper density of the cavity state together with geometry can suppress such process [180].

The presence of the additional dispersion is accompanied by the corresponding gain or loss according to Kramers–Kronig relations. The gain is responsible for the amplification and noise due to accompanying spontaneous emission. In contrast to four wave mixing, this process is not coherent and cannot be suppressed by choice of geometry. Thus it is necessary to take into account this effect.

For modelling the spontaneous emission we include the Langevin noise term corresponding to spontaneous emission into the Λ system:

$$\frac{d}{dt}\hat{P}_{46}^j = -(\gamma_{46} + i(\omega_{64} - \omega_n))\hat{P}_{46}^j - i \sum_{n=1}^{n_c} \Omega_n e^{i\vec{k}_n \vec{r}_j} \langle \hat{P}_{44}^j \rangle + \hat{F}_{46}^j, \quad (4.24)$$

$$\frac{d}{dt}\hat{P}_{56}^j = -(\gamma_{56} + i(\omega_{65} - \omega_s))\hat{P}_{56}^j - i\hat{P}_{54}^j \sum_{n=1}^{n_c} \Omega_n e^{i\vec{k}_n \vec{r}_j} + \hat{F}_{56}^j, \quad (4.25)$$

$$\frac{d}{dt}\hat{P}_{45}^j = -(\gamma_{45} + i(\omega_{54} - \omega_n + \omega_s))\hat{P}_{45}^j + i\hat{P}_{65}^j \sum_{n=1}^{n_c} \Omega_n e^{i\vec{k}_n \vec{r}_j} - ig_2^j e^{-i\vec{k}_s \vec{r}_j} \hat{a}_s^\dagger \hat{P}_{46}^j + \hat{F}_{45}^j, \quad (4.26)$$

where $\hat{F}_{mn}^j(t)$ represents generalized delta-correlated Langevin noise terms [15] with correlators of the form $\langle \hat{F}_{mn}^j(t) \hat{F}_{nm}^j(t') \rangle = D_{mm}^j(t) \delta(t - t')$ and $D_{mm}^j(t)$ are generalized diffusion coefficients [86, 181].

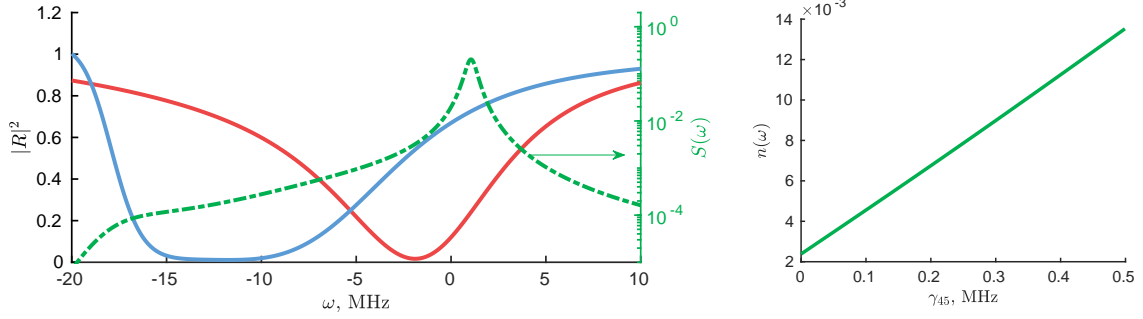


Figure (4.4) (a) The noise spectrum of spontaneously emitted photons (green dot-dashed) together with the broadened (blue dashed curve) and unbroadened (red solid curve) impedance matched absorption profile.

The output field is found similarly as in Section 4.3 with an additional noise term:

$$\hat{a}_{\text{out}}(\omega) = R(\omega)\hat{a}_{\text{in}}(\omega) + \frac{\kappa}{\kappa/2 + \beta_1(\omega) - i\beta_2(\omega) - i\omega} \delta\hat{a}_{\text{noise}}(\omega), \quad (4.27)$$

where the noise term is the superposition of two

$$\delta\hat{a}_{\text{noise}}(\omega) = i \sum_{j=1}^N g_2^j \left(\frac{\hat{F}_{56}^j e^{-i\vec{k}_s \vec{r}_j}}{\Xi(\omega)} - \frac{i\hat{F}_{54}^j \Omega_1 e^{i(\vec{k}_n - \vec{k}_s) \vec{r}_j}}{\Gamma(\omega)\Xi(\omega)} \right), \quad (4.28)$$

$$\Gamma(\omega) = (\gamma_{45} - i\delta + i\omega), \quad (4.29)$$

$$\Xi(\omega) = \gamma_{56} + i(\omega_{65} - \omega_s) - i\omega + |\Omega_1|^2 / \Gamma(\omega). \quad (4.30)$$

The corresponding output spectrum $\langle \hat{n} \rangle = \langle \hat{a}^\dagger(t'), \hat{a}(t) \rangle = \int d\omega S(\omega) e^{-i\omega(t-t')}$ for a vacuum input:

$$S(\omega) = \left| \frac{\kappa g_2}{\kappa/2 + \beta_1(\omega) - i\beta_2(\omega) - i\omega} \right|^2 \cdot N \left(\frac{\gamma_{56} \langle \hat{P}_{66} \rangle}{|\Xi(\omega)|^2} + \frac{|\Omega_1|^2 (\gamma_{54} \langle \hat{P}_{44} \rangle + (\gamma_{46} + \gamma_{56}) \langle \hat{P}_{66} \rangle)}{|\Gamma(\omega)\Xi(\omega)|^2} \right). \quad (4.31)$$

Our memory has a relatively low noise level of $\sim 10^{-2}$ photons per a bandwidth unit, as can be seen in Figure 4.4a. Such noise levels allow the memory to operate in quantum regime with a high fidelity [82].

γ_{12}	γ_{13}	γ_{45}	γ_{46}	γ_{56}	κ	Ω_L	Ω_n	Δ_L	Δ_n	δ_n	δ_{21}^j
0.1	10	0.001	1	1	6.5	35.4	28.3	58	15	-13	19.4

Table (4.2) Parameters used to find the noise spectrum presented in Figure 4.4. All these parameters are in MHz. Other parameters $\langle \hat{P}_{11} \rangle N g_1^2 = 283 \text{ MHz}^2$, $\langle \hat{P}_{44} \rangle N g_2^2 = 158 \text{ MHz}^2$, $g_1 = g_2 = 100 \text{ Hz}$.

Among all the control parameters the low noise regime is achieved only for high coherence times between levels $|4\rangle$ and $|5\rangle$. The dependence of the noise power on γ_{45} is presented in Figure 4.4b. In turn, there is strict requirement on a specific material, where long coherence time of the ground levels is accompanied by the existence of an additional three-level system. In the next section we consider suitable materials.

4.6 Experimental feasibility

In this section, we discuss suitable materials for the experimental realization of the broadband impedance-matched photon-echo QM. These materials should be able to provide spectrally independent ensembles with addressable Λ schemes. As memory cells built with dielectric crystals doped with rare-earth (RE) ions are solid-state, scalable, and have on-chip realizations, we will limit our consideration to these crystals.

Table (4.3) Potential candidates for implementation of the off-resonant Raman QM. Here Γ_{inh} is an inhomogeneous broadening of an optical transition, T_1 and T_2 are achieved longitudinal and transverse relaxation times of the ground state spin coherence, λ is the central wavelength of the optical transition.

Material	Doping %	Γ_{inh} MHz	T_1 s	T_2 s	λ nm	dipole moment C·m	Ref.
$^{167}\text{Er}^{3+}:\text{Y}_2\text{SiO}_5$	0.005	150	9.2	1.3	1538.903	7×10^{-32}	[182]
$\text{Pr}^{3+}:\text{Y}_2\text{SiO}_5$	0.05	$3 \cdot 10^3$	$\sim 10^2$	60	605.977	3.7×10^{-32}	[183]
$\text{Eu}^{3+}:\text{Y}_2\text{SiO}_5$	0.01	$1.4 \cdot 10^3$	$\sim 10^5$	3600	579.879	1.36×10^{-34}	[184]

We find crystals presented in Table 4.3 to be the best known candidates for an implementation of the off-resonant Raman QM protocol. Their ground hyperfine levels have both extremely long lifetimes, T_1 , and long phase-relaxation times, T_2 , leading to long storage times

of quantum information. In addition, some of them have optical transitions compatible with telecom bands, where the transmission losses are low and numerous optical-communication devices exist.

First, let us consider the non-Kramers RE ions, such as Eu^{+3} and Pr^{+3} in yttrium silicate (Y_2SiO_5). Their states are singlet states and their electron spin is equal to zero. Thus, the strong dephasing mechanism, being phonon-electron interaction, is heavily suppressed at low temperatures. The main remaining dephasing mechanism is governed by the fluctuations of the magnetic field created by fluctuations of environmental nuclear spins. There are two techniques, namely the zero first-order Zeeman shift and/or dynamical decoupling [95], to mitigate the effect of these fluctuations and to achieve a large nuclear spin coherence time (see Table 4.3). This makes these ions good candidates for quantum storage.

Moreover, non-Kramers ions allow engineering of different absorption profiles by spectral hole burning [89, 184]. The hole-burning technique allows isolation of an ensemble of identical ions within the spectral window with a bandwidth determined by the ground state hyperfine splitting [185]. In addition to the creation of the individual ion ensembles for the memory, the application of selective hole burning may create frequency shifted separate ensembles required for dispersion compensation for the proposed scheme. However, operational wavelengths for both of these ions lay in the visible range, which may require quantum wavelength conversion for communication application.

The Er^{3+} ion with telecom compatible $^4\text{I}_{15/2} \rightarrow ^4\text{I}_{13/2}$ transition is a natural choice for a quantum memory for quantum repeaters. However, Er^{+3} being the Kramers ion with non-zero electronic spin exhibits strong phonon relaxation, which limits the lifetime of the ground hyperfine states up to several milliseconds. Meanwhile, it was found that the presence of a large enough magnetic field suppresses resonant phonon relaxation [182]. The coherence time of hyperfine levels of $^{167}\text{Er}^{3+}$ isotope in Y_2SiO_5 was extended to ~ 1.3 s [182]. In this regime, an effective hole burning and ground state spin polarization of $^{167}\text{Er}^{3+}$ are achievable. The inhomogeneous broadening of 180 MHz [186] in turn would allow engineering of independent

memory and dispersion compensation ensembles in $\text{Er}^{3+} : \text{Y}_2\text{SiO}_5$. Overall, this crystal is the promising candidate for realization of the broadband impedance-matched telecom memory.

After choosing an appropriate material, we would like to specify possible cavity designs that could provide the required impedance matching. The easiest solution would be to place an RE doped crystal into an existing Fabry-Perot resonator [74, 175]. This external Fabry-Perot design is characterized by large intra-cavity losses due to scattering at the surfaces of the crystal. The losses are inevitable even for anti-reflective coated crystals, so we do not consider the external Fabry-Perot further.

Two more designs are the monolithic Fabry-Perot, where the crystal surfaces are reflective-coated to create the Fabry-Perot resonator within the crystal [187, 174], and the whispering gallery mode (WGM) resonator [188], where WGM is milled from the RE doped crystal. The losses for both of them are limited by the bulk Y_2SiO_5 losses per round trip and are estimated to be $7 \cdot 10^{-4} \text{cm}^{-1}$ for visible light [187]. These losses are due to material absorption as authors [187] claim, and they dominate over fundamental losses due to Rayleigh and Brillouin scattering [189]. The resulting quality factors of monolithic and WGM resonators are comparable. The experimental simplicity of the monolithic design makes it the preferable choice for the cavity ³.

Finally, we make estimations on feasibility of experimental realization on 9 mm monolithic cavity created from Y_2SiO_5 crystal [187] doped with isotopically purified $^{167}\text{Er}^{+3}$. The inhomogeneous broadening of the sample allows implementation of the memory unit and dispersion sample. The option is to optically burn the sample into two frequency separated ensembles within the inhomogeneous broadening profile. In this case the optical linewidth of transition can be made arbitrary small down to homogenous linewidth ~ 10 kHz [191]. We propose to burn memory ensemble with the optical linewidth of 10 MHz and dispersion compensation with the linewidth of 1 MHz. The compensation medium should contain as much as 55% of number atoms as a memory unit. The reflectivity of the front and back

³We do not consider the recently demonstrated photonic-bandgap cavity [190], since its linewidth is larger than inhomogeneous broadening and does not fit requirements of the proposed scheme.

mirrors 99.2% and 99.95% provides the inverse photon lifetime to be $\kappa/2\pi \sim 6.3$ MHz with a cavity volume $\sim 1\text{mm}^3$. This design provides averaged single photon cavity-atom coupling constant of $g/(2\pi) \sim 100$ Hz, and together with ion density $\sim 2 \cdot 10^{10}\text{mm}^{-1}$ it gives the total number of ions within the cavity mode $2 \cdot 10^{10}$. All other relevant parameters are summarized in the Table 4.2.

Work	λ	Efficiency	Lifetime	Delay-bandwidth product	Storage media
[192]	1342 nm	33%	0.22 s	$\sim 10^5$	^{87}Rb
[93]	1367 nm	7%	0.1 s	$\sim 10^5$	^{87}Rb
[84]	1532 nm	1%	5 ns	40	Er doped fiber
[47]	1536 nm	40%	16 μs	10	Er:YSO
[193]	1536 nm	0.2 %	450 ns	~ 2	Er:YSO
[194]	1566 nm	14%	15 μs	375	Optomechanics
[195]	1539 nm	0.001 %	10 μs	$\sim 10^3$	^{167}Er :YSO

Table (4.4) Recent telecom quantum memory realizations.

The scheme promises the 90% efficiency bandwidth extension from 4 MHz in usual impedance match scheme to 10 MHz in single control field settings with additional noise less than 0.01 per pulse. Taking into account the coherence time of the Erbium hyperfine levels the resulted delay-bandwidth product can reach $\sim 10^7$ in telecom compatible material. The use of phase modulated control field may open the avenue for extending the bandwidth up to 80 MHz. The proposed scheme may surpass the current telecom quantum memories presented in the Table 4.4.

4.7 Conclusion

In this work we propose the white cavity approach for implementation of the off-resonant broadband Raman quantum memory in a high-Q optical resonator. The idea is based on extending the impedance matching for broader frequency range by additional compensating dispersion. While the proposed “impedance matched white cavity” is a general concept, here we study particular absorption and dispersion realization via two independent Λ schemes. One scheme provides reversible Raman two-photon absorption, while the other is responsi-

ble for dispersion compensation associated with Raman gain. We have analyzed a principle scheme of such QM and found that it is possible to increase the quantum storage bandwidth by more than an order of magnitude. We showed that the noise introduced by the compensation dispersion is low enough to operate in a quantum regime.

Extra dispersion associated with additional Raman gain pumps allows further extension of the bandwidth of the impedance matched cavity in exchange of absorption profile uniformity. The feasible solid state materials for experimental realizations are discussed.

Chapter 5

Raman noises in gradient echo memory

5.1 Introduction

The noise in the QM is a fundamental problem, which may stop the memory from being useful in storing arbitrary quantum states of light. Especially the problem of the noise arises for QM based on Λ -atomic ensembles, where a strong classical laser field acts on one transition. Depending on an atomic sample and used polarization the laser field can simultaneously act on both transitions and produce a FWM between pump laser, signal, and idler fields. The effect of FWM was studied in EIT based memories [196, 86] and it was shown that the noise can be minimized for a homogeneous ensemble with a radiation-limited optical linewidth. The noise induced by FWM was also studied in the Λ gradient-echo memory, where it was shown that an off-resonant interaction together with an inhomogeneous broadening may suppress the FWM [197].

In this chapter, we experimentally and theoretically study the Raman-scattering noise in the gradient-echo memory scheme, this noise being similar to the four-wave mixing has several distinct features. While FWM produces coherent amplification of the signal, the

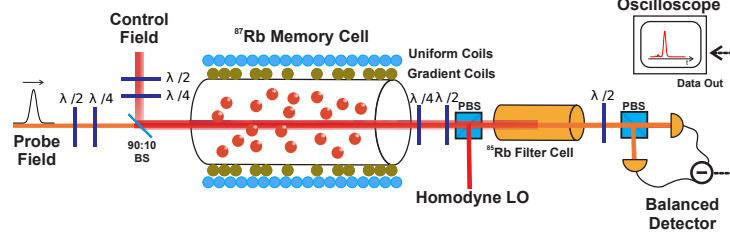


Figure (5.1) Schematic of the experiment used to observe GEM with co-rotating circular polarized fields. BS: beam splitter, PBS: polarizing beam splitter, $\lambda/2$: half-wave plate, $\lambda/4$: quarter-wave plate.

Raman noise is incoherent in its nature and has a unique dependence on the experimental parameters. We experimentally show the properties of the noise and its contribution into the quantum process of the memory. The developed theoretical model of the noise is presented and is in good agreement with experimentally acquired data. The analysis of the model allows to find operational conditions, where the noise can be minimized with a proper choice of the detuning and the level scheme. The experimental data was taken from Connor Kupchak [198].

5.2 Experiment

A schematic diagram of the experiment is shown in Figure 5.1. The memory was realized in a warm vapor of isotopically pure Rubidium 87 contained in cylindrical glass cells with anti-reflection coated windows affixed on both ends. The cell had dimensions of 20 cm length and 25 mm diameter and contained 0.5 Torr of Kr buffer gas, similar to the vapor cell used in References [199, 200]. The cells were situated in a temperature controlled oven at 74°C.

The control field was derived from a continuous-wave Ti:Sapphire laser (Coherent MBR-110) with a linewidth < 100 kHz and was tuned to 795 nm on the D_1 transition of ^{87}Rb . For our experiments the control field was typically blue-detuned by $\Delta_s/2\pi = 1 - 2$ GHz from the $|5S_{1/2}, F = 2\rangle \rightarrow |5P_{1/2}, F' = 2\rangle$ transition. The probe field used for storage was produced by a homemade external-cavity diode laser and was phase-locked near $+2\pi \cdot 6.83$ GHz (^{87}Rb ground state hyperfine splitting) to the control field using a phase-lock loop

(PLL). The locking frequency was adjusted to the two-field resonance condition ($\delta = 0$) of the split magnetic sub-levels using a reference signal sent into the PLL. The two-field interaction of these lasers created a Raman absorption line at the blue-detuning value Δ_s of the $|5S_{1/2}, F = 1\rangle \rightarrow |5P_{1/2}, F' = 2\rangle$ transition. For storage of the probe field, near-Gaussian pulses of temporal width $2\ \mu s$ were generated by use of an acousto-optic modulator (AOM) in conjunction with a variable voltage attenuator.

A uniform magnetic field was applied to break the degeneracy of the Zeeman sublevels such that the Raman absorption line corresponding to a specific three-level system could be utilized for GEM. The absorption line was broadened with a variable-pitch solenoid that ran longitudinally along the length of the cell. The Raman line was typically broadened to a width of 500 kHz to match the spectral width of the probe field pulses (see Figure 5.3 c). Using a home-made switch we were capable of reversing the direction of this gradient in a time of $< 500\text{ ns}$, which was sufficient for typical lifetimes of our ground state coherence time of about $1\ \mu s$.

Based on prior studies [199, 200], the optimal retrieval efficiency in a Λ -GEM system utilized co-rotating circular polarized light fields. This polarization scheme causes a majority of the population to occupy the $|F = 1, m_F = 1\rangle$ ground state. The control and probe fields were overlapped using a 90:10 beamsplitter. After the memory cell, the strong control field was separated from the weak probe by use of an isotopically pure ^{85}Rb vapor cell of 10 cm length with anti-reflection coated windows. For our detuning values the control field was near resonant to the $|5S_{1/2}, F = 2\rangle \rightarrow |5P_{1/2}, F = 2, 3\rangle$ ^{85}Rb transition while the probe field was far off-resonant to any transition. The filter cell was maintained at $115\text{ }^\circ\text{C}$ that provided a control field extinction of 55 dB and a probe field transmission of 85%.

Our setup allowed both heterodyne and homodyne detection modalities. The weak retrieved probe pulse was measured using a half-waveplate-PBS combination with the beams in the output port impinging upon a balanced detector (Thorlabs PDB150A) operated at a 3 MHz bandwidth. The oscillator beams used for both detections were derived from the

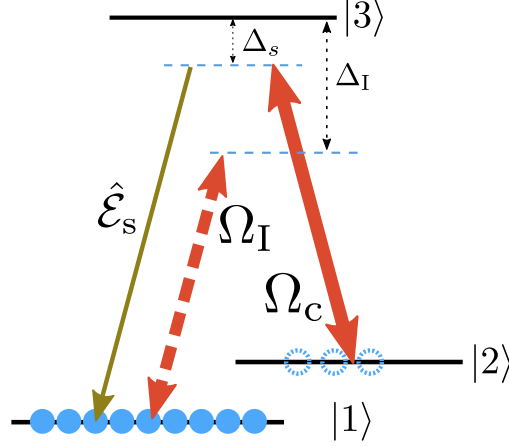


Figure (5.2) Level diagram of the atomic transition. The green (solid) line is the input signal field, the red arrows are the control fields, which act on the $|2\rangle \rightarrow |3\rangle$ transition and spuriously act on the $|1\rangle \rightarrow |3\rangle$ transition with Rabi frequency Ω_I . Here the carrying frequency for the signal field is $\omega_s = \omega_{31} - \Delta_s$ and carrier frequency of the control field is $\omega_c = \omega_{31} - \Delta_s - \omega_{21}$.

same laser generating the probe field. For heterodyne detection, the oscillator beam was modulated at +5.1 MHz away from the probe using an AOM and was mixed with the probe field after the memory process by means of a polarizing beam splitter (PBS). The light fields were mixed before the filter cell to offset the effect of wave vector fluctuations caused by the high temperature of the cell (as shown in Figure 5.1). Typically, visibilities of 97% were achieved between the probe field and the oscillator beams. This detection scheme was used for the classical measurements of the echo retrieval. For homodyne detection, the light field was modulated at the same frequency as the signal field.

5.3 Theoretical model

Here we present the key points for the description of the memory protocol and the noise generation mechanism. The GEM protocol is based on the conversion of signal field $\hat{\mathcal{E}}_s(t, z)$ into slowly varying collective Raman coherence $\hat{R}_{12}^\dagger(t, z')$ by two-photon transition between closely-spaced levels $|1\rangle$ and $|2\rangle$ via the excited level $|3\rangle$. In contrast to EIT-based memories the GEM protocol is less sensitive to the waveform control of the control field, since

the created Raman coherence controllably dephases due to applied linear frequency gradient β along the atomic sample. As the result of the dephasing, the absence of mean coherence suppresses the coherent emission of the atomic excitation back into the signal mode. The reverse of the frequency gradient brings Raman coherence in phase while the applied pump converts it back into the signal field.

In the previous studies the protocol is claimed to be noiseless [199], however we show that the initial non-perfect preparation of the atomic sample leads to unwanted noise in the signal channel. Remarkably the problem occurs for the pumping scheme used extensively in the experiments [200, 199], where the control field was applied “long enough” to depopulate level $|2\rangle$. Unfortunately, the control field, acting on transition $|2\rangle \rightarrow |3\rangle$ (Figure 5.2) with detuning Δ_c and Rabi-frequency Ω_s , simultaneously acts on transition $|1\rangle \rightarrow |3\rangle$ with detuning Δ_I and Rabi-frequency Ω_I . An auxiliary stationary population on level $|2\rangle$ is created and is scattered back into the signal mode. The effect may be enhanced by use of a particular transition and pump polarization in favor of experimental convenience as we show later. The effect is especially strong in some experimentally convenient schemes of pump polarization as we show later.

The properties of generated noise can be analyzed by the set of coupled equations for the signal field and the Raman coherence. Mathematically the signal field is described by a bosonic field operator with commutation relation $[\hat{\mathcal{E}}_s(t, z), \hat{\mathcal{E}}_s^\dagger(t, z')] = \delta(z - z')$. In turn the Raman coherence is presented by a continuous atomic flip operator parameterized by position z . The collective nature of the operator is imprinted in the commutator $[\hat{R}_{12}(t, z), \hat{R}_{12}^\dagger(t, z')] = \frac{\delta(z-z')}{n} (\hat{R}_{11} - \hat{R}_{22})$, where n is a linear atomic density.

Adiabatic elimination of the upper level $|3\rangle$ gives the following Heisenberg-Langevin

equations [201]:

$$\left(\frac{\partial}{\partial t} + \tilde{\gamma}_{12} + i\beta z + i\Delta_{AC}\right) \hat{R}_{12}(t, z) = -i\frac{g_s\Omega_c^*}{(\Delta_s + i\gamma_{13})} \hat{\mathcal{E}}_s(t, z) + \hat{F}_n(t, z) \quad (5.1)$$

$$\left(\frac{\partial}{\partial t} + c\frac{\partial}{\partial z} + ic\delta k\right) \hat{\mathcal{E}}_s(t, z) = -ic\frac{ng_s}{(\Delta_s + i\gamma_{13})} \left(\Omega_c \hat{R}_{12}(t, z) + i\hat{F}_{13}(t, z)e^{-i(k_c - k_s)z}\right) \quad (5.2)$$

where $\delta k = \left(\frac{n|g_s|^2}{(\Delta_s + i\gamma_{13})} + (k_c - k_s)\right)$ is the dispersion relation for the signal field, k_c (k_s) are the wave vector modulo of the control (signal) fields, γ_{ij} are the coherence decay rates, g_s is the signal field coupling constant on the $|1\rangle \rightarrow |3\rangle$ transition, and $\Delta_{AC} = \left(-\frac{|\Omega_I|^2\Delta_I}{\Delta_I^2 + \gamma_{32}^2} + \frac{|\Omega_c|^2\Delta_s}{\Delta_s^2 + \gamma_{31}^2}\right)$ is an AC-Stark shift that is induced by the applied control field acting on both transitions. Decay of coherence is strongly connected to an optical pumping, that leads to a modified decay rate on the $|1\rangle \rightarrow |2\rangle$ transition: $\tilde{\gamma}_{12} = \gamma_{12} + \left(\frac{|\Omega_I|^2\gamma_{32}}{\Delta_I^2 + \gamma_{32}^2} + \frac{|\Omega_c|^2\gamma_{31}}{\Delta_s^2 + \gamma_{31}^2}\right)$. The last terms in equations (5.1) and (5.2) are continuous Langevin noise operators responsible for Raman scattering, and $\hat{F}_n(t, z)$ is a sum of delta-correlated noise operators:

$$\hat{F}_n(t, z) = \frac{\Omega_I}{\Delta_I - i\gamma_{32}} e^{ik_c z} \hat{F}_{32}(t, z) + \frac{\Omega_c^*}{\Delta_s + i\gamma_{13}} e^{-i(k_c - k_s)z} \hat{F}_{13}(t, z) + \hat{F}_{12}(t, z). \quad (5.3)$$

Langevin operators corresponding to the decay of the upper level are included in the decay process of long-lived coherence. The diffusion coefficients can be obtained using generalized Einstein relations [15]:

$$\langle \hat{F}_{12}^\dagger(t, z) \hat{F}_{12}(t', z') \rangle = \delta(t - t') \frac{\delta(z - z')}{n} \left(2\gamma_{12} \langle \hat{R}_{22}(t, z) \rangle + r_{32} \langle \hat{R}_{33}(t, z) \rangle \right) \quad (5.4)$$

$$\langle \hat{F}_{12}^\dagger(t, z) \hat{F}_{13}(t', z') \rangle = \delta(t - t') \frac{\delta(z - z')}{n} (\gamma_{13} - \gamma_{23} + \gamma_{12}) \langle \hat{R}_{23}(t, z) \rangle \quad (5.5)$$

$$\langle \hat{F}_{13}^\dagger(t, z) \hat{F}_{13}(t', z') \rangle = \delta(t - t') \frac{\delta(z - z')}{n} (2\gamma_{13} - r_{23} - r_{13}) \langle \hat{R}_{33}(t, z) \rangle \quad (5.6)$$

$$\langle \hat{F}_{13}^\dagger(t, z) \hat{F}_{12}(t', z') \rangle = \delta(t - t') \frac{\delta(z - z')}{n} (\gamma_{13} - \gamma_{23} + \gamma_{12}) \langle \hat{R}_{32}(t, z) \rangle, \quad (5.7)$$

where r_{ij} are the spontaneous emission rates between levels $|i\rangle$ and $|j\rangle$.

Mean noise operators require averaged populations, which are estimated as a redistribu-

tion of atoms by the control field. Thus we search for the steady-state solution of Heisenberg equations including pump on both transitions $|1\rangle \rightarrow |3\rangle$ and $|2\rangle \rightarrow |3\rangle$, the resulted averaged atomic population in the presence of Doppler broadening is presented in Figure 5.3. While the account of Doppler broadening change the atomic population by few percents, the effect of relatively small inhomogeneous broadening $\Delta_{\text{in}} = \beta L \sim 1$ MHz (L -length of an atomic sample) of level $|2\rangle$ is negligibly small for steady state optical pumping and can be neglected. The power of control field has no significant effect on the distribution of population, since it is mainly dictated by a ratio of the corresponding optical pumping rates. In our case the control field acts on both transitions, and Rabi frequencies are only different by a Clebsh-Gordon coefficient and the pumping ratio stays constant, $\Omega_1/\Omega_c = \sqrt{3}$. While in principle we can include additional excited hyperfine level $|5P_{1/2}, F=1\rangle$, its contribution only slightly changes the decay rate to $|2\rangle$.

The opposite situation happens for the dependence of the population on the detuning: the increase in a blue-shifted detuning of the control field reduces pumping rate for level $|1\rangle$, while increasing the pumping rate for level $|2\rangle$ due to ‘more resonant’ action on transition $|1\rangle \rightarrow |3\rangle$. As the result, the population of level $|2\rangle$ reaches 10 – 20%, when detuning is in a range $\Delta_s/(2\pi) \sim 1 - 1.5$ GHz.

The absorption spectrum presented in Figure 5.3c has several asymmetrical features on the edges of the line. We attribute this to spatial modulation of a pump amplitude along the atomic cell $\Omega(z) = \Omega_c(1 + \epsilon \cos(\frac{2\pi z}{l} + \phi))$ with the modulation depth $\epsilon \approx 0.23$, spatial period $l = 1.35$ m, and phase $\phi \approx 0.64\pi$. The longitudinal inhomogeneous broadening maps this modulation into the absorption spectrum as the different parts of atomic sample provide various Raman absorption strengths. While the spatial modulation can be included into the analysis straightforwardly, it mainly modify the noise spectral density on the edge of the memory operational band. For the Gaussian pulses used for storage the effect of spatial modulation becomes insignificant as its main contribution is outside of the used band. For the sake of simplicity further on we present the model without this effect.

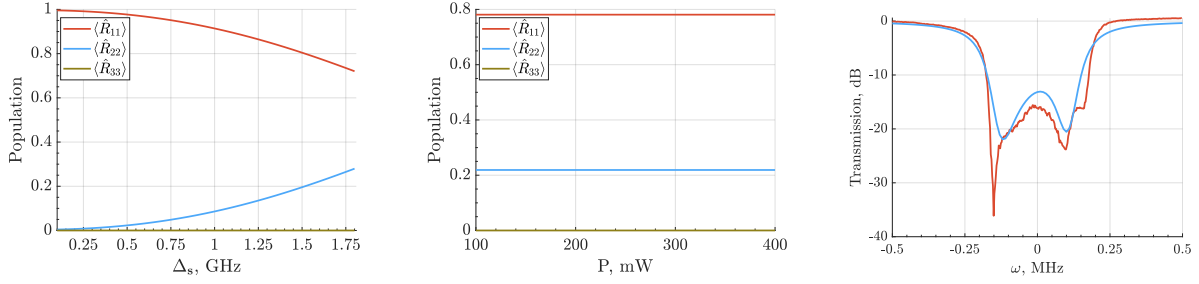


Figure (5.3) (a) Population of level $|1\rangle$ as a function of detuning with power $P=250$ mW. (b) In this figure we show that populations in all three levels are constant for all experimentally available pumping powers. (c) The experimental absorption line (red) and theoretical model (blue).

The solution of Eqs. (5.1)–(5.2) is obtained in the Fourier domain $\hat{\mathcal{E}}_s(\omega, z) = \int d\tau \hat{\mathcal{E}}_s(t, z) e^{-i\omega\tau}$ and in the co-moving reference frame $\tau = t - z/c$, $Z = z$:

$$\begin{aligned} \hat{\mathcal{E}}_s(\omega, z) = & \hat{\mathcal{E}}_s(\omega, -L/2) e^{-i\delta k(z+L/2)} \exp \left\{ -\frac{\text{OD} \cdot |\Omega_c|^2 \gamma_{13}}{i\Delta_{\text{in}}(\Delta_s + i\gamma_{13})^2} \cdot \zeta(\omega, z, -L/2) \right\} - \\ & - \int_{-L/2}^Z dz' \hat{F}_s(\omega, z') e^{-i\delta k(z-z')} \exp \left\{ -\frac{\text{OD} \cdot |\Omega_c|^2 \gamma_{13}}{i\Delta_{\text{in}}(\Delta_s + i\gamma_{13})^2} \cdot \zeta(\omega, z, z') \right\} \end{aligned} \quad (5.8)$$

where we introduced the resonant optical depth $\text{OD} = \frac{nL|g_s|^2}{\gamma_{13}}$ and function $\zeta(\omega, z, z') = \log \left(\frac{\tilde{\gamma}_{12} + i\beta z + i\Delta_{\text{AC}} - i\omega}{\tilde{\gamma}_{12} + i\beta z' + i\Delta_{\text{AC}} - i\omega} \right)$ is responsible for the profile of inhomogeneous broadening. The second line of Equation 5.8 contains a modified Langevin noise operator:

$$\hat{F}_s(\omega, z) = \frac{in g_s}{(\Delta_s + i\gamma_{13})} \left(\frac{\Omega_c \hat{F}_n(\omega, z)}{(\tilde{\gamma}_{12} + i\beta Z + i\Delta_{\text{AC}} - i\omega)} + i\hat{F}_{13}(\omega, z) e^{-i(k_c - k_s)z} \right). \quad (5.9)$$

The resulted model allows us to analyze the noises generated spontaneously in the system due to imperfect experimental conditions. The population on level $|2\rangle$ appears due to imperfect optical pumping or due to strong control field transferring atoms during the writing stage.

5.4 Noise analysis

5.4.1 Dominating noise mechanism

First, to distinguish the Raman scattering from the four-wave mixing, the several dependencies of the noise on experimental parameters are analyzed. FWM is known to be a coherent process which is extremely sensitive to spatial phase-matching, and the noise power contribution from FWM should follow the same behaviour. As a crude test for the presence of FWM, we observed the effect of spatial-mode mismatch on the efficiency and noise (Figure 5.4c). In this measurement, the control field alignment was first optimized for the highest efficiency and then subsequently misaligned from the point on the 90:10 beam splitter where the control field was combined with the probe (Figure 5.1). Noise values correspond to the vacuum-seeded case, meaning no signal (or probe) field was present. From Figure 5.4 it can be seen that as the control field becomes further misaligned the efficiency drops off monotonically, and this is in contrast to the extra noise which stays almost constant with a slight increase near 2 mrad. This behavior of the extra noise is what one would expect under FWM conditions, where the gain exhibits its peak value for a non-zero angle between the \mathbf{k} -vectors of the fields [202]. However, it should be noted that despite this angular dependence, the recorded extra noise level in this measurement was always greater than 1 dB. This signifies to us that while FWM processes may be present and is a main contributing factor to the extra noise. Simultaneously with this there still exists at least one other noise mechanism.

To investigate FWM in our system further, we look at the dependence of the gain peaks present in the Raman spectroscopy versus the single photon detuning (Figure 5.4a) and control field power (Figure 5.4b). First, we use the same experimental configuration except the applied magnetic gradient, and quantify the gain by recording its maximum value as a function of the mentioned parameters. If FWM is the reason for the extra noise, we expect the classical FWM peak to behave in a similar fashion to the quantum extra noise as a function of the experimental parameters. The behavior of the gain with respect to control

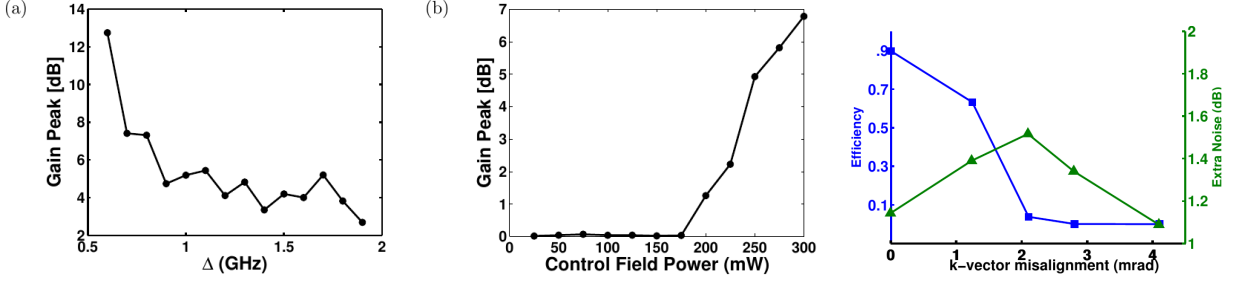


Figure (5.4) Maximum value of the gain peak observed in the vapour cell containing 0.5 Torr Kr buffer gas at 74 °C as a function of (a) single field detuning and (b) control field power. (c) Efficiency and extra noise as a function of control field misalignment.¹

field power is shown in Figure 5.4b, where we see that the gain is absent until about 200 mW at which point it increases substantially. These results possibly indicate that a minimum Rabi frequency is necessary before one can observe gain.²

More importantly, this behavior with the control field power is in disagreement with the plot of the extra noise in Figure 5.6c, where the observed extra noise was present even at control field powers of 100 mW. From these findings we can conclude that while FWM is present in our system and is in all likelihood a contributing factor to the observed extra noise, there exists at least one other mechanism which is induced by the control field. This brings us to the other noise possible source such as incoherent Raman scattering. Further we consider the spectral properties of the emitted noise with and without applied magnetic gradient.

5.4.2 Raman noise analysis

In Figure 5.5a we observe three distinct noise peaks corresponding to the non-degenerate Raman scattering peaks with magnitudes decreasing in accordance with the anticipated population distribution due to the pumping scheme. By applying a sufficient uniform magnetic field, the noise peaks that are not resonant to desired Raman transition can be moved out-

¹The plots and captions were taken from C. Kupchak thesis [198].

²The presented experimental study was done by C. Kupchak

side the bandwidth of the homodyne detector, but the noise corresponding to the resonant Raman absorption line used for GEM remains within the spectrum of the pulse. Under the conditions for optimal retrieval efficiency this resonant noise peak can be as high as 7 dB depending on the operating conditions. When performing GEM with the applied gradient magnetic field, the single noise peak is broadened and subsequently reduced to a magnitude of 1 dB spread uniformly over the spectral width of the pulse (Figure 5.5b).

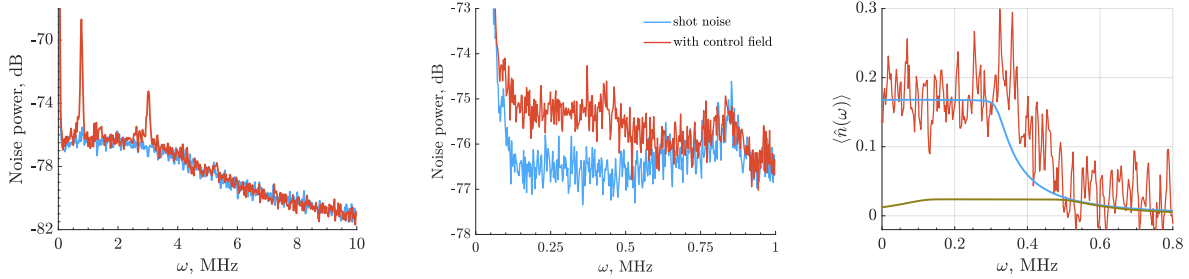


Figure (5.5) Homodyne spectrum (a) near-resonant and (b) resonant to the probe field as measured in the steady state configuration (i.e. no switching of the magnetic fields) with the gradient magnetic field being present. The resolution bandwidth of a spectrum analyzer was set to 30 kHz. The shot noise trace corresponds to only LO being sent to the homodyne detector. (c) The spectrum of noise photons. In red is the experimental data, blue and green lines are theoretical fits for two different Zeeman sublevels.

The experimentally acquired homodyne's noise power (Fig. 5.5 (b)) is converted into number of photons per frequency unit assuming no correlation within a frequency band. The acquired 10-base logarithmic difference between the shot noise and the observed signal is linearly rescaled by $(10^{x/10} - 1)/2$. Division by 2 converts the value into number of photons in frequency band, since for non-squeezed light quadrature variance proportional to twice the photon number $\langle Q^2 \rangle \approx \langle 1 + 2\hat{n} \rangle$.

Next we compare experimentally acquired noise to the model of Raman scattering presented above. The noise spectrum is modelled as the output of atomic sample in case of the vacuum input for the field operator (Eq. 5.8) and is presented in Figure 5.5c. The only nonzero contribution into the power spectrum is from the corresponding Langevin operators:

$$\langle \hat{\mathcal{E}}_s^\dagger(t, L/2) \hat{\mathcal{E}}_s(t, L/2) \rangle = \int \langle \hat{n}(\omega) \rangle e^{-i\omega\tau} d\omega, \quad (5.10)$$

whereas the spectrum is

$$\begin{aligned} \langle \hat{n}(\omega) \rangle &= \iint_{-L/2}^{L/2} dz' dz'' \langle \hat{F}_s^\dagger(\omega, z'') \hat{F}_s(\omega, z') \rangle \cdot \\ &\exp \left\{ -\frac{\text{OD} \gamma_{13} |\Omega_c|^2}{i\Delta_{\text{in}}} \cdot \left(\frac{\zeta(\omega, L/2, z')}{(\Delta_s + i\gamma_{13})^2} - \frac{\zeta^*(\omega, L/2, z'')}{(\Delta_s - i\gamma_{13})^2} \right) \right\}. \end{aligned} \quad (5.11)$$

We can see from Equations (5.3), (5.9) and (5.11), that the strongest contribution into the noise power comes from the $\hat{F}_{12}(\omega, z)$ operator responsible for the ground state decoherence, since it is proportional to the population of level $|2\rangle$ and does not have any Raman suppression coefficient in the form of Ω_c/Δ_s or Ω_I/Δ_I .

Though our formulas are general with a few assumptions, which we have mentioned above, in our calculations we confined ourselves to ^{87}Rb used in the experiment. All parameters necessary for calculations are presented in Table 5.1. The Rabi Frequency ratio $|\Omega_I|/|\Omega_c| = \sqrt{3}$ together with the detuning of the control fields Δ_s dictates the optical pumping rate and prepared population. Since the rate depends as $\sim \frac{|\Omega_{\text{C(I)}}|^2}{\Delta_{s(\text{I})}}$ the extra detuning due to hyperfine splitting $\omega_{21} = 2\pi \cdot 6.8 \text{ GHz}$ cannot fully compensate the repumping from the $|5S_{1/2}, F=1\rangle$ back to $|5S_{1/2}, F=2\rangle$. As the result, only $\sim 85\%$ of the total population is distributed on $|5S_{1/2}, F=1\rangle$ manifold. The redundant population on level $|F=2\rangle$ in conjunction with the decoherence γ_{12} produces the Raman scattering noise presented in Figure 5.5c.

The further increase of the detuning results in larger intensity of the Raman scattering in the signal mode in conjunction with larger population on level $|F=2\rangle$. The dependence of averaged photon number in a signal mode on detuning is presented in Figure 5.6a. The experimental data is averaged over five samples and integrated over the Gaussian waveform. The similar argument applies for power dependence of the noise (Figure 5.6b), but in this case the increase of the noise comes not from the population increase, but from the increased scattering rate, as it scales nonlinearly with power as seen from Equations 5.3 and 5.8.

Moreover, we perform polarization analysis of the noise by projecting its polarization

on superposition of co- and counter-rotating polarizations with respect to the control field ($|\phi\rangle = \cos\theta|\sigma_+\rangle + \sin\theta|\sigma_-\rangle$) by rotating the quarter-wave plate on an angle $\theta/2$ at the output of the memory unit. Our Raman scattering model matches the acquired noise as function of polarization (see Figure 5.6c). The measured polarization $|\phi\rangle$ is mapped into model as a superposition of coupling constants $g_s = g_+ \cos^2\theta + g_- \sin^2\theta$ in 5.9, where g_+ and g_- are the coupling constants for σ_+ and σ_- polarization.

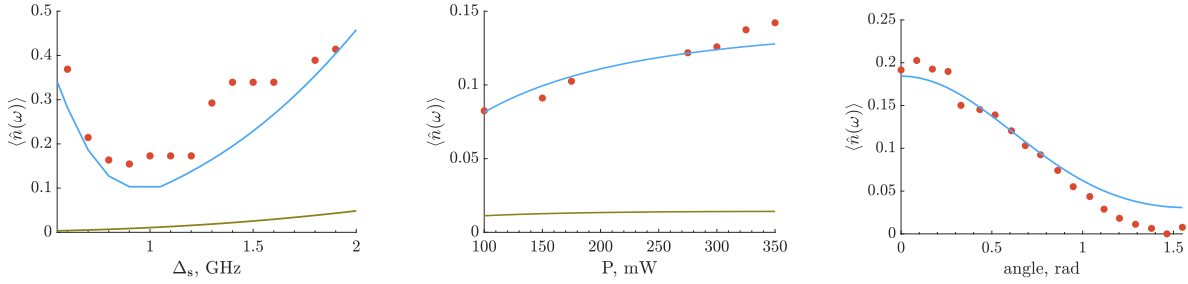


Figure (5.6) (a) An experimental extra noise as measured with increasing single field detuning for vapour cells with 0.5 Torr Kr (red dots). Parameters used in calculations: $P=0.25$ W, $\gamma_{12} = 2\pi \cdot 23.3$ kHz, $g_s = 6.53\sqrt{\text{Hz}}$. (b) Experimental points (red dots) for extra noise as measured with increasing control field power for the vapour cells containing 0.5 Torr Kr buffer gas are given in blue color. An orange solid line represents theoretical model. Parameters used in calculations: $P=0.34$ W, $\gamma_{12} = 2\pi \cdot 40$ kHz, $g_s = 2.9\sqrt{\text{Hz}}$. (c) The polarization dependence of the integrated number of noise photons versus the analyzing angle. Selecting initially co-rotating circular polarization and rotating the quarter-wave plate until the orthogonal circular polarization is selected.

γ_{12}	γ_{13}	γ_{23}	r_{13}	r_{23}	Ω_c	Ω_I	Δ_s	Δ_I	Δ_{in}
0.04	1.43	1.43	1.43	1.43	16.6	28.78	1330	5504	0.68

β , [MHz/m]	n , [1/m ²]	L , [m]	P , [W]	S_c , [m ²]	S_s , [m ²]	g_s , [$\sqrt{\text{Hz}}$]
$2\pi \cdot 3.2$	$4.5 \cdot 10^{14}$	0.2	0.34 (*)	$28 \cdot 10^{-6}$	$3 \cdot 10^{-6}$	2.9 (*)

Table (5.1) Parameters used in calculations. (*) unless otherwise specified. The parameters in the upper table are in MHz/(2 π).

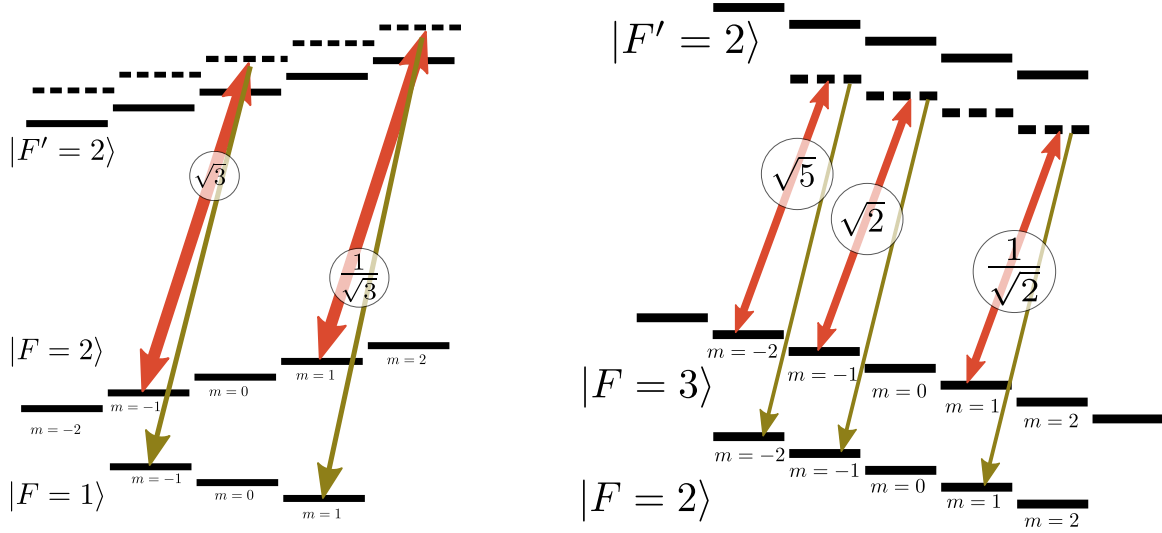


Figure (5.7) Assuming constant magnetic field aligned along the propagation of the control and signal fields we present the possible Λ schemes to be utilized in GEM scheme for co-rotating polarizations. For each Λ scheme the ratio $|\Omega_c|/|\Omega_I|$ for σ_+ polarization are presented, whereas the control and signal fields are represented by the thick red line and thin green respectively. (a) Available transitions for σ_+ polarization in Rubidium 87. (b) Available transitions for σ_+ polarization in Rubidium 85.

5.5 Conclusion

We conducted the analysis of gradient echo memory noise performance in warm rubidium vapor. At quantum efficiency of more than 80% we reveal, that depending on the experimental conditions the memory produces 0.1-0.3 noise photons per pulse even for a vacuum input. The mechanism responsible for the noise was identified as the Raman scattering from the residual population.

Performing the noise analysis and its modeling we noticed two main factors responsible for the noise. First, the intensity of Raman scattering is sensitive to the polarization and the magnetic sublevels used for the Λ scheme. These factors strongly modify the control field Rabi frequency Ω_I on the signal transition. The straightforward way to exploit this fact is to use different Λ scheme within ^{87}Rb , which provides better Ω_I/Ω_c ratio. It can be done by choosing states with suitable Clebsch-Gordan coefficients for a given polarization, examples for ^{85}Rb and ^{87}Rb for co-rotating σ_+ polarization are presented in Figure 5.7. From the

symmetrical consideration if the pump has σ_{\pm} polarization, the states providing the best noise suppression are $m = \mp 1$. The ratio of $\Omega_1/\Omega_c = 1/\sqrt{3}$ would result in 0.02 averaged noise photons for vacuum input that is similar to the EIT-based memories [203].

Secondly, the blue-detuned control field resulted in higher pumping ratio for state $|2\rangle$, which enhanced the Raman scattering rate on the signal transition. The use of red detuning in theory would eliminate this problem. However, it may come at an expense of losing the convenient control field filtering, because the control field will no longer be in resonance with a transition of ^{85}Rb . By reversing the roles (of filtering and memory cell) of ^{85}Rb and ^{87}Rb could result in the red-detuned memory with an atomic filtering. Moreover, the combination of ^{85}Rb with the low noise Λ scheme (see Figure 5.7), with the ratio of Rabi frequencies $\Omega_1/\Omega_c = 1/\sqrt{5}$, theoretically decreases the number of noise photons below 0.01.

Employing the mentioned noise minimization in conjunction with long-lived spin-exchange relaxation-free states [56] may open an avenue for realizing a noise-free efficient quantum memory with a storage lifetime of a second in warm vapor.

Chapter 6

Time-bin quantum random access memory

6.1 Introduction

It is well known, that the construction of universal quantum computer and long-distance communications pushes an intensive elaboration of the multi-qubit quantum memory. In turn, the desire to involve the QM devices in a processing of quantum information encourages the development of the control methods of QM operation. Quantum random access memory (qRAM) represents one of the such promising devices. In contrast to a usual QM [51], the qRAM provides the arbitrary access to the M data cells ($|D_1\rangle \dots |D_M\rangle$) by the quantum superposition of the address states ($|\Psi^a\rangle = \sum_{n=1}^M \alpha_n |\psi_n^a\rangle$): $|\Psi^a\rangle \xrightarrow{\text{qRAM}} \sum_{n=1}^M \alpha_n |\psi_n^a\rangle |D_n\rangle$ [2]. The qRAM holds the promise of the exponential enhancement for a number of data processing tasks such as a quantum search over a classical database [204], discrete logarithms [205], quantum Fourier transformation [2] and collision finding [206]. The first feasible qRAM architecture was proposed by Giovanetti et al [207, 208] and developed [209] in the so-called bucket-brigade architecture.

In the original proposal [207, 208], qRAM contains $2M - 1$ nodes with $M = 2^m$ single

qubit QM cells (where $m = 1, 2, \dots$ is a non-negative integer) and $M - 1$ quantum logical elements routing the signal to the individual QM cells.

All the nodes are connected in a binary tree with logical elements are located in the front nodes starting from the top while the last level of the tree is an array of QM cells (see Figure 6.1A). The addressing is performed via transfer of the address qubits one at a time through the binary tree starting from the root node. Each logical element has three internal quantum states. Initially all the elements are in the ‘wait’ states. The ‘wait’ state is switched into the superposition of two other states $|0\rangle, |1\rangle$ by the input address qubit. The logical element in the state $|0\rangle$ or $|1\rangle$ acts as the switch that routes the following address qubit to the next right or left set of the nodes respectively. The sequential input of all the address qubits creates the route to the desired memory cells. By initializing all logical elements in the ‘wait’ state and sending address qubits one by one it is possible to build a route to the desired memory cell. An example of three qubit addressing is presented in Figure 6.1A, where the two nodes are in the state $|1\rangle$ and one - in the state $|0\rangle$.

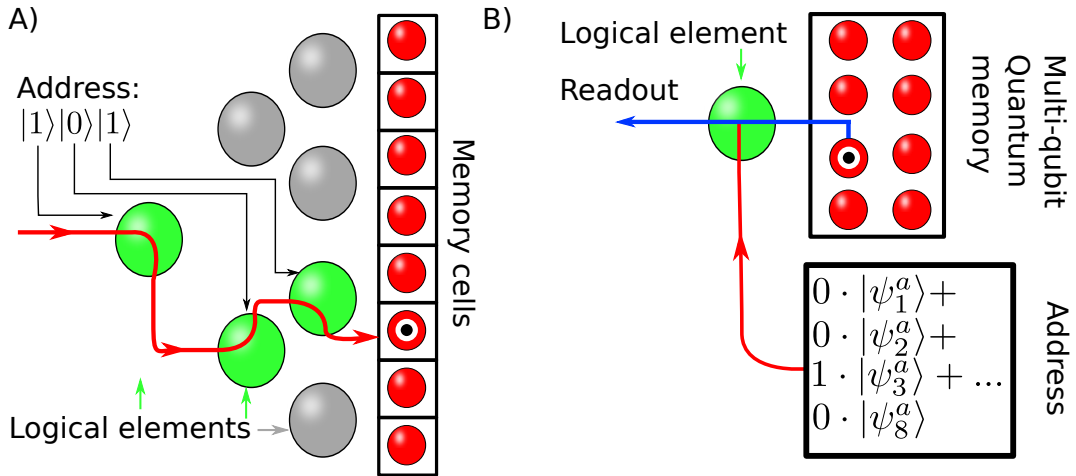


Figure (6.1) A) Each logical element in the bucket-brigade architecture [207] has three internal states: $|0\rangle$, $|1\rangle$ and “wait” state. While in the state $|0\rangle$ or $|1\rangle$, the logical element routes the signals to up (left) or to down (right), respectively. The ‘wait’ state is switched into the superposition of two other states $|0\rangle, |1\rangle$ by the input address qubit. B) The time-bin qRAM architecture uses one multi time-mode QM cell and one logical element. The quantum addressing is realized by using single photon distributed in M time-bin wavepackets depending on the photonic wavepacket state at particular time t .

Exponential speed up over the classical computation rate requires an operation of the qRAM with sufficiently large number of the QM cells. At the same time a qRAM device should be compact and easily integrable into the developing hybrid quantum circuits [210] and network [211]. However, due to the large number of logical elements and QM cells, the bucket-brigade qRAM scheme is faced with comprehensive difficulties in experimental implementation that limits its practical feasibility. In this work, instead of M single qubit QM cells used in the bucket-brigade scheme, we propose an atomic ensemble in cavity for storage of M photonic qubits on the orthogonal temporal modes of the atomic coherence¹ (see Figure 6.1B). This also allows us to reduce the number of the logical elements from $M - 1$ to just one control four- (or three-) level atom. The logical element depending on its state either permits the readout of the data from the memory cell or block it. Herein, the quantum address operation is achieved by temporally synchronized coupling of the control atom to the readable photonic qubit.

The control atom is suited in the front cavity which is connected with the neighboring resonant cavity containing the QM atomic ensemble (see Figure 6.2). The atomic transitions $|g_c\rangle \leftrightarrow |e_c\rangle$ and $|g_c\rangle \leftrightarrow |a_c\rangle$ are strongly coupled to the front cavity modes \hat{a}_1 and \hat{a}_d while the fourth ground level $|au\rangle$ is decoupled from the cavity modes. The coherent control of the atomic states can provide a quantum turnstile for transfer of the photonic qubits to/from the atomic ensemble. If the control atom state is far off the resonance with the front cavity modes (i.e. the atom stays on the fourth level), the incoming photon will be ideally transmitted into the QM cell, or retrieved, respectively, into the free space. Thus by initializing the control atom into the off-resonance state, it is possible to record (and retrieve) many ($M \gg 1$) photonic qubits subsequently into the atomic ensemble. However, if the control atom is in the ground state resonant to the front cavity mode \hat{a}_1 , the incoming/retrieved photon will be reflected back.

For the implementation of qRAM operation, we control the atomic state by a single

¹ Spatial QM modes can be also exploited in this proposal and this opportunity will improve the practical implementation of the proposed scheme. However this issue deserves special further analysis.

photon state which is distributed in a superposition of M temporal wavepackets (i.e. it is a M time-bin photon) $|\Psi^a\rangle_f = \sum_{n=1}^M \alpha_n |\psi_n^a\rangle_f$. Herein, $|\psi_n^a\rangle_f$ is the n -th photonic wavepacket and related to control the readout of n -th photon qubit from the atomic ensemble. Each photon wavepacket can control the state of logical element for writing and readout stages of the QM operation. Thus, the multi-time bin photon plays the role of the address state in the qRAM operation. It is worth noting that from the functional point of view this qRAM architecture with M stored qubits and one logical element is equivalent to the bucket-brigade qRAM with $M - 1$ logical elements and M cells of single qubit QMs. Below we describe the physical processes providing the qRAM operation.

It is possible to use a number of the multi-atomic QMs for the proposed qRAM scheme. However, in this work we focus on the photon echo technique [31, 129] which can provides a multi-qubit capacity [212] due to the inhomogeneous broadening (IB) of the resonant atomic transition.

Such technique has been successfully demonstrated for the multi-mode storage of single photon fields [213, 214] and more than 1000 temporal light pulses [45]. Moreover, the photon echo QM technique has demonstrated the record quantum efficiency [127, 39, 215, 216] that gives a credit for realization of the controlled perfect light-atom dynamics. Recently the photon echo QM has been further developed [217, 173] and successfully demonstrated [218, 219] for small atomic ensembles in the impedance matching cavities. This approach opens the opportunities for implementation of compact multi-qubit QM devices. Such photon echo QM scheme is also applicable in the microwave spectral range [220, 221, 222, 223, 224] for the integration into quantum computer schemes [225] and it can work with intensive quantum light fields [226, 227].

In the second section, we describe physical properties of the proposed scheme. First, we study the case of a single photon storage as the basic QM benchmark. After that we present the solution of the dynamical equations for the various stages of qRAM operations. Based on the obtained analytical solutions, we present the set of physical conditions (Eqs.

6.12,6.13,6.14) allowing effective multi-qubit quantum storage for subsequent qRAM operations. In the third section, we describe the quantum addressing protocol based on the time-reversible mapping of multi-time-bin single photon state on the control atom. Finally, we discuss implementation of the proposed qRAM scheme by using current optical and microwave techniques and we outline the potential advantages that are feasibly achievable experimentally.

6.2 Scheme

6.2.1 Single photon storage

The diagram of the proposed qRAM scheme is shown in Figure 6.2. We have analyzed

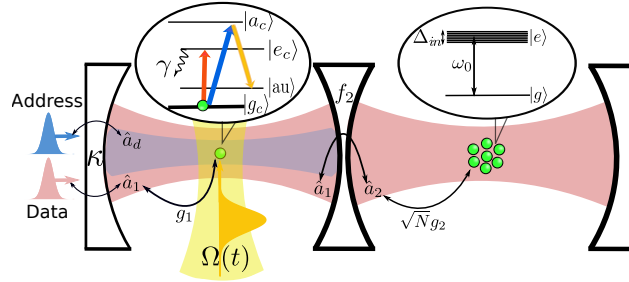


Figure (6.2) Free propagating modes $\hat{b}(\omega)$ are coupled to a resonant field modes \hat{a}_1 and \hat{a}_d of the double sided front cavity. This cavity contains a single four-level atom with the optical transitions: $|g_c\rangle \leftrightarrow |e_c\rangle$ is resonant to the cavity mode \hat{a}_1 and $|g_c\rangle \leftrightarrow |a_c\rangle$ is resonant to the addressed cavity mode \hat{a}_d . The atomic transition $|g_c\rangle \leftrightarrow |e_c\rangle$ is characterized by the frequency ω_0 , the coupling constant g_1 and by the decay rate γ due to the interaction with the bath field modes $\hat{c}_m(\nu)$ (there are similar parameters for the transition $|g_c\rangle \leftrightarrow |a_c\rangle$); κ is the decay rate of the cavity mode into the free propagating modes $\hat{b}(\omega)$, the arrow aligned with Ω indicates the control laser field with the Rabi frequency on the transition $|a_c\rangle \leftrightarrow |au\rangle$. The other side of the front cavity mode \hat{a}_1 is coupled (with the rate f_2) to the second cavity mode \hat{a}_2 . The QM atoms have the inhomogeneous broadening Δ_{in} of the resonant line and the collective coupling constant $\sqrt{N}g_2$ for the interaction with the cavity mode \hat{a}_2 .

the quantum storage of an input single photon wave packet:

$$|\psi_{\text{in}}(t)\rangle_f = \int d\nu \alpha_\nu^0(t) \hat{b}^\dagger(\nu) |0\rangle_f, \quad (6.1)$$

which is launched into the first cavity in the presence of the control three-level atom. Amplitudes $\alpha_\nu^0 = \alpha_\nu(-\infty)$ characterize the state of the input photon wave packet with normalization value $\int d\nu |\alpha_\nu^0|^2 = 1$. $\hat{b}^\dagger(\nu)$ and $\hat{b}(\nu)$ are the creation and annihilation operators of ν -th field mode where $[\hat{b}(\nu), \hat{b}^\dagger(\nu')] = \delta(\nu - \nu')$; $|0\rangle_f$ is the vacuum state of these modes.

Assuming that the control atom and all QM atoms are in their respective ground states $|g_c\rangle$ and $|g\rangle \equiv \prod_{j=1}^N |g_j\rangle$, the initial wave function takes the form

$$|\Psi(t \rightarrow -\infty)\rangle = |\psi_{\text{in}}(t)\rangle_f |g_c\rangle |g\rangle. \quad (6.2)$$

The subsequent dynamics of resonant light-atom interactions is described by the wave function (see Appendix B.1):

$$\begin{aligned} |\Psi(t)\rangle = & \left(\beta_c \hat{S}_+^c + \sum_{j=1}^N \beta_j \hat{S}_+^j + \alpha_1 \hat{a}_1^\dagger + \alpha_2 \hat{a}_2^\dagger + \alpha_d \hat{a}_d^\dagger \right. \\ & \left. + \int d\nu \alpha_\nu \hat{b}^\dagger(\nu) + \sum_m \int d\omega r_\nu^m \hat{c}_m^\dagger(\nu) \right) |0\rangle_f |g_c\rangle |g\rangle, \end{aligned} \quad (6.3)$$

with normalization

$$|\beta_c|^2 + |\alpha_1|^2 + |\alpha_2|^2 + |\alpha_d|^2 + \sum_{j=1}^N |\beta_j|^2 + \int d\nu |\alpha_\nu|^2 + \sum_m \int d\nu |r_\nu^m|^2 = 1 \quad (6.4)$$

and initial conditions $\beta_c(-\infty) = \beta_j(-\infty) = \alpha_{1,2}(-\infty) = r_\nu^m(-\infty) = 0$. In Eq. 6.3 we describe the atomic dynamics by effective spins 1/2, where \hat{S}_+^j , \hat{S}_-^j and \hat{S}_+^c , \hat{S}_-^c are the ladder spin operators of j -th memory atom and the control atom respectively; $\hat{a}_{1,2}^\dagger$ and $\hat{a}_{1,2}$ are creation and annihilation operators of the 1-st and 2-nd cavity field modes; $\hat{c}_m(\nu)$, $\hat{c}_m^\dagger(\nu)$ are the bosonic operators of the bath modes interacting with the control atom in the first

cavity $([\hat{c}_m(\nu), \hat{c}_n^\dagger(\nu')]) = \delta_{m,n}\delta(\nu - \nu')$.

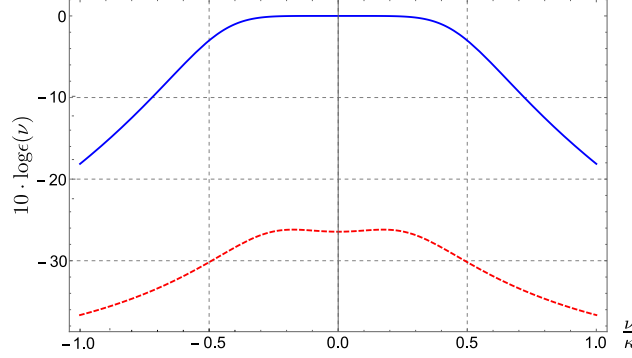


Figure (6.3) Spectral transfer function in the logarithmic scale $10 \log \epsilon(\nu/\kappa)$ for the single photon storage (blue solid line) and for the blockade (red dashed line). The wide spectral window for the photonic storage is implementing by three impedance matching conditions (6.12, 6.13, 6.14). The strength of the blockade of the memory process is represented by the single-atom cooperativity factor $C = 10$ and $\gamma = \kappa$.

Using the well-known input-output formalism [33], we solve the Schrödinger equation for the wave function $|\Psi(t)\rangle$ (see Appendix B.1). Here, we obtain the following atomic amplitudes

$$\beta_j(\Delta_j, t) = i\sqrt{2\pi\kappa}\frac{g_2}{f_2}F(\Delta_j)\alpha_{\Delta_j}^0 e^{-i(\Delta_j - i/T_2)t}, \quad (6.5)$$

for the sufficiently large interaction time $t > \delta t$, where δt is a temporal duration of the input photon wavepacket:

$$F(\Delta) = \frac{f_2^2}{(Ng_2^2\tilde{G}(\Delta) - i\Delta)(\frac{\kappa}{2} + \frac{ig_1^2}{\Delta - \delta + i\gamma/2} - i\Delta) + f_2^2}, \quad (6.6)$$

where $\tilde{G}(\Delta) = \int d\nu \frac{G(\nu)}{1/T_2 + i(\nu - \Delta)}$, $G(\nu)$ is the formfactor of the IB-resonant line, T_2 is the decoherence time of the atomic ensemble in QM, f_2 is the coupling constant between two cavities, $\sqrt{N}g_2$ is the collective interaction constant between the second cavity mode and atoms, κ is the linewidth of the first cavity, and γ is the linewidth of the control atom (see Appendix B.1). We have used the continuous limit for the large number of atoms in QM: $\sum_{j=1}^N \dots \rightarrow N \int d\Delta G(\Delta) \dots$ and $\beta_j(\Delta_j, \tau) \rightarrow \beta(\Delta, \tau)$.

We find the probability of the photon transfer in QM using Eq. 6.5:

$$P_a(t > \delta t) = \sum_{j=1}^N |\beta_j(t)|^2 = N \int_{-\infty}^{\infty} d\Delta G(\Delta) |\beta(\Delta, t)|^2 = \int_{-\infty}^{\infty} d\Delta \epsilon(\Delta) |\alpha_{\Delta}^0|^2. \quad (6.7)$$

As it is seen in Eq. 6.7, the qRAM can be characterized by its spectral efficiency

$$\epsilon(\Delta) = 2\pi N \kappa \left| \frac{g_2}{f_2} \right|^2 G(\Delta) |F(\Delta)|^2 \quad (6.8)$$

for the single photon storage. For simplicity, but without compromising the generalization, we assume IB to be Lorentzian $G(\nu) \equiv G_L(\nu) = \frac{\Delta_{\text{in}}}{\pi(\nu^2 + \Delta_{\text{in}}^2)}$ with bandwidth Δ_{in} . For the narrow bandwidth of the input photon field ($\delta\omega_f \sim \delta t^{-1} \ll \kappa, \Delta_{\text{in}}$), we find that the following resonant quantum efficiency

$$\epsilon(\Delta \approx 0) = \frac{4C_{\text{pm}}}{(1 + C_{\text{pm}} + \frac{\gamma^2 C}{\delta^2 + (\gamma/2)^2})^2 + (\frac{2\delta\gamma C}{\delta^2 + (\gamma/2)^2})^2}, \quad (6.9)$$

determines the main properties of qRAM, where $C = \frac{g_1^2}{\kappa\gamma}$ is the well-known single-atom cooperativity factor. We have also introduced a *cooperativity factor of photonic molecule*:

$$C_{\text{pm}} = |f_2|^2 / \left(\kappa \frac{Ng_2^2}{2\Delta_{\text{in}}} \right). \quad (6.10)$$

We note that a strong interaction of two closely placed cavities creates a photonic molecule, which plays an important role in the controlled photon transfer in the atomic ensemble. The photonic molecular factor C_{pm} characterizes the relative strength of dynamical and dissipative processes of a photon distributed in two coupled resonant cavities. Here, the f_2 -constant determines oscillation frequency of the photon between two quantum states of the photonic molecule: the photon exists in either the first or in the second cavity. Parameters κ and $Ng_2^2/(2\Delta_{\text{in}})$ characterize the decay processes of a photon in these two cavities.

By analyzing Eq. 6.9, we find two basic regimes of the qRAM operation: 1) storage (or

retrieval) of a single photon in the QM ensemble and 2) blockade of these processes.

6.2.2 Impedance matching conditions

Perfect storage is possible for large spectral detuning of the control atom $|\delta| \gg \gamma C$. It can be achieved by transferring the atom to the third ancillary state $|au\rangle$ (see Figure 6.2). In this case the resonant storage efficiency (6.9) is:

$$\epsilon(0) \big|_{|\delta| \gg \gamma C} \equiv \epsilon_R(0) = 4C_{\text{pm}}/(1 + C_{\text{pm}})^2, \quad (6.11)$$

that demonstrates the ideal recording (index “R”) of a photon into the QM ensemble for

$$C_{\text{pm}} = 1, \quad (6.12)$$

which we call as the first impedance matching (IM) condition of the effective qRAM where $\epsilon(0) = 1$ that provides an efficient quantum storage for resonant frequency ($\Delta = 0$). We note that the first IM condition coincides formally with the impedance matching photon echo QM [217, 173] although the photon storage occurs in the presence of the additional cavity in front and the condition is related to the property of the photonic molecule. At the same time, the impedance photon echo QM [217, 173] is characterized by different coupling constants: by the collective atomic coupling constant $\sqrt{N}|g_2|$ and by the decay constants κ and Δ_{in} , where κ is responsible for the photon leakage from the cavity and Δ_{in} determines the decay rate of the excited atomic coherence. These parameters satisfy the condition $\kappa\Delta_{\text{in}} = 2N|g_2|^2$. It is possible to generalize the values pertinent to this condition and facilitate its implementation by using the off-resonant Raman echo QM scheme [228].

The IM condition modifies several different physical parameters and we will see how the condition can lead to implementation of broadband qRAM operation. Analyzing $\epsilon(\nu)$ for

the transfer process we found the second

$$\frac{N |g_2|^2}{\Delta_{\text{in}}} = \frac{\Delta_{\text{in}} \kappa / 2}{(\Delta_{\text{in}} + \kappa / 2)}, \quad (6.13)$$

and the third

$$\Delta_{\text{in}} = \kappa / 2, \quad (6.14)$$

IM conditions, where the highest quantum efficiency $\epsilon(\nu)$ gets almost ideally flat spectral behavior (see Figure 6.3) around $\nu \approx 0$ that is expressed in the equation

$$\epsilon_{\text{R}}(\nu) = \frac{1}{1 + (\frac{\nu}{\kappa/2})^6}, \quad (6.15)$$

and which provides an efficient transfer of the broadband input single photon field in QM atomic ensemble. This process transfers the input photon wave function (6.2) into the atomic state $|\Psi(t > \delta t)\rangle \cong |0\rangle_f |au\rangle_c \left(\sum_{j=1}^N \beta_j(t) \hat{S}_+^j \right) |g\rangle$.

The three IM conditions provide the broadband one way storage for many photon qubits flying one by one into the QM cell. The large bandwidth is a result of the specific (almost equal, i.e. $\frac{N|g_2|^2}{\Delta_{\text{in}}} = \frac{\kappa}{4}$) coupling of the photonic molecule with the free propagating light modes and with the QM atoms.

6.2.3 Photonic transfer blockade

In the case of the resonant interaction with the control atom, when the atom remains in the state $|g\rangle_c$ where $\delta = 0$, we find from Eq. 6.11

$$\epsilon(0)_{|\delta=0} \equiv \epsilon_{\text{B}}(0) = 4C_{\text{pm}} / (1 + C_{\text{pm}} + 4C)^2, \quad (6.16)$$

that in turn leads to

$$\epsilon_B(0)|_{C_{\text{pm}}=1} = (1 + 2C)^{-2}, \quad (6.17)$$

if the first IM condition 6.12 holds. By taking the single-atom cooperativity factor C from the experimental data [210] for the single atom in the optical Fabry-Perot cavity $C \equiv C_{\text{opt}} = 30$ and for the superconducting qubit in the moderate microwave resonator $C \equiv C_{\mu\text{w}} = 300$, it is possible to achieve blockade with $\epsilon_{B,\text{opt}} = 2.6 \cdot 10^{-4}$ and $\epsilon_{B,\mu\text{w}} \approx 3 \cdot 10^{-6}$.

The most important benchmark of the photon blockade is a reflection of the input photon field. The direct usage of the input-output relationship $\alpha_{\text{in}}(\nu) + \alpha_{\text{out}}(\nu) = \sqrt{\kappa}\alpha_1(\nu)$ and the relation $\alpha_1(\nu) = A_{1,\text{in}}(\nu)\alpha_{\text{in}}(\nu)$ (see $A_{1,\text{in}}(\nu)$ in the Appendix B.1) leads to

$$\alpha_{\text{out}}(\nu) = f_B(\nu)\alpha_{\text{in}}(\nu), \quad (6.18)$$

where

$$f_B(\nu) = \frac{i\kappa}{\nu + \frac{i\kappa}{2} - \frac{g_1^2}{\nu - \delta + i\gamma/2} - \frac{f_2^2}{\nu + iNg_2^2\tilde{G}(\nu)}} - 1. \quad (6.19)$$

Here for a sufficiently narrow spectral width of the stored light ($|\nu| < \kappa$) and the resonant interaction with control atoms ($\delta \cong 0$) we obtain

$$f_B(|\nu| < \kappa) |_{\delta=0} \rightarrow \left(\frac{1}{\frac{1+C_{\text{pm}}}{2} + 2C} - 1 \right). \quad (6.20)$$

Taking into account the first IM condition $C_{\text{pm}} = 1$ we find for Eq. 6.18

$$\alpha_{\text{out}} = -\frac{2C}{(1 + 2C)}\alpha_{\text{in}}. \quad (6.21)$$

The reflection 6.21 is valid with high accuracy within the memory bandwidth $\sim \kappa$ (see Fig.

6.3). Inserting the same values for the single-atom cooperativity factor we obtain $\left| \frac{\alpha_{out}}{\alpha_{in}} \right|^2 = 0.983$ and 0.996 for $C \equiv C_{opt} = 30$ and $C \equiv C_{\mu w} = 300$, respectively, that is a rather strong photonic blockade.

6.2.4 Echo photon retrieval

Implementing the CRIB procedure for the retrieval of the stored single photon field, we invert the atomic detuning $\Delta_j \rightarrow -\Delta_j$ at the time $t = \tau$. In general, one might also use some other experimental methods for rephasing the atomic coherence, such as AFC- or silent echo protocols (i.e. the protocols using the atomic systems with natural IB of resonant line). However, we further consider CRIB due to its perfect time reversibility.

Initially all free propagation modes and three cavity modes ($\hat{a}_1, \hat{a}_d, \hat{a}_2$) are in the vacuum state and the control atom is in the ground state $|g_c\rangle$, while there is an excited QM atomic coherence determined by the atomic amplitudes $\beta_j(\Delta_j, \tau)$. We find the wave function (see the Appendix B.2) of the light-atomic system for the time $t \gg 2\tau$ with the following spectral photonic amplitude $\alpha_\nu(t)$:

$$\alpha_\nu(t) = -2\pi\kappa N \left| \frac{g_2}{f_2} \right|^2 G_L(\nu) F_S(-\nu) F_R(\nu) \cdot \alpha_{-\nu}^0 e^{-i\nu(t-2\tau)-2\tau/T_2}, \quad (6.22)$$

where indices S,R denote the *storage* and the *retrieval* stages. In turn, the states $|g_c\rangle$ and $|au\rangle$ of the single atom correspond to *blockade* (B) and *transfer* (T) regimes. If the control atom stays in the state $|au\rangle_c$ (i.e., $S, R \rightarrow T$), we find from Eq. 6.22 the following quantum efficiency of the photon retrieval:

$$\epsilon_{\text{echo}}|_{\delta\omega_f \leq 0.2\kappa} \cong \frac{16C_{\text{pm}}^2 e^{-4\tau/T_2}}{(1 + C_{\text{pm}})^4} \Big|_{C_{\text{pm}}=1} = e^{-4\tau/T_2}, \quad (6.23)$$

where the amplitude of the irradiated photon field is $\alpha_\nu(t) \cong -\alpha_{-\nu}^0 \exp\{-i\nu(t-2\tau)-2\tau/T_2\}$, that indicates the perfect time-reversal retrieval of the initial single photon state under the

condition of the long-lived coherence time $2\tau/T_2 \ll 1$. The probability of the photon retrieval for the different decoherence time T_2 and pulse duration δt is presented in Figure 6.4.

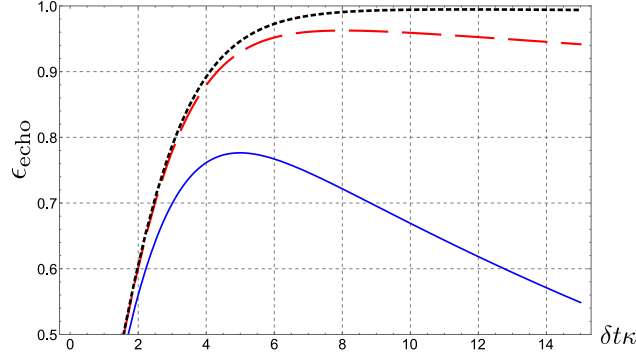


Figure (6.4) Efficiency of the echo photon retrieval as a function of the Gaussian pulse duration δt (in units $\delta t \kappa$) for different atomic relaxation times T_2 : $T_2 \kappa = 10^2$ (blue, solid line); $T_2 \kappa = 10^3$ (red, long dashed line); $T_2 \kappa = 10^4$ (black, short dashed line) when the three IM conditions hold.

If the control atom is prepared in the ground state $|g_c\rangle$ and $\delta = 0$, the photon retrieval is blocked. In this case, there is a following equation for the photon emission probability:

$$\epsilon_{\text{echo}} = e^{-4\tau/T_2} \int_{-\infty}^{\infty} d\Delta \epsilon_R(\Delta) \epsilon_B(\Delta) |\alpha_{\Delta}^o|^2 \Big|_{\delta\omega_f \leq 0.2\kappa, C_{pf}=1} \cong \frac{e^{-4\tau/T_2}}{(1+2C)^2} \Big|_{C \geq 10} < 0.0023, \quad (6.24)$$

which describes the strong blockade of the storage state, when the echo photon is efficiently reabsorbed by the QM atomic ensemble. At the same time, the atomic amplitudes grasp the additional π -shift: $\beta(\Delta, \tau) e_{t < 2\tau}^{i\Delta t} \rightarrow -\beta(\Delta, \tau) e_{t > 2\tau}^{i\Delta t} e^{-(t-\tau)/T_2}$ as a result of the echo photon reabsorption.

6.3 Quantum addressing

Here we demonstrate a method for the quantum addressing of the retrieval stage by assuming rather large time T_2 of the atomic coherence ($T_2 \kappa \geq 10^4$, see Figure 6.4). Let us suppose that initially M photon qubits in the state $\prod_{n=1}^M |\psi_{in,m}(t - t_m)\rangle_f$ were stored, one

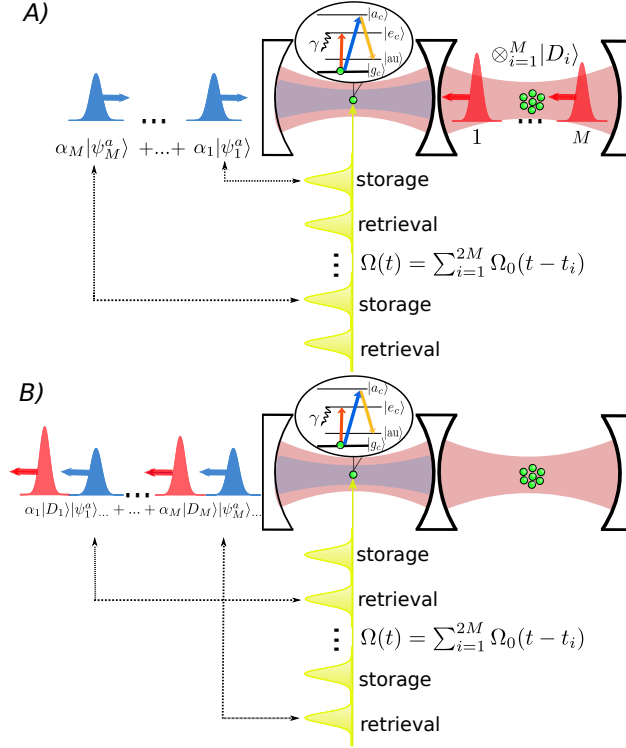


Figure (6.5) Quantum addressing is accomplished by the temporal synchronization between the external quantum control of four-level atom and the readout of M photonic states from the QM cell. A) The control atom is transferred into the superposition of states $|g\rangle_c$ and $|au\rangle_c$ via lambda-transition by the address single photon in the presence of laser pulse sequence $\Omega(t)$. The address single photon is represented by M time-bin wavepackets entering the left cavity. The stored M photonic states are symbolically depicted by M pulses in the right cavity. B) The retrieved state describes the entangled two-photon field in the sequence of M wavepacket pairs flying from the qRAM cell. The irradiated field contains the data and address photons. The two-photon field is also entangled with the quantum data remaining in the QM atomic ensemble. The control atom is returned to the ground state after the whole procedure.

by one, in the atomic ensemble. After the storage qRAM is in the state

$$|\text{qRAM}_1\rangle = |\text{QM}\rangle |au\rangle_c, \quad (6.25)$$

where

$$|\text{QM}\rangle = \hat{S}_{(M)}^+(t - t_M) \dots \hat{S}_{(1)}^+(t - t_1) |g\rangle, \quad (6.26)$$

then $\hat{S}_{(m)}^+(t - t_m) = \sum_{j=1}^N \beta_j^{(m)}(\Delta_j, t - t_m) \hat{S}_+^j$ describes a collective single atomic excitation caused by the absorption of the m -th photonic qubit at the time $t \approx t_m$.

All M atomic excited coherences are decoupled from each other due to $M \ll N$ and strong reciprocal dephasing. Such separable quantum state of M qubits in qRAM can be formally represented as the product $|\text{QM}\rangle = \prod_{m=1}^M |D_m\rangle$, where M states are orthogonal $\langle D_{m'} | D_m \rangle \sim \delta_{m,m'}$. The state $|D_m\rangle$ can be interpreted as the state of m -th qubit in the multi-qubit QM cell, where t_m is a time-label of this qubit.

In the case of m' qubit readout, the quantum state of qRAM transforms as follows:

$$\begin{aligned} |0\rangle_f |\text{qRAM}_1\rangle &\rightarrow -|\psi_{\text{in},m'}\rangle_f \hat{S}_{(M)}^+(t - t_M) \\ &\quad \dots \hat{S}_{(m'+1)}^+(t - t_{m'+1}) \hat{S}_{(m'-1)}^+(t - t_{m'-1}) \\ &\quad \dots \hat{S}_{(1)}^+(t - t_1) |au_c\rangle |g\rangle \\ &\equiv -|\psi_{\text{in},m'}\rangle_f |au_c\rangle |\emptyset_{m'}\rangle \prod_{m \neq m'}^M |D_m\rangle. \end{aligned} \quad (6.27)$$

The photon retrieval is possible, since the control atom is in the state $|au_c\rangle$. As it is seen in Eq. 6.27, the $M - 1$ qubits are still stored in the QM, while m' -qubit has been irradiated into the free space associated with the quantum state $|\psi_{\text{in},m'}\rangle_f$, $|\emptyset_{m'}\rangle$ represents an empty m' cell of the QM.

Analogously, if the m' -th and the m'' -th stored qubits are irradiated one by one from

qRAM, the output state will be with two retrieved photon qubits and two empty cells:

$$|0\rangle_f | \text{qRAM}_1 \rangle \rightarrow |\psi_{\text{in},m'}\rangle_f |\psi_{\text{in},m''}\rangle_f |au_c\rangle |\emptyset_{m'}\rangle |\emptyset_{m''}\rangle \prod_{m \neq m', m''}^M |D_m\rangle. \quad (6.28)$$

Before the addressing the control atom stays in the state $|g_c\rangle$:

$$| \text{qRAM}_2 \rangle = | \text{QM} \rangle | g_c \rangle. \quad (6.29)$$

For the quantum addressing we use a single photon wave packet distributed in M time-bins (M coinciding with the number of photon qubits stored in the QM) that is described by the following quantum superposition:

$$|\Psi^a\rangle_f = \sum_{n=1}^M \alpha_n |\psi_n^a(t)\rangle_f, \quad (6.30)$$

$$|\psi_n^a(t)\rangle_f = |\psi^a[-(t - (n-1)\tau_o - t_c)]\rangle_f \quad (6.31)$$

where $\sum_n |\alpha_n|^2 = 1$. The input wave packet is represented by a wavefunction

$$|\psi^a(t)\rangle_f = \int dz g(t - z/c, \delta z_f) e^{-i\omega(t-z/c)} \hat{a}^\dagger(z) |0\rangle_f \quad (6.32)$$

where $\hat{a}^\dagger(z)$ is field with commutation relationship $[\hat{a}(z), \hat{a}^\dagger(z')] = \delta(z - z')$, $g(t)$ describes the temporal shape of the photon wave packet. We assume the duration of each time-bin is much smaller than the distance between two nearest time-bins $\delta z/c \ll T_0$, δz is its spatial longitudinal size. The states in Eq. 6.30 are orthogonal ${}_f\langle \psi_n^a(t) | \psi_m^a(t) \rangle_f = \delta_{n,m}$. We also assume that the carrier frequency of an address photon coincides with the frequency of the front cavity mode \hat{a}_d . Thus, the initial state before addressing is $|\Psi_{\text{in}}\rangle = |\Psi^a\rangle_f | \text{qRAM}_2 \rangle$.

We run the rephasing of the coherences in atomic ensemble by inverting the frequency detuning of each atom $\Delta_j \rightarrow -\Delta_j$ as is depicted in Fig. 6.5. Before the recovery of the first atomic coherence at the time $t \approx t_1$ we also map the first addressing wave packet ($n = 1$:

$1 \leq n \leq M$) on the superposition of the atomic states $|g_c\rangle$ and $|au_c\rangle$ via Raman transition with the help of control field $\Omega_0(t - t_1)$ as it is sketched in Fig. 6.5:

$$|\Psi_{\text{in}}\rangle \rightarrow |\Psi_1\rangle = |0\rangle_{\text{out},f} \prod_{m=1}^M |D_m\rangle \left(|g_c\rangle \sum_{n=2}^M \alpha_n |\psi_n^a\rangle_f - \alpha_1 |au_c\rangle |0\rangle_f \right), \quad (6.33)$$

where $|0\rangle_{\text{out},f}$ denotes the vacuum state of the output light field modes.

In particular, the highly efficient mapping of the addressed photon wave packet on the control atom state $|au_c\rangle$ is possible for an exponentially rising shape $g(-t)$ [11] of the photon wavepacket. The exponential shape $g(t)$ corresponds to the typical photon irradiation of a single two-level emitter. To prevent the leakage of the address photon into the QM atomic ensemble we use the second front cavity mode \hat{a}_d for the off-resonant coherent population transfer, as it is depicted in Figure 6.5A and Figure 6.5B. Herein, the address photon wave packet is coupled with the control atom state $|au_c\rangle$ due to the Raman interaction via excited optical state $|a_c\rangle$ in the presence of laser control field $\Omega(t)$.

The atomic rephasing will lead to the transfer of the 1-st atomic state $|D_1\rangle$ into the freely propagating photon wave packet or return back to phase shifted atomic state in the case of the atomic blockade. These two alternatives of the qRAM operation happen in accordance with earlier analysis of the two basic regimes (1-st or 2-nd) determined by two control atom states ($|g_c\rangle$ or $|au_c\rangle$). Eventually these two quantum alternatives lead to the following transformation of the initial state $|\Psi_1\rangle$ after the rephasing of the first atomic coherence and retrieval of the first qubit into the free space photon modes:

$$|\Psi_1\rangle \rightarrow |\Psi_2\rangle = \prod_{m=2}^M |D_m\rangle \{ \alpha_1 |au_c\rangle |\emptyset_1\rangle |\psi_{\text{in},1}\rangle_f + |g_c\rangle |D_1\rangle |0\rangle_{\text{out},f} \sum_{n=2}^M \alpha_n |\psi_n^a\rangle_f \}. \quad (6.34)$$

Next we return the control atom from the state $|au_c\rangle$ to the initial state $|g_c\rangle$ through the retrieval of the first time-bin photon wave packet by way of applying an additional laser

pulse on the transition $|au_c\rangle \rightarrow |a_c\rangle$ (see Figure 6.5). This transfer leads to the following transition

$$\begin{aligned} |\Psi_2\rangle \rightarrow |\Psi_3\rangle = & \prod_{m=2}^M |D_m\rangle |g_c\rangle \{-\alpha_1 |\emptyset_1\rangle |\psi_1^a\rangle_f |\psi_{in,1}\rangle_f \\ & + |D_1\rangle |0\rangle_{out,f} \sum_{n=2}^M \alpha_n |\psi_n^a\rangle_f\}. \end{aligned} \quad (6.35)$$

As it is seen in Eq. 6.35, the irradiation of the first addressing photon component and first qubit are correlated. We repeat this process one by one for the second and all others $M - 2$ time-bin addressing wave packets what leads to the following final state:

$$|\Psi_{in}\rangle \xrightarrow{\text{qRAM}} |\Psi_{out}\rangle = -|g_c\rangle \sum_n^M \alpha_n |\psi_n^a\rangle_f |\psi_{in,n}\rangle_f |\emptyset_n\rangle \prod_{m \neq n}^M |D_m\rangle. \quad (6.36)$$

The final state 6.36 is the result of the pure unitary evolution leading to the quantum superposition of M two-photon states - $|\psi_n^a\rangle_f, |\psi_{in,n}\rangle_f$ with amplitudes α_n determined by the addressing state accomplishing the qRAM operation on the multi-qubit QM cell. We note that other $(M - 1)$ stored qubits $|D_m\rangle$ also become entangled with the irradiated two photon qubits. The performed analysis is valid for an arbitrary quantum state 6.26 stored in the QM atoms. Eq. (6.36) describes the implementation of qRAM operation [207, 208, 209] in the scheme of impedance matching photon echo QM controlled by a single four-level atom.

6.4 Possible experimental implementations

Nowadays implementation of the proposed qRAM in the circuit and nano-optical schemes seems feasible. All the basic hardware elements for the proposed qRAM design are already under active development in the circuit QED. These are systems of two coupled cavities with quantum emitters [229], the multi-qubit echo memory of the spin ensemble in the cavity [221, 222, 223, 224], the coherent population transfer of the single artificial atom [230, 231, 232].

The technique of the multi-time-bin photon generation, which was successfully demonstrated in the cavity QED [233], can be also applied in microwave domain [230, 234]. For the optical domain there are several potential candidates: quantum dots (QD) in coupled photonic crystal nano-cavities [235], nanofibers coupled to cavities with solid-state emitters (like NV centers in diamond, QD, rare-earth ions doped crystals) [236], or natural atoms [237, 238]. The photon state (6.30) can be prepared by linear optics, photon echo QM technique [239], by the Raman quantum memory [240], or by the stimulated rapid adiabatic passage, that has been successfully demonstrated to have a high efficiency [233].

It is worth noting that an efficient qRAM implementation requires further improvement of the quantum transistor protocol based on a single atom in a cavity. Various developing protocols of photon routing [241] can be applied for better photon addressing. The passive routing [242, 243, 238], which does not require any control fields, seems especially promising. Finally, we note that the proposed time-bin qRAM can be also developed for off-resonant Raman atomic transitions that will provide direct quantum storage on a long-lived atomic transition.

6.5 Conclusion

We have proposed the time-bin qRAM based on the single multi-qubit QM cell. The qRAM scheme contains two coupled cavities along with a control four-level atom and the QM resonant atomic ensemble. The multimodality is achieved by combining the time-domain control of the single four-level atom in the front cavity together with the photon echo multi-qubit QM. For the qRAM control we have used the multi-time bin single photon state to perform the quantum addressing without binary tree bifurcation trip inherent to the “bucket-brigade” architecture [207, 208, 209]. This single photon state puts the control atom in the superposition of the transfer and blockade regimes thereby providing a selective readout of the photonic qubits stored in the QM cell. Herein, the qRAM can be principally realized

without “bucket-brigade” architecture by using the proposed quantum control of single multi-qubit QM unit. This technique avoids the complex control on many single-qubit QM cells that previously seems to be difficult for implementation.

We have found a series of impedance matching conditions on the physical parameters of the qRAM scheme. Fulfillment of these conditions provides the broadband and efficient implementation of the studied processes. The maximal efficiency of the qRAM is achieved when the cooperativity parameter of the excited photonic molecule equals to unity and this can be experimentally realized. The performed analysis can be extended to various options of the photon echo QM protocols in the impedance matching cavities. The proposed qRAM can be implemented with current circuit and cavity QED technologies. Moreover, our scheme is suitable for superconducting quantum computing and optical quantum communications.

Chapter 7

Conclusion and discussion

Here we summarize the main results of the dissertation. In Chapter 1, we give a review and outlook of different approaches to quantum memory. We present the physical principles of all main atomic ensemble-based protocols. By introducing the memory performance criteria and compare existing protocols to each other and show their benefits and drawbacks in the context of application to quantum repeaters.

In Chapter 2, we present the necessary mathematical framework for the description of the memory operation.

In Chapter 3, we present a proposed scheme for quantum memory based on a chirped ring-cavity array. The scheme resembles the idea of the echo in AFC, where the role of individual atomic ensembles with a given frequency is played by an array of cavities. The equidistant spectral spacing of the cavities produces constructive interference for the input pulse after the delay inversely proportional to the frequency spacing between the cavities. The presence of the common waveguide allows to reach optimal coupling for converting the input wavepacket into the the cavity array excitation at the finite coupling constant. We compare the CRC memory to the existing coupled integrated spaced sequence of resonators (SCISSOR) and show the supremacy of the CRC scheme in terms of delay time for a given efficiency and lower coupling constant. The more elaborated non-uniform coupling of the

cavities allows to substantially decrease the number of required cavities and open the avenue for the efficient on-chip integrated memory [155].

In Chapter 4 we present the scheme for the extending the bandwidth of the impedance matched Raman memory. The Raman interaction allows to map the light into the extremely long lived ground state nuclear spin coherence of rare-earth ions. Unfortunately, the narrow bandwidth of the Raman resonance allows operation only with long pulses at reasonable parameters of the media. The proposed way to increase the bandwidth of the memory is to use an additional dispersion, which extends the spectral zone of zero round trip phase accumulation inside the cavity. The additional media compensates the cavity dispersion by its refractive index, the similar effect is used for realization of the white light cavity. Next we considered the memory unit to be Λ atomic media inside the impedance matched cavity settings, the additional dispersion is implemented by an extra detuned ensemble of Λ unit driven by a strong pump, which acts as a Raman amplifier. The resulted enhancement of 90 % bandwidth ranges from 2 to 12 fold increase for single to phase modulated pump. An experimental implementation is discussed with Erbium ions doped in yttrium silicate crystal host, which promises the potential to store the light on second time scale. The modeling of the scheme with experimentally feasible parameters shows the promises of achieving delay-bandwidth product on the order of $10^7 - 10^8$ with telecom compatible material. An extra noise introduced by the additional Λ scheme can be as low as 10^{-3} photons per pulse.

In Chapter 5 we present the results on the noise analysis of the GEM implemented with warm rubidium 87 vapour. The memory performance was experimentally evaluated by optical homodyne tomography. The observed noise of 0.1 to 0.3 photons per pulse was attributed to Raman scattering of the spurious population on the level intended for storage. This population appears as a result of the simultaneous action of the control field on both transitions. The developed theoretical model demonstrates a good match with the experimental data. The following analysis of the atomic Clebsch-Gordan coefficients showed, that the different choice of the Λ scheme may decrease the noise by an order of magnitude while keeping an

existing high efficiency. Employing the mentioned noise minimization may open an avenue for realizing simple noise-free efficient quantum memory in a warm vapor.

In Chapter 6 we proposed the new scheme for the quantum random access memory. In contrast to usual quantum memory, the quantum random access can provide the read out of the quantum data in superposition defined by the quantum register. The proposed scheme is based on the atomic ensemble and single atom suited in the coupled cavities. The atomic ensemble plays the role of the memory and allows to store multiple time bin qubits, while a single atom in the strong coupling regime controls the read out from the memory. The mapping of the single photon distributed by the multiple time bins correspondingly to the recorded data allows to put the control atom in to the superposition of two states for all the recorded data independently. In turn, the single atom has two ground state, one is in resonance with cavity and the other is not. While in the resonance the atom blocks the light from entering the second cavity. Therefore the recalled light state from the memory depends on the state of atom, if the atom is in one state the light is recalled, otherwise it is returned into the memory. It was shown, that the proposed design is capable of operating as quantum random access memory with constant scaling with number of used qubits. The optimal physical parameters were presented.

The results presented in the thesis have a broad impact on development of quantum memory. The results can be used for implementation of the quantum memory for quantum repeater and beyond.

Bibliography

- [1] H.-J. Briegel, W. Dür, J. I. Cirac, and P. Zoller. Quantum repeaters: The role of imperfect local operations in quantum communication. *Phys. Rev. Lett.*, 81:5932–5935, 1998.
- [2] Michael A Nielsen and Isaac L Chuang. *Quantum computation and quantum information*. Cambridge university press, 2010.
- [3] Nicolas Sangouard, Christoph Simon, Hugues de Riedmatten, and Nicolas Gisin. Quantum repeaters based on atomic ensembles and linear optics. *Rev. Mod. Phys.*, 83:33–80, Mar 2011.
- [4] M. Razavi, M. Piani, and N. Lütkenhaus. Quantum repeaters with imperfect memories: Cost and scalability. *Physical Review A*, 80(3):032301, sep 2009.
- [5] Sreraman Muralidharan, Linshu Li, Jungsang Kim, Norbert Lütkenhaus, Mikhail D. Lukin, and Liang Jiang. Optimal architectures for long distance quantum communication. *Scientific Reports*, 6(1):20463, Feb 2016.
- [6] L.-M. Duan, M. D. Lukin, J. Ignacio Cirac, and P. Zoller. Long-distance quantum communication with atomic ensembles and linear optics. *Nature*, 414(6862):413–418, Nov 2001.

- [7] Haruka Tanji, Saikat Ghosh, Jonathan Simon, Benjamin Bloom, and Vladan Vuletić. Heralded Single-Magnon Quantum Memory for Photon Polarization States. *Physical Review Letters*, 103(4):043601, jul 2009.
- [8] Boris Albrecht, Pau Farrera, Georg Heinze, Matteo Cristiani, and Hugues de Riedmaten. Controlled rephasing of single collective spin excitations in a cold atomic quantum memory. *Phys. Rev. Lett.*, 115:160501, Oct 2015.
- [9] Yunfei Pu, Yukai Wu, Nan Jiang, Wei Chang, Chang Li, Sheng Zhang, and Lum-ing Duan. Experimental entanglement of 25 individually accessible atomic quantum interfaces. *Sci. Adv.*, 4(4):eaar3931, 2018.
- [10] M. Fleischhauer and M. D. Lukin. Quantum memory for photons: Dark-state polaritons. *Phys. Rev. A*, 65:022314, Jan 2002.
- [11] Alexey V. Gorshkov, Axel André, Michael Fleischhauer, Anders S. Sørensen, and Mikhail D. Lukin. Universal approach to optimal photon storage in atomic media. *Phys. Rev. Lett.*, 98:123601, Mar 2007.
- [12] Alexey V. Gorshkov, Axel André, Mikhail D. Lukin, and Anders S. Sørensen. Photon storage in Λ -type optically dense atomic media. ii. free-space model. *Phys. Rev. A*, 76:033805, Sep 2007.
- [13] A. E. Kozhekin, K. Mølmer, and E. Polzik. Quantum memory for light. *Phys. Rev. A*, 62:033809, Aug 2000.
- [14] J. Nunn, I. A. Walmsley, M. G. Raymer, K. Surmacz, F. C. Waldermann, Z. Wang, and D. Jaksch. Mapping broadband single-photon wave packets into an atomic memory. *Phys. Rev. A*, 75:011401, Jan 2007.
- [15] M. O. Scully and S. M. Zubairy. *Quantum Optics*. Cambridge Univ. Press, 1997.

- [16] J. Nunn, K. Reim, K. C. Lee, V. O. Lorenz, B. J. Sussman, I. A. Walmsley, and D. Jaksch. Multimode memories in atomic ensembles. *Phys. Rev. Lett.*, 101:260502, 2008.
- [17] K. Tikhonov, K. Samburskaya, T. Golubeva, and Yu. Golubev. Storage and retrieval of squeezing in multimode resonant quantum memories. *Phys. Rev. A*, 89:013811, Jan 2014.
- [18] T. Golubeva, Yu. Golubev, O. Mishina, A. Bramati, J. Laurat, and E. Giacobino. High-speed spatially multimode atomic memory. *Phys. Rev. A*, 83:053810, May 2011.
- [19] T Golubeva, Y M Golubev, O Mishina, A Bramati, J Laurat, and E Giacobino. High speed spatially multimode Λ -type atomic memory with arbitrary frequency detuning. *The European Physical Journal D*, 66(10):275, 2012.
- [20] Erhan Saglamyurek, Taras Hrushevskyi, Anindya Rastogi, Khabat Heshami, and Lindsay J LeBlanc. Coherent storage and manipulation of broadband photons via dynamically controlled Autler–Townes splitting. *Nature Photonics*, 12(12):774–782, 2018.
- [21] Erhan Saglamyurek, Taras Hrushevskyi, Logan Cooke, Anindya Rastogi, and Lindsay J. LeBlanc. Single-photon-level light storage in cold atoms using the autler-townes splitting protocol. *Phys. Rev. Research*, 1:022004, Sep 2019.
- [22] Thomas W Mossberg. Time-domain frequency-selective optical data storage. *Optics Letters*, 7(2):77–79, 1982.
- [23] E. L. Hahn. Spin echoes. *Phys. Rev.*, 80:580–594, Nov 1950.
- [24] N. A. Kurnit, I. D. Abella, and S. R. Hartmann. Observation of a photon echo. *Phys. Rev. Lett.*, 13:567–568, Nov 1964.

- [25] N. Christensson, T. Polivka, A. Yartsev, and T. Pullerits. Photon echo spectroscopy reveals structure-dynamics relationships in carotenoids. *Phys. Rev. B*, 79:245118, Jun 2009.
- [26] Lap Van Dao, Craig Lincoln, Martin Lowe, and Peter Hannaford. Spectrally resolved two-colour three-pulse photon echo studies of vibrational dynamics of molecules. *Physica B: Condensed Matter*, 327(1):123 – 128, 2003.
- [27] Igor Osad’ko. *Selective spectroscopy of single molecules*, volume 69. Springer Science & Business Media, 2013.
- [28] VA Zuikov, VV Samartsev, and RG Usmanov. Correlation of the shape of light echo signals with the shape of the excitation pulses. *JETP Letters*, 32:270–274, 1980.
- [29] Masaharu Mitsunaga, Ryuzi Yano, and Naoshi Uesugi. Time- and frequency-domain hybrid optical memory: 1.6-kbit data storage in eu3+:y2sio5. *Opt. Lett.*, 16(23):1890–1892, Dec 1991.
- [30] V. V. Samartsev. Coherent optical spectroscopy of promising materials for solid-state optical processors. *Laser Physics*, 20(2):383–446, 2010.
- [31] S. A. Moiseev and S. Kröll. Complete reconstruction of the quantum state of a single-photon wave packet absorbed by a doppler-broadened transition. *Phys. Rev. Lett.*, 87:173601, 2001.
- [32] Jérôme Ruggiero, Jean-Louis Le Gouët, Christoph Simon, and Thierry Chanelière. Why the two-pulse photon echo is not a good quantum memory protocol. *Phys. Rev. A*, 79:053851, May 2009.
- [33] Daniel F. Walls and Gerard J. Milburn. *Quantum Optics*. Springer Science & Business Media, 2007.

- [34] B. Kraus, W. Tittel, N. Gisin, M. Nilsson, S. Kröll, and J. I. Cirac. Quantum memory for nonstationary light fields based on controlled reversible inhomogeneous broadening. *Phys. Rev. A*, 73:020302, 2006.
- [35] G. Hétet, J. J. Longdell, A. L. Alexander, P. K. Lam, and M. J. Sellars. Electro-optic quantum memory for light using two-level atoms. *Phys. Rev. Lett.*, 100:023601, Jan 2008.
- [36] S. A. Moiseev and N. M. Arslanov. Efficiency and fidelity of photon-echo quantum memory in an atomic system with longitudinal inhomogeneous broadening. *Phys. Rev. A*, 78:023803, 2008.
- [37] G. Hétet, A. Peng, M. T. Johnsson, J. J. Hope, and P. K. Lam. Characterization of electromagnetically-induced-transparency-based continuous-variable quantum memories. *Phys. Rev. A*, 77:012323, Jan 2008.
- [38] S. A. Moiseev and W. Tittel. Optical quantum memory with generalized time-reversible atom–light interaction. *New Journal of Physics*, 13(6):063035, 2011.
- [39] M. Hosseini, B. M. Sparkes, G. Campbell, P. K. Lam, and B. C. Buchler. High efficiency coherent optical memory with warm rubidium vapour. *Nat. Commun.*, 2:174, Feb 2011.
- [40] Mikael Afzelius, Christoph Simon, Hugues de Riedmatten, and Nicolas Gisin. Multi-mode quantum memory based on atomic frequency combs. *Phys. Rev. A*, 79:052329, May 2009.
- [41] A Amari, A Walther, M Sabooni, M Huang, S Kröll, M Afzelius, I Usmani, B Lauritzen, N Sangouard, H de Riedmatten, and N Gisin. Towards an efficient atomic frequency comb quantum memory. *Journal of Luminescence*, 130(9):1579–1585, 2010.
- [42] Erhan Saglamyurek, Neil Sinclair, Jeongwan Jin, Joshua A. Slater, Daniel Oblak, Felix Bussieres, Mathew George, Raimund Ricken, Wolfgang Sohler, and Wolfgang Tittel.

- Broadband waveguide quantum memory for entangled photons. *Nature*, 469(7331):512–515, 2011.
- [43] M. Bonarota, J.-L. Le Gouët, and T Chanelière. Highly multimode storage in a crystal. *New Journal of Physics*, 13(1):013013, 2011.
- [44] Sergey A. Moiseev. Photon-echo quantum memory with complete use of natural inhomogeneous broadening. *Phys. Rev. A*, 83:012307, 2011.
- [45] V. Damon, M. Bonarota, A. Louchet-Chauvet, T. Chanelière, and J-L Le Gouët. Revival of silenced echo and quantum memory for light. *New Journal of Physics*, 13(9):093031, 2011.
- [46] D. L. McAuslan, P. M. Ledingham, W. R. Naylor, S. E. Beavan, M. P. Hedges, M. J. Sellars, and J. J. Longdell. Photon-echo quantum memories in inhomogeneously broadened two-level atoms. *Phys. Rev. A*, 84:022309, Aug 2011.
- [47] Julián Dajczgewand, Jean-Louis Le Gouët, Anne Louchet-Chauvet, and Thierry Chanelière. Large efficiency at telecom wavelength for optical quantum memories. *Opt. Lett.*, 39(9):2711–2714, May 2014.
- [48] Herbert Walther, Benjamin T H Varcoe, Berthold-Georg Englert, and Thomas Becker. Cavity quantum electrodynamics. *Reports on Progress in Physics*, 69(5):1325–1382, apr 2006.
- [49] Alexey V. Gorshkov, Axel André, Mikhail D. Lukin, and Anders S. Sørensen. Photon storage in Λ -type optically dense atomic media. i. cavity model. *Phys. Rev. A*, 76:033804, Sep 2007.
- [50] S. A. Moiseev and W. Tittel. Temporal compression of quantum-information-carrying photons using a photon-echo quantum memory approach. *Phys. Rev. A*, 82:012309, 2010.

- [51] C. Simon, M. Afzelius, J. Appel, A. Boyer de la Giroday, S. J. Dewhurst, N. Gisin, C. Y. Hu, F. Jelezko, S. Kröll, J. H. Müller, J. Nunn, E. S. Polzik, J. G. Rarity, H. De Riedmatten, W. Rosenfeld, A. J. Shields, N. Sköld, R. M. Stevenson, R. Thew, I. A. Walmsley, M. C. Weber, H. Weinfurter, J. Wrachtrup, and R. J. Young. Quantum memories. *The European Physical Journal D*, 58(1):1–22, 2010.
- [52] Alexander I. Lvovsky, Barry C. Sanders, and Wolfgang Tittel. Optical quantum memory. *Nat. Photonics*, 3(12):706–714, 2009.
- [53] Pieter Kok and Brendon W. Lovett. *Introduction to Optical Quantum Information Processing*. Cambridge University Press, 2010.
- [54] Samuel L. Braunstein and Peter van Loock. Quantum information with continuous variables. *Rev. Mod. Phys.*, 77:513–577, Jun 2005.
- [55] Frédéric Grosshans and Philippe Grangier. Quantum cloning and teleportation criteria for continuous quantum variables. *Phys. Rev. A*, 64:010301, Jun 2001.
- [56] Or Katz and Ofer Firstenberg. Light storage for one second in room-temperature alkali vapor. *Nature Communications*, 9(1):2074, 2018.
- [57] M. V. Balabas, T. Karaulanov, M. P. Ledbetter, and D. Budker. Polarized alkali-metal vapor with minute-long transverse spin-relaxation time. *Phys. Rev. Lett.*, 105:070801, Aug 2010.
- [58] Y. O. Dudin, L. Li, and A. Kuzmich. Light storage on the time scale of a minute. *Phys. Rev. A*, 87:031801, Mar 2013.
- [59] Georg Heinze, Christian Hubrich, and Thomas Halfmann. Stopped light and image storage by electromagnetically induced transparency up to the regime of one minute. *Phys. Rev. Lett.*, 111:033601, Jul 2013.

- [60] Manjin Zhong, Morgan P Hedges, Rose L Ahlefeldt, John G Bartholomew, Sarah E Beavan, Sven M Wittig, Jevon J Longdell, and Matthew J Sellars. Optically addressable nuclear spins in a solid with a six-hour coherence time. *Nature*, 517(7533):177, 2015.
- [61] Christoph Simon, Hugues de Riedmatten, Mikael Afzelius, Nicolas Sangouard, Hugo Zbinden, and Nicolas Gisin. Quantum repeaters with photon pair sources and multi-mode memories. *Phys. Rev. Lett.*, 98:190503, May 2007.
- [62] Yunfei Pu, Yukai Wu, Nan Jiang, Wei Chang, Chang Li, Sheng Zhang, and Luming Duan. Experimental entanglement of 25 individually accessible atomic quantum interfaces. *Science Advances*, 4(4), 2018.
- [63] Radoslaw Chrapkiewicz, Michal Dkabrowski, and Wojciech Wasilewski. High-capacity angularly multiplexed holographic memory operating at the single-photon level. *Phys. Rev. Lett.*, 118:063603, Feb 2017.
- [64] Cyril Laplane, Pierre Jobez, Jean Etesse, Nuala Timoney, Nicolas Gisin, and Mikael Afzelius. Multiplexed on-demand storage of polarization qubits in a crystal. *New Journal of Physics*, 18(1):013006, dec 2015.
- [65] Yafei Wen, Pai Zhou, Zhongxiao Xu, Liang Yuan, Minjie Wang, Shengzhi Wang, Lirong Chen, and Hai Wang. Cavity-enhanced and long-lived optical memories for two orthogonal polarizations in cold atoms. *Opt. Express*, 28(1):360–368, Jan 2020.
- [66] K. F. Reim, J. Nunn, V. O. Lorenz, B. J. Sussman, K. C. Lee, N. K. Langford, D. Jaksch, and I. A. Walmsley. Towards high-speed optical quantum memories. *Nature Photonics*, 4:218 EP –, Mar 2010.
- [67] Khabat Heshami, Duncan G. England, Peter C. Humphreys, Philip J. Bustard, Victor M. Acosta, Joshua Nunn, and Benjamin J. Sussman. Quantum memories: emerging applications and recent advances. *Journal of Modern Optics*, 63(20):2005–2028, 2016.

- [68] Nicolas Sangouard, Christoph Simon, Hugues De Riedmatten, and Nicolas Gisin. Quantum repeaters based on atomic ensembles and linear optics. *Reviews of Modern Physics*, 83(1):33, 2011.
- [69] M. A. Nielsen and I. L. Chuang. *Quantum Computation and Quantum Information*. Cambridge Univ. Press, 2000.
- [70] A. Furusawa, J. L. Sørensen, S. L. Braunstein, C. A. Fuchs, H. J. Kimble, and E. S. Polzik. Unconditional quantum teleportation. *Science*, 282(5389):706–709, 1998.
- [71] Ya-Fen Hsiao, Pin-Ju Tsai, Hung-Shiue Chen, Sheng-Xiang Lin, Chih-Chiao Hung, Chih-Hsi Lee, Yi-Hsin Chen, Yong-Fan Chen, Ite A Yu, and Ying-Cheng Chen. Highly Efficient Coherent Optical Memory Based on Electromagnetically Induced Transparency. *Phys. Rev. Lett.*, 120(18):183602, may 2018.
- [72] Sergey. A. Moiseev and J.-L. Le Gouët. Rephasing processes and quantum memory for light: reversibility issues and how to fix them. *Journal of Physics B: Atomic, Molecular and Optical Physics*, 45(12):124003, 2012.
- [73] Mahmood Sabooni, Qian Li, Stefan Kröll, and Lars Rippe. Efficient quantum memory using a weakly absorbing sample. *Phys. Rev. Lett.*, 110:133604, Mar 2013.
- [74] P Jobez, I Usmani, N Timoney, C Laplane, N Gisin, and M Afzelius. Cavity-enhanced storage in an optical spin-wave memory. *New Journal of Physics*, 16(8):83005, 2014.
- [75] Tian Zhong, Jonathan M Kindem, John G Bartholomew, Jake Rochman, Ioana Craiciu, Evan Miyazono, Marco Bettinelli, Enrico Cavalli, Varun Verma, Sae Woo Nam, Francesco Marsili, Matthew D Shaw, Andrew D Beyer, and Andrei Faraon. Nanophotonic rare-earth quantum memory with optically controlled retrieval. *Science*, 357(6358):1392–1395, 2017.

- [76] Jinxian Guo, Xiaotian Feng, Peiyu Yang, Zhifei Yu, L Q Chen, Chun-Hua Yuan, and Weiping Zhang. High-performance Raman quantum memory with optimal control in room temperature atoms. *Nature Communications*, 10(1):148, 2019.
- [77] Erwan Bimbard, Rajiv Boddeda, Nicolas Vitrant, Andrey Grankin, Valentina Parigi, Jovica Stanojevic, Alexei Ourjoumtsev, and Philippe Grangier. Homodyne tomography of a single photon retrieved on demand from a cavity-enhanced cold atom memory. *Phys. Rev. Lett.*, 112:033601, Jan 2014.
- [78] A. Kuzmich, W. P. Bowen, A. D. Boozer, A. Boca, C. W. Chou, L.-M. Duan, and H. J. Kimble. Generation of nonclassical photon pairs for scalable quantum communication with atomic ensembles. *Nature*, 423(6941):731–734, Jun 2003.
- [79] T Chanelière, D N Matsukevich, S D Jenkins, S.-Y. Lan, T A B Kennedy, and A Kuzmich. Storage and retrieval of single photons transmitted between remote quantum memories. *Nature*, 438(7069):833–836, 2005.
- [80] M D Eisaman, A André, F Massou, M Fleischhauer, A S Zibrov, and M D Lukin. Electromagnetically induced transparency with tunable single-photon pulses. *Nature*, 438(7069):837–841, 2005.
- [81] Jürgen Appel, Eden Figueroa, Dmitry Korystov, M. Lobino, and A. I. Lvovsky. Quantum Memory for Squeezed Light. *Physical Review Letters*, 100(9):093602, mar 2008.
- [82] M. Lobino, C. Kupchak, E. Figueroa, and A. I. Lvovsky. Memory for Light as a Quantum Process. *Physical Review Letters*, 102(20):203601, may 2009.
- [83] Daniel Rieländer, Kutlu Kutluer, Patrick M. Ledingham, Mustafa Gündoğan, Julia Fekete, Margherita Mazzera, and Hugues de Riedmatten. Quantum storage of heralded single photons in a praseodymium-doped crystal. *Phys. Rev. Lett.*, 112:040504, Jan 2014.

- [84] Erhan Saglamyurek, Jeongwan Jin, Varun B Verma, Matthew D Shaw, Francesco Marsili, Sae Woo Nam, Daniel Oblak, and Wolfgang Tittel. Quantum storage of entangled telecom-wavelength photons in an erbium-doped optical fibre. *Nature Photonics*, 9(2):83–87, 2015.
- [85] Nathaniel B. Phillips, Alexey V. Gorshkov, and Irina Novikova. Light storage in an optically thick atomic ensemble under conditions of electromagnetically induced transparency and four-wave mixing. *Physical Review A*, 83(6):063823, jun 2011.
- [86] Nikolai Lauk, Christopher O’Brien, and Michael Fleischhauer. Fidelity of photon propagation in electromagnetically induced transparency in the presence of four-wave mixing. *Phys. Rev. A*, 88:013823, Jul 2013.
- [87] R. L. Ahlefeldt, M. R. Hush, and M. J. Sellars. Ultranarrow optical inhomogeneous linewidth in a stoichiometric rare-earth crystal. *Phys. Rev. Lett.*, 117:250504, Dec 2016.
- [88] Mattias Nilsson, Lars Rippe, Stefan Kröll, Robert Klieber, and Dieter Suter. Hole-burning techniques for isolation and study of individual hyperfine transitions in inhomogeneously broadened solids demonstrated in $\text{pr}^{3+}:\text{Y}_2\text{SiO}_5$. *Phys. Rev. B*, 70:214116, Dec 2004.
- [89] A. Amari, A. Walther, M. Sabooni, M. Huang, S. Kröll, M. Afzelius, I. Usmani, B. Lauritzen, N. Sangouard, H. De Riedmatten, and N. Gisin. Towards an efficient atomic frequency comb quantum memory. *J. Lumin.*, 130(9):1579–1585, 2010.
- [90] Carlo Ottaviani, Christoph Simon, Hugues de Riedmatten, Mikael Afzelius, Björn Lauritzen, Nicolas Sangouard, and Nicolas Gisin. Creating single collective atomic excitations via spontaneous Raman emission in inhomogeneously broadened systems: Beyond the adiabatic approximation. *Physical Review A*, 79(6):063828, jun 2009.

- [91] R. Zhao, Y. O. Dudin, S. D. Jenkins, C. J. Campbell, D. N. Matsukevich, T. A. B. Kennedy, and A. Kuzmich. Long-lived quantum memory. *Nat. Phys.*, 5:100–104, Dec 2008.
- [92] Sheng-Jun Yang, Xu-Jie Wang, Xiao-Hui Bao, and Jian-Wei Pan. An efficient quantum light–matter interface with sub-second lifetime. *Nat. Photonics*, 10(6):381, Apr 2016.
- [93] A. G. Radnaev, Y. O. Dudin, R. Zhao, H. H. Jen, S. D. Jenkins, A. Kuzmich, and T. A. B. Kennedy. A quantum memory with telecom-wavelength conversion. *Nat. Phys.*, 6:894–899, Sep 2010.
- [94] Adrian Holzäpfel, Jean Etesse, Krzysztof T Kaczmarek, Alexey Tiranov, Nicolas Gisin, and Mikael Afzelius. Optical storage on the timescale of a second in a solid-state atomic frequency comb memory using dynamical decoupling. *arXiv preprint arXiv:1910.08009*, 2019.
- [95] J. J. Longdell, E. Fraval, M. J. Sellars, and N. B. Manson. Stopped Light with Storage Times Greater than One Second Using Electromagnetically Induced Transparency in a Solid. *Physical Review Letters*, 95(6):063601, aug 2005.
- [96] U. Schnorrberger, J. D. Thompson, S. Trotzky, R. Pugatch, N. Davidson, S. Kuhr, and I. Bloch. Electromagnetically Induced Transparency and Light Storage in an Atomic Mott Insulator. *Physical Review Letters*, 103(3):033003, jul 2009.
- [97] Or Katz and Ofer Firstenberg. Light storage for one second in room-temperature alkali vapor. *Nature communications*, 9(1):2074, 2018.
- [98] Miloš Rancic, Morgan P. Hedges, Rose L. Ahlefeldt, and Matthew J. Sellars. Coherence time of over a second in a telecom-compatible quantum memory storage material. *Nature Physics*, 14(1), 2018.

- [99] Emmanuel Zambrini Cruzeiro, Florian Fröwis, Nuala Timoney, and Mikael Afzelius. Noise in optical quantum memories based on dynamical decoupling of spin states. *Journal of Modern Optics*, 63(20):2101–2113, 2016.
- [100] K. Boone, J.-P. Bourgoin, E. Meyer-Scott, K. Heshami, T. Jennewein, and C. Simon. Entanglement over global distances via quantum repeaters with satellite links. *Physical Review A*, 91(5):052325, may 2015.
- [101] Tian-Shu Yang, Zong-Quan Zhou, Yi-Lin Hua, Xiao Liu, Zong-Feng Li, Pei-Yun Li, Yu Ma, Chao Liu, Peng-Jun Liang, Xue Li, Yi-Xin Xiao, Jun Hu, Chuan-Feng Li, and Guang-Can Guo. Multiplexed storage and real-time manipulation based on a multiple degree-of-freedom quantum memory. *Nature Communications*, 9(1):3407, 2018.
- [102] D. B. Higginbottom, B. M. Sparkes, M. Rancic, O. Pinel, M. Hosseini, P. K. Lam, and B. C. Buchler. Spatial-mode storage in a gradient-echo memory. *Physical Review A*, 86(2):023801, aug 2012.
- [103] Quentin Glorieux, Jeremy B. Clark, Alberto M. Marino, Zhifan Zhou, and Paul D. Lett. Temporally multiplexed storage of images in a gradient echo memory. *Optics Express*, 20(11):12350, may 2012.
- [104] Rui Zhang, Sean R. Garner, and Lene Vestergaard Hau. Creation of long-term coherent optical memory via controlled nonlinear interactions in bose-einstein condensates. *Phys. Rev. Lett.*, 103:233602, Dec 2009.
- [105] Yunfei Pu, Yukai Wu, Nan Jiang, Wei Chang, Chang Li, Sheng Zhang, and Lum-ing Duan. Experimental entanglement of 25 individually accessible atomic quantum interfaces. *Science advances*, 4(4):eaar3931, 2018.
- [106] Yanfei Tu, Guoquan Zhang, Zhaohui Zhai, and Jingjun Xu. Angular multiplexing storage of light pulses and addressable optical buffer memory in Pr³⁺: Y₂ SiO₅ based

- on electromagnetically induced transparency. *Physical Review A - Atomic, Molecular, and Optical Physics*, 80(3):3–7, 2009.
- [107] Young-Wook Cho and Yoon-Ho Kim. Atomic vapor quantum memory for a photonic polarization qubit. *Optics Express*, 18(25):25786–25793, 2010.
- [108] Radoslaw Chrapkiewicz and Wojciech Wasilewski. Generation and delayed retrieval of spatially multimode Raman scattering in warm rubidium vapors. *Optics Express*, 20(28):29540, dec 2012.
- [109] A Nicolas, L Veissier, L Giner, E Giacobino, D Maxein, and J Laurat. A quantum memory for orbital angular momentum photonic qubits. *Nature Photonics*, 8(3):234–238, 2014.
- [110] Yafei Wen, Pai Zhou, Zhongxiao Xu, Liang Yuan, Minjie Wang, Shengzhi Wang, Lirong Chen, and Hai Wang. Cavity-enhanced and long-lived optical memories for two orthogonal polarizations in cold atoms. *Opt. Express*, 28(1):360–368, jan 2020.
- [111] Kate R. Ferguson, Sarah E. Beavan, Jevon J. Longdell, and Matthew J. Sellars. Generation of light with multimode time-delayed entanglement using storage in a solid-state spin-wave quantum memory. *Phys. Rev. Lett.*, 117:020501, Jul 2016.
- [112] Yafei Wen, Pai Zhou, Zhongxiao Xu, Liang Yuan, Haoyi Zhang, Shengzhi Wang, Long Tian, Shujing Li, and Hai Wang. Multiplexed spin-wave–photon entanglement source using temporal multimode memories and feedforward-controlled readout. *Physical Review A*, 100(1):012342, jul 2019.
- [113] Zhan Zheng, Oxana Mishina, Nicolas Treps, and Claude Fabre. Atomic quantum memory for multimode frequency combs. *Phys. Rev. A*, 91(3):31802, mar 2015.

- [114] Daniel Schraft, Marcel Hain, Nikolaus Lorenz, and Thomas Halfmann. Stopped light at high storage efficiency in a $\text{pr}^{3+} : \text{y}_2\text{sio}_5$ crystal. *Phys. Rev. Lett.*, 116:073602, Feb 2016.
- [115] Rikizo Ikuta, Yoshiaki Kusaka, Tsuyoshi Kitano, Hiroshi Kato, Takashi Yamamoto, Masato Koashi, and Nobuyuki Imoto. Wide-band quantum interface for visible-to-telecommunication wavelength conversion. *Nature Communications*, 2(1):537, 2011.
- [116] Tim van Leent, Matthias Bock, Robert Garthoff, Kai Redeker, Wei Zhang, Tobias Bauer, Wenjamin Rosenfeld, Christoph Becher, and Harald Weinfurter. Long-Distance Distribution of Atom-Photon Entanglement at Telecom Wavelength. *Physical Review Letters*, 124(1):010510, jan 2020.
- [117] Mikhail I. Kolobov. The spatial behavior of nonclassical light. *Rev. Mod. Phys.*, 71:1539–1589, Oct 1999.
- [118] Andrei B. Klimov and Sergei M. Chumakov. *A Group-Theoretical Approach to Quantum Optics: Models of Atom-Field Interactions*. John Wiley & Sons, 2009.
- [119] C. W. Gardiner and M. J. Collett. Input and output in damped quantum systems: Quantum stochastic differential equations and the master equation. *Phys. Rev. A*, 31:3761–3774, Jun 1985.
- [120] N. A. Kurnit, I. D. Abella, and S. R. Hartmann. Observation of a photon echo. *Phys. Rev. Lett.*, 13:567–568, Nov 1964.
- [121] Leslie Allen and Joseph H. Eberly. *Optical resonance and two-level atoms*, volume 28. Courier Corporation, 1987.
- [122] Y. R. Shen. *The Principles of Nonlinear Optics*. John Wiley & Sons, 1984.
- [123] Henrik Stapelfeldt and Tamar Seideman. Colloquium: Aligning molecules with strong laser pulses. *Rev. Mod. Phys.*, 75:543–557, Apr 2003.

- [124] D. Kartashov, S. Haessler, S. Ališauskas, G. Andriukaitis, A. Pugžlys, A. Baltuška, J. Möhring, D. Starukhin, M. Motzkus, A. M. Zheltikov, et al. Research in optical sciences. *OSA Technical Digest (Optical Society of America, 2014)*, paper HTh4B, 5, 2012.
- [125] I. V. Fedotov, A. D. Savvin, A. B. Fedotov, and A. M. Zheltikov. Controlled rotational raman echo recurrences and modulation of high-intensity ultrashort laser pulses by molecular rotations in the gas phase. *Opt. Lett.*, 32(10):1275–1277, May 2007.
- [126] Hugues de Riedmatten, Mikael Afzelius, Matthias U. Staudt, Christoph Simon, and Nicolas Gisin. A solid-state light-matter interface at the single-photon level. *Nature*, 456(7223):773–777, 2008.
- [127] Morgan P. Hedges, Jevon J. Longdell, Yongmin Li, and Matthew J. Sellars. Efficient quantum memory for light. *Nature*, 465(7301):1052–1056, 2010.
- [128] Klemens Hammerer, Anders S. Sørensen, and Eugene S. Polzik. Quantum interface between light and atomic ensembles. *Rev. Mod. Phys.*, 82:1041–1093, Apr 2010.
- [129] W. Tittel, M. Afzelius, T. Chanelière, R.L. Cone, S. Kröll, S.A. Moiseev, and M. Sellars. Photon-echo quantum memory in solid state systems. *Laser & Photonics Reviews*, 4(2):244–267, 2010.
- [130] V Damon, M Bonarota, A Louchet-Chauvet, T Chanelière, and J-L Le Gouët. Revival of silenced echo and quantum memory for light. *New Journal of Physics*, 13(9):093031, sep 2011.
- [131] Mikael Afzelius and Christoph Simon. Impedance-matched cavity quantum memory. *Phys. Rev. A*, 82:022310, Aug 2010.
- [132] VB Braginsky, ML Gorodetsky, and VS Ilchenko. Quality-factor and nonlinear properties of optical whispering-gallery modes. *Physics letters A*, 137(7-8):393–397, 1989.

- [133] M. L. Gorodetsky and V. S. Ilchenko. Optical microsphere resonators: optimal coupling to high-q whispering-gallery modes. *J. Opt. Soc. Am. B*, 16(1):147–154, Jan 1999.
- [134] John Heebner, Rohit Grover, Tarek Ibrahim, and Tarek A Ibrahim. *Optical microresonators: theory, fabrication, and applications*, volume 138. Springer Science & Business Media, 2008.
- [135] John E. Heebner and Robert W. Boyd. Slow and stopped light ‘slow’ and ‘fast’ light in resonator-coupled waveguides. *Journal of Modern Optics*, 49(14-15):2629–2636, 2002.
- [136] John E. Heebner, Robert W. Boyd, and Q-Han Park. Scissor solitons and other novel propagation effects in microresonator-modified waveguides. *J. Opt. Soc. Am. B*, 19(4):722–731, Apr 2002.
- [137] Fengnian Xia, Lidija Sekaric, and Yurii Vlasov. Ultracompact optical buffers on a silicon chip. *Nature photonics*, 1(1):65, 2007.
- [138] Amnon Yariv, Yong Xu, Reginald K. Lee, and Axel Scherer. Coupled-resonator optical waveguide: a proposal and analysis. *Opt. Lett.*, 24(11):711–713, Jun 1999.
- [139] Ioannis Chremmos, Otto Schwelb, and Nikolaos Uzunoglu. *Photonic microresonator research and applications*, volume 156. Springer, 2010.
- [140] Francesco Morichetti, Carlo Ferrari, Antonio Canciamilla, and Andrea Melloni. The first decade of coupled resonator optical waveguides: bringing slow light to applications. *Laser & Photonics Reviews*, 6(1):74–96, 2012.
- [141] Wim Bogaerts, Peter De Heyn, Thomas Van Vaerenbergh, Katrien De Vos, Shankar Kumar Selvaraja, Tom Claes, Pieter Dumon, Peter Bienstman, Dries Van Thourhout, and Roel Baets. Silicon microring resonators. *Laser & Photonics Reviews*, 6(1):47–73, 2012.

- [142] Mingzhen Tian, Devin Vega, and Jacob Dilles. Quantum memory based on a spectroscopic atomic comb. *Phys. Rev. A*, 87:042338, Apr 2013.
- [143] S. A. Moiseev. Off-resonant raman-echo quantum memory for inhomogeneously broadened atoms in a cavity. *Phys. Rev. A*, 88:012304, Jul 2013.
- [144] ES Moiseev and SA Moiseev. Time-bin quantum ram. *Journal of Modern Optics*, 63(20):2081–2092, 2016.
- [145] G Lenz, BJ Eggleton, C Kd Madsen, and RE Slusher. Optical delay lines based on optical filters. *IEEE Journal of Quantum Electronics*, 37(4):525–532, 2001.
- [146] DK Armani, TJ Kippenberg, SM Spillane, and KJ Vahala. Ultra-high-q toroid microcavity on a chip. *Nature*, 421(6926):925, 2003.
- [147] Tobias Herr, Victor Brasch, John D Jost, Christine Y Wang, Nikita M Kondratiev, Michael L Gorodetsky, and Tobias J Kippenberg. Temporal solitons in optical microresonators. *Nature Photonics*, 8(2):145, 2014.
- [148] Andrea Melloni, Antonio Canciamilla, Carlo Ferrari, Francesco Morichetti, L O’Faolain, TF Krauss, Re De La Rue, A Samarelli, and M Sorel. Tunable delay lines in silicon photonics: coupled resonators and photonic crystals, a comparison. *IEEE Photonics Journal*, 2(2):181–194, 2010.
- [149] Antonio Canciamilla, M Torregiani, Carlo Ferrari, Francesco Morichetti, RM De La Rue, A Samarelli, M Sorel, and A Melloni. Silicon coupled-ring resonator structures for slow light applications: potential, impairments and ultimate limits. *Journal of Optics*, 12(10):104008, 2010.
- [150] Gopalakrishnan Balasubramanian, Philipp Neumann, Daniel Twitchen, Matthew Markham, Roman Kolesov, Norikazu Mizuochi, Junichi Isoya, Jocelyn Achard, Jo-

- hannes Beck, Julia Tissler, et al. Ultralong spin coherence time in isotopically engineered diamond. *Nature materials*, 8(5):383, 2009.
- [151] GD Fuchs, Guido Burkard, PV Klimov, and DD Awschalom. A quantum memory intrinsic to single nitrogen–vacancy centres in diamond. *Nature Physics*, 7(10):789, 2011.
- [152] W. L. Yang, Z. Q. Yin, Y. Hu, M. Feng, and J. F. Du. High-fidelity quantum memory using nitrogen-vacancy center ensemble for hybrid quantum computation. *Phys. Rev. A*, 84:010301, Jul 2011.
- [153] Peter Christian Maurer, Georg Kucsko, Christian Latta, Liang Jiang, Norman Ying Yao, Steven D Bennett, Fernando Pastawski, David Hunger, Nicholas Chisholm, Matthew Markham, et al. Room-temperature quantum bit memory exceeding one second. *Science*, 336(6086):1283–1286, 2012.
- [154] AV Tsukanov. Quantum memory based on ensemble states of nv centers in diamond. *Russian Microelectronics*, 42(3):127–147, 2013.
- [155] N. S. Perminov and S. A. Moiseev. Spectral-topological superefficient quantum memory. *Scientific Reports*, 9(1):1568, 2019.
- [156] V. Huet, A. Rasoloniaina, P. Guillemé, P. Rochard, P. Féron, M. Mortier, A. Levenson, K. Bencheikh, A. Yacomotti, and Y. Dumeige. Millisecond photon lifetime in a slow-light microcavity. *Phys. Rev. Lett.*, 116:133902, Mar 2016.
- [157] Yosuke Hashimoto, Takeshi Toyama, Jun-ichi Yoshikawa, Kenzo Makino, Fumiya Okamoto, Rei Sakakibara, Shuntaro Takeda, Peter van Loock, and Akira Furusawa. All-optical storage of phase-sensitive quantum states of light. *Phys. Rev. Lett.*, 123:113603, Sep 2019.

- [158] David Press, Kristiaan De Greve, Peter L. McMahon, Thaddeus D. Ladd, Benedikt Friess, Christian Schneider, Martin Kamp, Sven Höfling, Alfred Forchel, and Yoshihisa Yamamoto. Ultrafast optical spin echo in a single quantum dot. *Nat. Photonics*, 4:367–370, Apr 2010.
- [159] D. D. Sukachev, A. Sipahigil, C. T. Nguyen, M. K. Bhaskar, R. E. Evans, F. Jelezko, and M. D. Lukin. Silicon-vacancy spin qubit in diamond: A quantum memory exceeding 10 ms with single-shot state readout. *Phys. Rev. Lett.*, 119:223602, Nov 2017.
- [160] Duncan G. England, Kent A. G. Fisher, Jean-Philippe W. MacLean, Philip J. Bustard, Rune Lausten, Kevin J. Resch, and Benjamin J. Sussman. Storage and retrieval of THz-bandwidth single photons using a room-temperature diamond quantum memory. *Phys. Rev. Lett.*, 114:053602, Feb 2015.
- [161] G. Heinze, C. Hubrich, and T. Halfmann. Coherence time extension in $\text{Pr}^{3+}:\text{Y}_2\text{SiO}_5$ by self-optimized magnetic fields and dynamical decoupling. *Phys. Rev. A*, 89:053825, May 2014.
- [162] J. I. Cirac, P. Zoller, H. J. Kimble, and H. Mabuchi. Quantum state transfer and entanglement distribution among distant nodes in a quantum network. *Phys. Rev. Lett.*, 78:3221–3224, Apr 1997.
- [163] Norbert Kalb, Andreas Reiserer, Stephan Ritter, and Gerhard Rempe. Heralded storage of a photonic quantum bit in a single atom. *Phys. Rev. Lett.*, 114:220501, Jun 2015.
- [164] A. Wallraff, D. I. Schuster, A. Blais, L. Frunzio, R.-S. Huang, J. Majer, S. Kumar, S. M. Girvin, and R. J. Schoelkopf. Strong coupling of a single photon to a superconducting qubit using circuit quantum electrodynamics. *Nature*, 431:162–197, 2004.

- [165] Stephan Welte, Bastian Hacker, Severin Daiss, Stephan Ritter, and Gerhard Rempe. Photon-mediated quantum gate between two neutral atoms in an optical cavity. *Phys. Rev. X*, 8:011018, Feb 2018.
- [166] R. E. Evans, M. K. Bhaskar, D. D. Sukachev, C. T. Nguyen, A. Sipahigil, M. J. Burek, B. Machielse, G. H. Zhang, A. S. Zibrov, E. Bielejec, H. Park, M. Lončar, and M. D. Lukin. Photon-mediated interactions between quantum emitters in a diamond nanocavity. *Science*, 362(6415):662–665, 2018.
- [167] Chun Xiao Zhou, Rui Zhang, Miao Di Guo, S A Moiseev, and Xue Mei Su. Single photon transfer controlled by excitation phase in a two-atom cavity system. *Journal of Physics B: Atomic, Molecular and Optical Physics*, 50(12):125501, may 2017.
- [168] Alexander I. Lvovsky, Barry C. Sanders, and Wolfgang Tittel. Optical quantum memory. *Nature photonics*, 3(12):706–714, 2009.
- [169] L. Ma, O Slattery, and X. Tang. Optical quantum memory and its applications in quantum communication systems. *J. Res. Natl. Inst. Stan.*, 125:125002, 2020.
- [170] B. M. Sparkes, J. Bernu, M. Hosseini, J. Geng, Q. Glorieux, P. A. Altin, P. K. Lam, N. P. Robins, and B. C. Buchler. Gradient echo memory in an ultra-high optical depth cold atomic ensemble. *New Journal of Physics*, 15(8):085027, 2013.
- [171] M. T. Manzoni, M. Moreno-Cardoner, A. Asenjo-Garcia, J. V. Porto, A. V. Gorshkov, and D. E. Chang. Optimization of photon storage fidelity in ordered atomic arrays. *New Journal of Physics*, 20(8):083048, 2018.
- [172] Mahmood Sabooni, Adam N. Nilsson, Gerhard Kristensson, and Lars Rippe. Wave propagation in birefringent materials with off-axis absorption or gain. *Phys. Rev. A*, 93:013842, Jan 2016.

- [173] Sergey A. Moiseev, Sergey N. Andrianov, and Firdus F. Gubaidullin. Efficient multi-mode quantum memory based on photon echo in an optimal qed cavity. *Phys. Rev. A*, 82:022311, Aug 2010.
- [174] Mahmood Sabooni, Qian Li, Lars Rippe, R. Krishna Mohan, and Stefan Kröll. Spectral engineering of slow light, cavity line narrowing, and pulse compression. *Phys. Rev. Lett.*, 111:183602, Oct 2013.
- [175] M. M. Minnegaliev, E. I. Baibekov, K. I. Gerasimov, S. A. Moiseev, M. A. Smirnov, and R. V. Urmancheev. Photon echo of an ultranarrow optical transition of $^{167}\text{Er}^{3+}$ in $^7\text{LiYF}_4$ crystals. *Quantum Electron.*, 47(9):778–782, 2017.
- [176] E. S. Moiseev and S. A. Moiseev. Time-bin quantum ram. *Journal of Modern Optics*, 63(20):2081–2092, 2016.
- [177] A. Wicht, K. Danzmann, M. Fleischhauer, M. Scully, G. Müller, and R.-H. Rinkleff. White-light cavities, atomic phase coherence, and gravitational wave detectors. *Opt. Comm.*, 134(1):431–439, 1997.
- [178] Warren Nagourney. *Quantum Electronics for Atomic Physics and Telecommunication*. OUP Oxford, 2014.
- [179] E. S. Moiseev and S. A. Moiseev. Scalable time reversal of raman echo quantum memory and quantum waveform conversion of light pulse. *New Journal of Physics*, 15(10):105005, 2013.
- [180] J. Nunn, J. H. D. Munns, S. Thomas, K. T. Kaczmarek, C. Qiu, A. Feizpour, E. Poem, B. Brecht, D. J. Saunders, P. M. Ledingham, Dileep V. Reddy, M. G. Raymer, and I. A. Walmsley. Theory of noise suppression in λ -type quantum memories by means of a cavity. *Phys. Rev. A*, 96:012338, Jul 2017.

- [181] Nikolai Lauk. *Quantum Networks for Photons: Nonlinear Effects in Quantum Memories, Quantum Interfaces and Single-photon Filter*. PhD thesis, Technische Universität Kaiserslautern, 2016.
- [182] Miloš Rančić, Morgan P. Hedges, Rose L. Ahlefeldt, and Matthew J. Sellars. Coherence time of over a second in a telecom-compatible quantum memory storage material. *Nat. Phys.*, 14(1):50–54, 2017.
- [183] Mattias Nilsson, Lars Rippe, Stefan Kröll, Robert Klieber, and Dieter Suter. Hole-burning techniques for isolation and study of individual hyperfine transitions in inhomogeneously broadened solids demonstrated in $\text{pr}^{3+}:\text{Y}_2\text{SiO}_5$. *Phys. Rev. B*, 70:214116, Dec 2004.
- [184] M. Zhong, M. P. Hedges, R. L. Ahlefeldt, J. G. Bartholomew, S. E. Beavan, S. M. Wittig, J. J. Longdell, and M. J. Sellars. Optically addressable nuclear spins in a solid with a six-hour coherence time. *Nature*, 517:177–180, 2015.
- [185] Mattias Nilsson, Lars Rippe, Stefan Kröll, Robert Klieber, and Dieter Suter. Erratum: Hole-burning techniques for isolation and study of individual hyperfine transitions in inhomogeneously broadened solids demonstrated in $\text{pr}^{3+}:\text{Y}_2\text{SiO}_5$ [*phys. rev b* 70, 214116 (2004)]. *Phys. Rev. B*, 71:149902, Apr 2005.
- [186] Thomas Böttger, Y. Sun, C. W. Thiel, and R. L. Cone. Spectroscopy and dynamics of $\text{Er}^{3+}:\text{Y}_2\text{SiO}_5$ at $1.5\ \mu\text{m}$. *Phys. Rev. B*, 74(7):75107, 2006.
- [187] Hayato Goto, Satoshi Nakamura, and Kouichi Ichimura. Experimental determination of intracavity losses of monolithic Fabry-Perot cavities made of $\text{Pr}^{3+}:\text{Y}_2\text{SiO}_5$. *Optics Express*, 18(23):23763, 2010.
- [188] D. L. McAuslan, D. Korystov, and J. J. Longdell. Coherent spectroscopy of rare-earth-metal-ion-doped whispering-gallery-mode resonators. *Phys. Rev. A*, 83:063847, Jun 2011.

- [189] Ivan S Grudinin, Andrey B Matsko, and Lute Maleki. On the fundamental limits of Q factor of crystalline dielectric resonators. *Optics Express*, 15(6):3390–3395, 2007.
- [190] Tian Zhong, Jonathan M. Kindem, Evan Miyazono, and Andrei Faraon. Nanophotonic coherent light–matter interfaces based on rare-earth-doped crystals. *Nature Communications*, 6(1):8206, Sep 2015.
- [191] C. W. Thiel, Thomas Böttger, and R. L. Cone. Rare-earth-doped materials for applications in quantum information storage and signal processing. *J. Lumin.*, 131(3):353–361, Mar 2011.
- [192] Yong Yu, Fei Ma, Xi-Yu Luo, Bo Jing, Peng-Fei Sun, Ren-Zhou Fang, Chao-Wei Yang, Hui Liu, Ming-Yang Zheng, Xiu-Ping Xie, Wei-Jun Zhang, Li-Xing You, Zhen Wang, Teng-Yun Chen, Qiang Zhang, Xiao-Hui Bao, and Jian-Wei Pan. Entanglement of two quantum memories via fibres over dozens of kilometres. *Nature*, 578(7794):240–245, Feb 2020.
- [193] Björn Lauritzen, Ji ří Minář, Hugues de Riedmatten, Mikael Afzelius, Nicolas Sangouard, Christoph Simon, and Nicolas Gisin. Telecommunication-wavelength solid-state memory at the single photon level. *Phys. Rev. Lett.*, 104:080502, Feb 2010.
- [194] Andreas Wallucks, Igor Marinković, Bas Hensen, Robert Stockill, and Simon Gröblacher. A quantum memory at telecom wavelengths. *arXiv preprint arXiv:1910.07409*, 2019.
- [195] Ioana Craiciu, Mi Lei, Jake Rochman, Jonathan M. Kindem, John G. Bartholomew, Evan Miyazono, Tian Zhong, Neil Sinclair, and Andrei Faraon. Nanophotonic quantum storage at telecommunication wavelength. *Phys. Rev. Applied*, 12:024062, Aug 2019.
- [196] Nathaniel B. Phillips, Alexey V. Gorshkov, and Irina Novikova. Light storage in an optically thick atomic ensemble under conditions of electromagnetically induced transparency and four-wave mixing. *Phys. Rev. A*, 83:063823, Jun 2011.

- [197] M Hosseini, B M Sparkes, G T Campbell, P K Lam, and B C Buchler. Storage and manipulation of light using a raman gradient-echo process. *Journal of Physics B: Atomic, Molecular and Optical Physics*, 45(12):124004, jun 2012.
- [198] Connor Michael Kupchak. *Complete Characterization of Quantum Optical Processes with a Focus on Quantum Memory*. PhD thesis, University of Calgary, 2013.
- [199] Mahdi Hosseini, Geoff Campbell, Ben M Sparkes, Ping K Lam, and Ben C Buchler. Unconditional room-temperature quantum memory. *Nature Physics*, 7(10):794, 2011.
- [200] Mahdi Hosseini, Ben M Sparkes, Geoff Campbell, Ping K Lam, and Ben C Buchler. High efficiency coherent optical memory with warm rubidium vapour. *Nature communications*, 2:174, 2011.
- [201] E. S. Moiseev and S. A. Moiseev. Scalable time reversal of raman echo quantum memory and quantum waveform conversion of light pulse. *New J. Phys.*, 15(10):105005, 2013.
- [202] M. T. Turnbull, P. G. Petrov, C. S. Embrey, A. M. Marino, and V. Boyer. Role of the phase-matching condition in nondegenerate four-wave mixing in hot vapors for the generation of squeezed states of light. *Phys. Rev. A*, 88:033845, Sep 2013.
- [203] M. Lobino, C. Kupchak, E. Figueroa, and A. I. Lvovsky. Memory for light as a quantum process. *Phys. Rev. Lett.*, 102:203601, May 2009.
- [204] Vittorio Giovannetti, Seth Lloyd, and Lorenzo Maccone. Quantum private queries. *Phys. Rev. Lett.*, 100:230502, Jun 2008.
- [205] A. Ambainis. Quantum walk algorithm for element distinctness. *SIAM Journal on Computing*, 37(1):210–239, 2007.
- [206] Gilles Brassard, Peter Høyer, and Alain Tapp. Quantum cryptanalysis of hash and claw-free functions. *SIGACT News*, 28(2):14–19, June 1997.

- [207] Vittorio Giovannetti, Seth Lloyd, and Lorenzo Maccone. Quantum random access memory. *Phys. Rev. Lett.*, 100:160501, Apr 2008.
- [208] Vittorio Giovannetti, Seth Lloyd, and Lorenzo Maccone. Architectures for a quantum random access memory. *Phys. Rev. A*, 78:052310, Nov 2008.
- [209] Fang-Yu Hong, Yang Xiang, Zhi-Yan Zhu, Li-zhen Jiang, and Liang-neng Wu. Robust quantum random access memory. *Phys. Rev. A*, 86:010306, Jul 2012.
- [210] Ze-Liang Xiang, Sahel Ashhab, J. Q. You, and Franco Nori. Hybrid quantum circuits: Superconducting circuits interacting with other quantum systems. *Rev. Mod. Phys.*, 85:623–653, Apr 2013.
- [211] H-J Kimble. The quantum internet. *Nature*, 453(7198):1023–1030, 2008.
- [212] J. Nunn, K. Reim, K. C. Lee, V. O. Lorenz, B. J. Sussman, I. A. Walmsley, and D. Jaksch. Multimode memories in atomic ensembles. *Phys. Rev. Lett.*, 101:260502, Dec 2008.
- [213] Daniel Rieländer, Kutlu Kutluer, Patrick M. Ledingham, Mustafa Gündoğan, Julia Fekete, Margherita Mazzera, and Hugues de Riedmatten. Quantum storage of heralded single photons in a praseodymium-doped crystal. *Phys. Rev. Lett.*, 112:040504, Jan 2014.
- [214] Neil Sinclair, Erhan Saglamyurek, Hassan Mallahzadeh, Joshua A. Slater, Mathew George, Raimund Ricken, Morgan P. Hedges, Daniel Oblak, Christoph Simon, Wolfgang Sohler, and Wolfgang Tittel. Spectral multiplexing for scalable quantum photonics using an atomic frequency comb quantum memory and feed-forward control. *Phys. Rev. Lett.*, 113:053603, Jul 2014.
- [215] M Hosseini, Geoff Campbell, Ben M Sparkes, Ping K Lam, and Ben C Buchler. Unconditional room-temperature quantum memory. *Nature Physics*, 7(10):794–798, 2011.

- [216] B M Sparkes, J Bernu, M Hosseini, J Geng, Q Glorieux, PA Altin, P K Lam, N P Robins, and B C Buchler. Gradient echo memory in an ultra-high optical depth cold atomic ensemble. *New Journal of Physics*, 15(8):085027, 2013.
- [217] Mikael Afzelius and Christoph Simon. Impedance-matched cavity quantum memory. *Phys. Rev. A*, 82:022310, Aug 2010.
- [218] Mahmood Sabooni, Qian Li, Stefan Kröll, and Lars Rippe. Efficient quantum memory using a weakly absorbing sample. *Phys. Rev. Lett.*, 110:133604, Mar 2013.
- [219] P Jobez, I Usmani, N Timoney, C Laplane, N Gisin, and M Afzelius. Cavity-enhanced storage in an optical spin-wave memory. *New Journal of Physics*, 16(8):083005, 2014.
- [220] Hua Wu, Richard E. George, Janus H. Wesenberg, Klaus Mølmer, David I. Schuster, Robert J. Schoelkopf, Kohei M. Itoh, Arzhang Ardavan, John J. L. Morton, and G. Andrew D. Briggs. Storage of multiple coherent microwave excitations in an electron spin ensemble. *Phys. Rev. Lett.*, 105:140503, Sep 2010.
- [221] Brian Julsgaard, Cécile Grezes, Patrice Bertet, and Klaus Mølmer. Quantum memory for microwave photons in an inhomogeneously broadened spin ensemble. *Phys. Rev. Lett.*, 110:250503, Jun 2013.
- [222] M Afzelius, N Sangouard, G Johansson, M U Staudt, and C M Wilson. Proposal for a coherent quantum memory for propagating microwave photons. *New Journal of Physics*, 15(6):065008, 2013.
- [223] K. I. Gerasimov, S. A. Moiseev, V. I. Morosov, and R. B. Zaripov. Room-temperature storage of electromagnetic pulses on a high-finesse natural spin-frequency comb. *Phys. Rev. A*, 90:042306, Oct 2014.
- [224] C. Grezes, B. Julsgaard, Y. Kubo, M. Stern, T. Umeda, J. Isoya, H. Sumiya, H. Abe, S. Onoda, T. Ohshima, V. Jacques, J. Esteve, D. Vion, D. Esteve, K. Mølmer, and

- P. Bertet. Multimode storage and retrieval of microwave fields in a spin ensemble. *Phys. Rev. X*, 4:021049, Jun 2014.
- [225] Sergey A Moiseev and Sergey N Andrianov. Photon echo quantum random access memory integration in a quantum computer. *Journal of Physics B: Atomic, Molecular and Optical Physics*, 45(12):124017, 2012.
- [226] S. A. Moiseev and M. I. Noskov. The possibilities of the quantum memory realization for short pulses of light in the photon echo technique. *Laser Physics Letters*, 1(6):303, 2004.
- [227] Thierry Chanelière. Strong excitation of emitters in an impedance matched cavity: the area theorem, π -pulse and self-induced transparency. *Opt. Express*, 22(4):4423–4436, Feb 2014.
- [228] S. A. Moiseev. Off-resonant raman-echo quantum memory for inhomogeneously broadened atoms in a cavity. *Phys. Rev. A*, 88:012304, Jul 2013.
- [229] J. Raftery, D. Sadri, S. Schmidt, H. E. Türeci, and A. A. Houck. Observation of a dissipation-induced classical to quantum transition. *Phys. Rev. X*, 4:031043, Sep 2014.
- [230] BR Johnson, MD Reed, AA Houck, DI Schuster, Lev S Bishop, E Ginossar, JM Gambetta, L DiCarlo, L Frunzio, SM Girvin, et al. Quantum non-demolition detection of single microwave photons in a circuit. *Nature Physics*, 6(9):663–667, 2010.
- [231] A. A. Abdumalikov, O. Astafiev, A. M. Zagoskin, Yu. A. Pashkin, Y. Nakamura, and J. S. Tsai. Electromagnetically induced transparency on a single artificial atom. *Phys. Rev. Lett.*, 104:193601, May 2010.
- [232] Mika A. Sillanpää, Jian Li, Katarina Cicak, Fabio Altomare, Jae I. Park, Raymond W. Simmonds, G. S. Paraoanu, and Pertti J. Hakonen. Autler-townes effect in a superconducting three-level system. *Phys. Rev. Lett.*, 103:193601, Nov 2009.

- [233] Peter B R Nisbet-Jones, Jerome Dilley, Annemarie Holleczek, Oliver Barter, and Axel Kuhn. Photonic qubits, qutrits and ququads accurately prepared and delivered on demand. *New Journal of Physics*, 15(5):053007, 2013.
- [234] M. Pechal, L. Huthmacher, C. Eichler, S. Zeytinoglu, A. A. Abdumalikov, S. Berger, A. Wallraff, and S. Filipp. Microwave-controlled generation of shaped single photons in circuit quantum electrodynamics. *Phys. Rev. X*, 4:041010, Oct 2014.
- [235] S. Hughes. Coupled-cavity qed using planar photonic crystals. *Phys. Rev. Lett.*, 98:083603, Feb 2007.
- [236] Ramachandrarao Yalla, Mark Sadgrove, Kali P. Nayak, and Kohzo Hakuta. Cavity quantum electrodynamics on a nanofiber using a composite photonic crystal cavity. *Phys. Rev. Lett.*, 113:143601, Sep 2014.
- [237] J. D. Thompson, T. G. Tiecke, N. P. de Leon, J. Feist, A. V. Akimov, M. Gullans, A. S. Zibrov, V. Vuletić, and M. D. Lukin. Coupling a single trapped atom to a nanoscale optical cavity. *Science*, 340(6137):1202–1205, 2013.
- [238] Itay Shomroni, Serge Rosenblum, Yulia Lovsky, Orel Bechler, Gabriel Guendelman, and Barak Dayan. All-optical routing of single photons by a one-atom switch controlled by a single photon. *Science*, 345(6199):903–906, 2014.
- [239] S. A. Moiseev and B. S. Ham. Photon-echo quantum memory with efficient multipulse readings. *Phys. Rev. A*, 70:063809, Dec 2004.
- [240] K. F. Reim, J. Nunn, X.-M. Jin, P. S. Michelberger, T. F. M. Champion, D. G. England, K. C. Lee, W. S. Kolthammer, N. K. Langford, and I. A. Walmsley. Multipulse addressing of a raman quantum memory: Configurable beam splitting and efficient readout. *Phys. Rev. Lett.*, 108:263602, Jun 2012.

- [241] Serge Rosenblum, Scott Parkins, and Barak Dayan. Photon routing in cavity qed: Beyond the fundamental limit of photon blockade. *Phys. Rev. A*, 84:033854, Sep 2011.
- [242] Kazuki Koshino, Satoshi Ishizaka, and Yasunobu Nakamura. Deterministic photon-photon $\sqrt{\text{SWAP}}$ gate using a λ system. *Phys. Rev. A*, 82:010301, Jul 2010.
- [243] Julio Gea-Banacloche and Leno M. Pedrotti. Single-photon, cavity-mediated gates: Detuning, losses, and nonadiabatic effects. *Phys. Rev. A*, 86:052311, Nov 2012.
- [244] Daniel A Steck. Rubidium 87 D line data, 2001.
- [245] Marcis Auzinsh, Dmitry Budker, and Simon Rochester. *Optically Polarized Atoms: Understanding Light-Atom Interactions*. Oxford University Press, 2010.

Appendix A

Raman noises

A.1 Spontaneous Emission

Let us consider spontaneous emission rate into the particular Zeeman sublevel $|F, m\rangle$ from the whole hyperfine manifold $|F'\rangle$, and spontaneous emission could happen with any polarization q . The Weisskopf-Wigner approach gives the emission rate as follows [15]:

$$r_{F',Fm} = \frac{\omega_0^3}{3\pi\epsilon_0\hbar c^3} \sum_{m',q} \left| \langle F', m' | \hat{d} \vec{e}_q | F, m \rangle \right|^2, \quad (\text{A.1})$$

where \hat{d} is a dipole moment operator, \vec{e}_q is a normalized polarization vector, and ω_0 the central frequency of the transition. By applying the Wigner-Eckart theorem A.1.1, we arrive at

$$r_{F',Fm} = \frac{\omega_0^3}{3\pi\epsilon_0\hbar c^3} \left| \langle F | \hat{d} | F' \rangle \right|^2 \sum_{m',q} \left(\begin{matrix} F' & 1 & F \\ -m' & q & m \end{matrix} \right)^2, \quad (\text{A.2})$$

where under the sum is squared 3-j symbol. Applying the theorem for the second time we decompose the reduced dipole matrix element of total atomic angular momentum into a

reduced dipole matrix element of total electron angular momentum:

$$r_{F',Fm} = \frac{\omega_0^3}{3\pi\epsilon_0\hbar c^3} \left| \langle \xi J' | \hat{d} | \xi J \rangle \right|^2 (2F+1)(2F'+1) \left\{ \begin{matrix} J' & F' & I \\ F & J & 1 \end{matrix} \right\}^2 \sum_{m',q} \left(\begin{matrix} F' & 1 & F \\ -m' & q & m \end{matrix} \right)^2, \quad (\text{A.3})$$

where ξ stands for other atomic numbers besides J and m . 6-j symbol is represented by the following matrix:

$$\left\{ \begin{matrix} J' & F' & I \\ F & J & 1 \end{matrix} \right\}. \quad (\text{A.4})$$

The reduced dipole moment element is related to the lifetime by [244]:

$$\frac{\omega_0^3}{3\pi\epsilon_0\hbar c^3} \left| \langle \xi J | \hat{d} | \xi J' \rangle \right|^2 \frac{1}{2J'+1} = 1/\tau. \quad (\text{A.5})$$

Thus

$$r_{F',Fm} = \frac{2J'+1}{\tau} (2F+1)(2F'+1) \left\{ \begin{matrix} J' & F' & I \\ F & J & 1 \end{matrix} \right\}^2 \sum_{m',q} \left(\begin{matrix} F' & 1 & F \\ -m' & q & m \end{matrix} \right)^2. \quad (\text{A.6})$$

Lifetimes for Rubidium 87 atoms are $\tau_{D_2} = 26.24(4)\text{ns}$ and $\tau_{D_1} = 27.70(4)\text{ns}$ with nuclear spin $I = 3/2$ [244]. The experiment was conducted on D_1 line with level $|2\rangle$ corresponding to the level with total atomic angular momentum $F = 2$ which 6-j symbol being equal to $-\frac{1}{2\sqrt{5}}$, while $|1\rangle$ level corresponds to level having $F = 1$ and $-\frac{1}{2\sqrt{3}}$, respectively. The decay

constants in this case can be expressed as

$$r_{13}(F = 1 \rightarrow F' = 2) = \frac{(2 + 1)}{27.7 \text{ ns}} \left(\frac{1}{2\sqrt{3}} \right)^2 = 2\pi \cdot 1.43 \text{ MHz}, \quad (\text{A.7})$$

$$r_{23}(F = 2 \rightarrow F' = 2) = \frac{(2 \cdot 2 + 1)}{27.7 \text{ ns}} \left(\frac{1}{2\sqrt{5}} \right)^2 = 2\pi \cdot 1.43 \text{ MHz}, \quad (\text{A.8})$$

$$r_{13}(F = 1 \rightarrow F' = 1) = \frac{3}{27.7 \text{ ns}} \left(\frac{1}{6} \right)^2 = 2\pi \cdot 0.48 \text{ MHz}, \quad (\text{A.9})$$

$$r_{23}(F = 2 \rightarrow F' = 1) = \frac{5}{27.7 \text{ ns}} \left(\frac{1}{2\sqrt{3}} \right)^2 = 2\pi \cdot 2.39 \text{ MHz}. \quad (\text{A.10})$$

Sum of all decays is $r_{\text{sum}} = 2\pi \cdot 5.73 \text{ MHz}$.

Let us consider D_1 line, for which the total electron angular momentum is $J = 1/2$. The atomic levels with total atomic angular momentum correspond to the memory levels: $|1\rangle \rightarrow |F = 1\rangle$, $|2\rangle \rightarrow |F = 2\rangle$, and $|3\rangle \rightarrow |F' = 2\rangle$, as shown in Figure 5.7. For calculating the coupling constant we assume the signal mode has polarization \vec{e}_q (in spherical basis) and the the atomic level $|1\rangle$ corresponds to sublevel of $F = 1$ manifold:

$$|g_s|^2 = \frac{\omega}{2\epsilon_0 \hbar S c} \left| \langle 1 | \vec{d} \vec{e}_q | 3 \rangle \right|^2 = \frac{\omega}{2\epsilon_0 \hbar S c} \sum_{m'} \left| \langle F = 1, m | \vec{d} \vec{e}_q | F' = 2, m' \rangle \right|^2 = \quad (\text{A.11})$$

$$= \frac{\omega}{2\epsilon_0 \hbar S c} \sum_{m'} \left(\begin{matrix} F & 1 & F' \\ m & q & m' \end{matrix} \right)^2 \left| \langle n' J' I F' | d | n J I F \rangle \right|^2 \quad (\text{A.12})$$

$$= \frac{\omega}{2\epsilon_0 \hbar S c} \sum_{m'} \left(\begin{matrix} F & 1 & F' \\ m & q & m' \end{matrix} \right)^2 (2F + 1)(2F' + 1) \left\{ \begin{matrix} J' & F' & I \\ F & J & 1 \end{matrix} \right\}^2 \left| \langle \xi' J' | d | \xi J \rangle \right|^2 \quad (\text{A.13})$$

Assuming circular polarization σ_{\pm} ($q = \pm 1$) and $|1\rangle = |F = 1, m = \pm 1\rangle$, upper level $|3\rangle =$

$|F' = 2\rangle$ we get:

$$\sum_{m'} \begin{pmatrix} F & 1 & F' \\ m & q & m' \end{pmatrix}^2 = 1/5, \quad \left\{ \begin{matrix} J' & F' & I \\ F & J & 1 \end{matrix} \right\}^2 = 1/12, \quad (\text{A.14})$$

$$\sum_{m'} \begin{pmatrix} F & 1 & F' \\ m & q & m' \end{pmatrix}^2 (2F+1)(2F'+1) \left\{ \begin{matrix} J' & F' & I \\ F & J & 1 \end{matrix} \right\}^2 = \frac{1}{4}. \quad (\text{A.15})$$

As another example, let's consider circular polarization σ_{\pm} ($q = \pm 1$) and $|2\rangle = |F = 2, m = \pm 1\rangle$, upper level $|3\rangle = |F' = 2\rangle$ we get:

$$\sum_{m'} \begin{pmatrix} F & 1 & F' \\ m & q & m' \end{pmatrix}^2 = 1/15, \quad \left\{ \begin{matrix} J' & F' & I \\ F & J & 1 \end{matrix} \right\}^2 = 1/20, \quad (\text{A.16})$$

$$\sum_{m'} \begin{pmatrix} F & 1 & F' \\ m & q & m' \end{pmatrix}^2 (2F+1)(2F'+1) \left\{ \begin{matrix} J' & F' & I \\ F & J & 1 \end{matrix} \right\}^2 = \frac{1}{12}. \quad (\text{A.17})$$

The coupling constant for the continuous field is calculated similarly as for a cavity with effective volume to be a product of area and speed of light ($V \rightarrow S_c c$):

$$|g_s|^2 = \frac{\omega}{2\epsilon_0 \hbar S_c} \frac{|\langle \xi' J' | d | \xi J \rangle|^2}{4} = \frac{1}{\tau} \frac{3}{2} \frac{\pi c^2}{4 S_s \omega^2}, \quad (\text{A.18})$$

Analogously we find Rabi frequency of control field with amplitude $|E_c|$ on the same $|1\rangle \rightarrow |3\rangle$ transition:

$$\begin{aligned} \Omega_I^2 &= \frac{E_c^2}{\hbar^2} \sum_{m'} \begin{pmatrix} F & 1 & F' \\ m & q & m' \end{pmatrix}^2 (2F+1)(2F'+1) \left\{ \begin{matrix} J' & F' & I \\ F & J & 1 \end{matrix} \right\}^2 |\langle \xi' J' | d | \xi J \rangle|^2 \\ &= \frac{E_c^2}{\hbar^2} \frac{|\langle \xi' J' | d | \xi J \rangle|^2}{4}. \end{aligned} \quad (\text{A.19})$$

While for circularly polarized control field on $|2\rangle \rightarrow |3\rangle$ is:

$$\Omega_s^2 = \frac{E_c^2}{\hbar^2} \frac{|\langle \xi' J' | d | \xi J \rangle|^2}{12}. \quad (\text{A.20})$$

As the result the ratio between to Rabi frequencies is $\Omega_I/\Omega_s = \sqrt{3}$.

A.1.1 The Wigner-Eckart theorem

If the T_q^k is irreducible tensor component of rank k , then the Wigner-Eckart theorem states [245]:

$$\langle \xi J' m' | T_q^k | \xi J m \rangle = \langle \xi' J' | T^k | \xi J \rangle (-1)^{J'-m'} \begin{pmatrix} J' & k & J \\ -m' & q & m \end{pmatrix}. \quad (\text{A.21})$$

For the state composed of the two angular momentum the Wigner-Eckart theorem states [245]:

$$\langle \xi J' I F' | T^k | \xi J I F \rangle = (-1)^{J+I+F+1} \sqrt{(2F+1)(2F'+1)} \begin{Bmatrix} J' & F' & I \\ F & J & 1 \end{Bmatrix} \langle \xi J' | T^k | \xi J \rangle. \quad (\text{A.22})$$

A.2 Effect of spatial modulation

Adiabatic elimination of the upper level $|3\rangle$ gives the following Heisenberg-Langevin equations [201]:

$$(\tilde{\gamma}_{12}(z) + i(\beta z + i\Delta_{AC} - \omega)) \hat{R}_{12}(t, z) = -i \frac{g_s \Omega_c^*(z)}{(\Delta_s + i\gamma_{13})} \hat{\mathcal{E}}_s(t, z), \quad (\text{A.23})$$

$$\frac{\partial}{\partial z} \hat{\mathcal{E}}_s(t, z) = -i \frac{ng_s}{(\Delta_s + i\gamma_{13})} \Omega_c(z) \hat{R}_{12}(t, z). \quad (\text{A.24})$$

If we assume the phase matching holds $e^{-i\delta kL} \approx 1$, the full solution for the field is

$$\begin{aligned} \hat{\mathcal{E}}_s(\omega, z) = & \hat{\mathcal{E}}_s(\omega, -L/2) \exp \left(- \int_{-L/2}^z dz' \frac{ng_s^2 \Omega^2(z')}{(\Delta_s + i\gamma_{13})^2 (\tilde{\gamma}_{12}(z') + i(\beta z' + i\Delta_{AC}(z') - \omega))} \right) + \\ & - \int_{-L/2}^z dz' \hat{F}_s(\omega, z') \exp \left(- \int_{z'}^z dz'' \frac{ng_s^2 \Omega^2(z'')}{(\Delta_s + i\gamma_{13})^2 (\tilde{\gamma}_{12}(z'') + i(\beta z'' + \Delta_{AC}(z'') - \omega))} \right). \end{aligned} \quad (\text{A.25})$$

The spatial modulation of the pump we assume to be in the following form [198]:

$$\Omega(z) = \Omega_c(1 + \epsilon \cos(k_m z)). \quad (\text{A.26})$$

The modulation modifies the noise contribution to

$$\begin{aligned} \langle n(\omega) \rangle \sim & \iint_{-L/2}^z dz' dz'' \langle \hat{F}_s^\dagger(\omega, z'') \hat{F}_s(\omega, z') \rangle \\ & \cdot \exp \left\{ - \int_{z'}^z dx' \frac{ng_s^2 \Omega^2(x')}{(\Delta_s + i\gamma_{13})^2 (\tilde{\gamma}_{12}(x') - i(\beta x' + \Delta_{AC}(x') - \omega))} \right\} \\ & \cdot \exp \left\{ - \int_{z''}^z dx'' \frac{ng_s^2 \Omega^2(x'')}{(\Delta_s - i\gamma_{13})^2 (\tilde{\gamma}_{12}(x'') + i(\beta x'' + \Delta_{AC}(x'') - \omega))} \right\}. \end{aligned} \quad (\text{A.27})$$

A.3 Simulation parameters

symbol	Value	Units	Formula Reference	Parameter
T	74	C		temperature
Sc	$28 \cdot 10^{-6}$	$1/\text{m}^2$		Control field cross section
Ss	$3 \cdot 10^{-6}$	$1/\text{m}^2$		Signal field cross section
σ_D	0.5	GHz	$\sqrt{\frac{kT}{m}} \cdot 10^{-6}/\lambda$	width of the Doppler broadening
ω_{12}	$2\pi \cdot 6834$	MHz		hyperfine splitting
r_{32}	$2\pi \cdot 1.43$	MHz		decay rate of population
r_{31}	$2\pi \cdot 1.43$	MHz		decay rate of population
γ_{13}	$2\pi \cdot 1.43$	MHz	$(r_{32} + r_{31})/2$	coherence decay
γ_{23}	$2\pi \cdot 1.43$	MHz	$(r_{32} + r_{31})/2$	coherence decay
γ_{12}	$2\pi \cdot 40$	kHz		
Δ_s	$2\pi \cdot 1330$	MHz		
Δ_I	$2\pi \cdot 5504$	MHz	$\omega_{21} - \Delta_s$	
n	$4.5 \cdot 10^{14}$	$1/\text{m}^3$		atomic density
β	$2\pi \cdot 3.2$	MHz/m		magnetic gradient linear density
P	0.34	W		power of control field
L	0.2	m		length of sample
Δ_{in}	$2\pi \cdot 0.68$	MHz	βL	inhomogeneous broadening
ν_0	0.055			spatial modulation frequency
Ω_c	$2\pi \cdot 16.6$	MHz	$\sqrt{\frac{P}{\epsilon_0 S c \cdot c}} \frac{d_{23}}{2\hbar} \cdot 10^{-6}$	Rabi frequency of the control field for P=0.34
Ω_I	$2\pi \cdot 28.78$	MHz	$\epsilon \Omega_c$	Rabi frequency of the control field for P=0.34
ϵ	$\sqrt{3}$			Ratio between coupling constants

Table (A.1) Parameters used to fit an experimental data

Appendix B

Time-bin quantum random access memory

B.1 Hamiltonian and equations of motions

Here we present the effective Hamiltonian of the analyzed system 6.3 under dipole and rotating-wave approximations [15]. It consist from two parts $\hat{H} = \hat{H}_0 + \hat{H}_1$, where

$$\hat{H}_0 = \hbar\omega_0 \left(\sum_{j=1}^N S_z^j + S_z^c + a_1^\dagger a_1 + a_2^\dagger a_2 + \int d\omega \left(\sum_m \hat{c}_m^\dagger(\omega) \hat{c}_m(\omega) + b^\dagger(\omega) b(\omega) \right) \right), \quad (\text{B.1})$$

is the unperturbed Hamiltonian. The perturbation part is

$$\begin{aligned}
\hat{H}_1 = & \hbar \sum_j^N \Delta_j \hat{S}_z^j + \hbar \delta S_z^c + \hbar \int d\nu \nu \hat{b}^\dagger(\omega_0 + \nu) \hat{b}(\omega_0 + \nu) \\
& + \hbar \sum_m \int d\nu \nu \hat{c}_m^\dagger(\omega_0 + \nu) \hat{c}_m(\omega_0 + \nu) + \\
& + \hbar \sqrt{\frac{\kappa}{2\pi}} \int d\nu (\hat{a}_1^\dagger \hat{b}(\omega_0 + \nu) + H.C.) \\
& + \hbar \left(g_1 \hat{a}_1^\dagger \hat{S}_-^c + f_2 \hat{a}_1^\dagger \hat{a}_2 + g_2 \sum_{j=1}^N \hat{a}_2^\dagger \hat{S}_-^j + H.C. \right) \\
& + \hbar \sqrt{\frac{\gamma}{2\pi}} \sum_m \int d\nu \left(\hat{c}_m(\omega_0 + \nu) \hat{S}_+^c + H.C. \right), \tag{B.2}
\end{aligned}$$

where the first three terms are determined by the frequency detunings of the j -th atom Δ_j in QM, δ - of the control atom and the detuning ν of the free field modes. Four further terms are the interactions between free field modes and the first cavity mode with the coupling constant $\sqrt{\kappa/2\pi}$.

The interaction between the cavity mode and the control atom with the coupling constant is g_1 . The interaction between the coupled cavity modes with the coupling constant is f_2 . The interaction between the second cavity mode and the atoms with the coupling constant g_2 . The operators \hat{S}_z^0 and \hat{S}_z^j are the z projection of the spin 1/2 operators, \hat{S}_+^j , \hat{S}_-^j and \hat{S}_+^0 , \hat{S}_-^0 are the transition spin operators of j -th and control atoms. The operators $\hat{a}_{1,2}^\dagger$ and $\hat{a}_{1,2}$ are creation and annihilation operators of the 1-st and 2-nd cavity field modes. The operators $b^\dagger(\omega)$, $b(\omega)$ are the bosonic operators of free propagating modes ($[b(\omega), b^\dagger(\omega')] = \delta(\omega - \omega')$).

By assuming that the cavity modes, all the atoms and bath modes $c_m(\omega)$ are in the ground state, the initial wave function of the input single photon field is given by Eq. 6.1, the total wavefunction is given by Eq. 6.3. After using the well-known input-output formalism we

obtain the following system of equations [33]:

$$\frac{d\alpha_1}{dt} = -ig_1\beta_c - if_2\alpha_2 - \frac{\kappa}{2}\alpha_1 + \sqrt{\kappa}\alpha_{in}(t), \quad (\text{B.3})$$

$$\frac{d\beta_c}{dt} = -i(\delta - i\gamma/2)\beta_c - ig_1\alpha_1, \quad (\text{B.4})$$

$$\frac{d\alpha_2}{dt} = -ig_2 \sum_{j=1}^N \beta_j - if_2\alpha_1, \quad (\text{B.5})$$

$$\frac{d\beta_j}{dt} = -i(\Delta_j - i/T_2)\beta_j - ig_2\alpha_2, \quad (\text{B.6})$$

where we have added the weak phenomenological decay constant $1/T_2$ for the QM atomic coherence which is caused by the interaction with the local fluctuating fields

$$\alpha_{in}(t) = -\frac{i}{\sqrt{2\pi}} \int d\nu \alpha_\nu^o e^{-i\nu t}. \quad (\text{B.7})$$

By integrating Eq. B.6 we find

$$\begin{aligned} \beta_j(\tau) &= -ig_2 \int_{-\infty}^{\tau} dt' \alpha_2(t') e^{-i(\Delta_j - i/T_2)(\tau - t')} \Big|_{\lim_{\tau} \gg \delta t} \\ &\cong -i2\pi g_2 \tilde{\alpha}_2(\Delta_j) e^{-i(\Delta_j - i/T_2)\tau}, \end{aligned} \quad (\text{B.8})$$

where pulse duration of the light field δt is assumed to be short enough in comparison with the atomic decoherence time of the atomic QM $\delta t \ll T_2$. Inserting it into Eq. B.5 and using the Fourier transform $\alpha_{1,2,in}(t) = \int d\nu \tilde{\alpha}_{1,2,in}(\nu) \exp\{-i\nu t\}$, and $\beta_c(t) = \int d\nu \tilde{\beta}_c(\nu) \exp\{-i\nu t\}$, we obtain the following solution for the amplitudes of the control atom and two cavity modes:

$$\tilde{\beta}_c = g_1 \frac{\tilde{\alpha}_1}{(\nu - \delta + i\gamma/2)}, \quad (\text{B.9})$$

$$\tilde{\alpha}_2(\nu) = A_{2,1}(\nu) \tilde{\alpha}_1(\nu), \quad (\text{B.10})$$

$$\tilde{\alpha}_1(\nu) = A_{1,in}(\nu) \tilde{\alpha}_{in}(\nu), \quad (\text{B.11})$$

where

$$A_{1,\text{in}}(\nu) = \frac{i\sqrt{\kappa}}{\nu + i\kappa/2 - \frac{g_1^2}{(\nu - \delta + i\gamma/2)} - \frac{f_2^2}{\nu + iNg_2^2\tilde{G}(\nu)}}, \quad (\text{B.12})$$

$$A_{2,1}(\nu) = \frac{f_2}{\nu + iNg_2^2\tilde{G}(\nu)}. \quad (\text{B.13})$$

B.2 Readout stage

The system of light-atom dynamical equations during the readout stage is almost the same as Eqs. B.3–B.6, except for the absence of the driving laser field and the inverted inhomogeneous broadening at the time $t = \tau$:

$$\frac{d\alpha_1}{dt} = -ig_1\beta_1 - if_2\alpha_2 - \frac{\kappa}{2}\alpha_1, \quad (\text{B.14})$$

$$\frac{d\beta_c}{dt} = -i(\delta - i\gamma/2)\beta_c - ig_1\alpha_1, \quad (\text{B.15})$$

$$\frac{d\alpha_2}{dt} = -ig_2 \sum_{j=1}^N \beta_j - if_2\alpha_1, \quad (\text{B.16})$$

$$\frac{d\beta_j}{dt} = i(\Delta_j + i/T_2)\beta_j - ig_2\alpha_2. \quad (\text{B.17})$$

By taking into account the initial condition at $t = \tau$ in accordance with Eq. 6.5 and $\alpha_1 = \alpha_2 = \beta_c = 0$ we have

$$\beta_j(-\Delta_j, \tau) = i\sqrt{2\pi\kappa}\frac{g_2}{f_2}F_S(\Delta_j)\alpha_{\Delta_j}^0 e^{-i(\Delta_j - i/T_2)\tau}, \quad (\text{B.18})$$

before the rephasing of the atomic coherence. After solving the linear system of equations B.14–B.17, we find the following spectral component of the irradiated single photon field

$$\alpha_\nu(t) = i\sqrt{2\pi\kappa}\frac{g_2}{f_2}F_R(\nu)\beta(\nu, \tau) \cdot G_L(\nu) \exp\{-i\nu(t - \tau) - \tau/T_2\}, \quad (\text{B.19})$$

where $F_R(\nu)$ indicates the spectral transfer function for the readout stage.

B.3 Blockade and wave function of the QM atomic system

For the blockade regime during the retrieval, we find the following Fourier image for the amplitude of the QM atomic excitation from the Eqs. B.14-B.17:

$$\beta_B(\Delta, \nu) = \frac{1}{1/T_2 - i\nu - i\Delta} \cdot \left(\beta(\Delta, 0) + \Delta_{\text{in}} J(\nu) (F_B(\nu) - 1) \int d\Delta' \frac{G(\Delta') \beta(\Delta', 0)}{-i\nu + i\Delta'} \right), \quad (\text{B.20})$$

where the index “B” means the blockade regime and

$$J(\nu) = \frac{\kappa(\kappa - 2i\nu)}{\kappa^2 - 4i\kappa\nu - 8\nu^2}. \quad (\text{B.21})$$

In the case of the strong atomic blockade $2 + 4C \gg 1$:

$$\beta_B(\Delta, \nu) \cong \frac{1}{1/T_2 - i\nu - i\Delta} \cdot \left(\beta_0(\Delta, 0) e^{-i\Delta\tau} - \frac{2\Delta_{\text{in}}^2 J(\nu)}{(\nu^2 + \Delta_{\text{in}}^2)} \beta_0(-\nu, 0) e^{i\nu\tau - \tau/T_2} \right), \quad (\text{B.22})$$

where $\beta_0(-\nu, 0) = i\sqrt{2\pi\kappa} \frac{g_2}{f_2} F(-\nu) \alpha_{-\nu}^0 e^{-\tau/T_2}$. Since $J(\nu \approx 0) \approx 1$ and $\tau \ll T_2$, we obtain good recovery of the atomic amplitude for $|\nu| < \kappa$:

$$\beta_B(\Delta, |\nu| < \kappa) |_{\tau \ll T_2} = -\frac{\beta(\Delta, 0)}{1/T_2 - i\nu - i\Delta}. \quad (\text{B.23})$$

As it is seen in Eq. B.23, the atomic dynamics during the irradiation and subsequent reabsorption of the echo pulse leads to the additional π -phase shift of the atomic coherence for $t \gg t_{\text{echo}} = 2\tau$.